Experimental and numerical investigations of compressible, transient, and subcritical vessel outflows

Zur Erlangung des akademischen Grades eines

Dr.-Ing.

von der Fakultät Bio- und Chemieingenieurwesen
der Technischen Universität Dortmund
genehmigte Dissertation

vorgelegt von

M.Sc. Michael-David Fischer

aus

Wesel

Tag der mündlichen Prüfung: 24.04.2024

1. Gutachter: Prof. Dr.-Ing. Peter Ehrhard

2. Gutachter: Prof. Dr.-Ing. Uwe Janoske

Dortmund 2024

sapere aude

- Horaz -

Danksagung

Diese Dissertation wurde im Rahmen meiner intensiven Tätigkeit als wissenschaftlicher Mitarbeiter in der Arbeitsgruppe Strömungsmechanik an der Technischen Universität Dortmund angefertigt. An dieser Stelle möchte ich mich herzlichst bei allen Menschen bedanken, die mich während dieser Zeit begleitet und unterstützt haben. Mein besonderer Dank gilt meinem Doktorvater Prof. Dr.-Ing. Peter Ehrhard, der mir die Möglichkeit gegeben hat an dieser Promotion zu arbeiten und mich auch in seinem Ruhestand betreut hat. Prof. Dr.-Ing. Uwe Janoske danke ich vielmals für die Übernahme des Zweitgutachtens. Des Weiteren spreche ich Prof. Dr. rer. nat. Markus Thommes und Prof. Dr.-Ing. Norbert Kockmann, als Teil der Prüfungskommission, meinen Dank aus.

Großer Dank gilt meinen aktuellen und auch ehemaligen Kollegen der Professuren Strömungsmechanik, Apparatedesign und Transport Processes: Prof. Dr.-Ing. Alba Diéguez-Alonso, Simon Baier, Friedrich Barth, Alexander Behr, Dr.-Ing. Konrad Boettcher, Inga Burke, Dr.-Ing. Jayotpaul Chaudhuri, Andrea Dernbecher, Robin Dinter, Dr.-Ing. Juan Jesús Rico Fuentes, Dr.-Ing. Lutz Gödecke, Dr.-Ing. Sabrina Grünendahl, Ingo Hanning, Dr.-Ing. Christian Heckmann, Dr.-Ing. Ann Kathrin Höffmann, Stefan Höving, Nils Kaufhold, Tatjana Kornhof, Dr.-Ing. Peter Lakshmanan, Dr.-Ing. Tim Neumann, Dr.-Ing. Jonas Oeing, Bastian Oldach und Fabienne Ryll.

Vielen Dank an die Mitarbeiter der mechanischen Werkstatt der TU Dortmund und insbesondere Gerriet Jäger, die mit viel Engagement und Expertise meine Konstruktionen in die Tat umgewandelt haben. Vielen Dank an Dr. rer. nat. Swetlana Herbrandt und Dr. rer. nat. Uwe Ligges für ihre Unterstützung bei der statistischen Auswertung meiner experimentellen Daten. Vielen Dank an Kenan Golgiyaz, der mir eine große Hilfe war, das optimale PDA-Setup zu finden. Vielen Dank an die Firma Walter Ludwig, Behälter- und Anlagenbau e.K., ohne deren speziell für meine Anforderungen gefertigten Behälter diese Forschung nicht möglich gewesen wäre.

Abschließend gilt ein ganz besonderer Dank meinen Eltern, Christel und Rolf, meiner Familie und meinen Freunden, die mir immer ein Rückhalt sind und den Rücken freihalten. Ohne Euch wäre ich mit Sicherheit nicht da, wo ich jetzt stehe. Danke!

Im Licht der jüngsten Ereignisse sind die Bande der Freundschaft, die wir hier geknüpft haben, wichtiger denn je. Beherzigt das!

- Albus Dumbledore -

Zusammenfassung

Das Ausströmen eines Gases aus einem unter Druck stehenden Behälter gehört zu den klassischen strömungsmechanischen Grundlagenproblemen. Gerade der kompressible und unterkritische Fall ist hierbei komplexer als sich zunächst vermuten lässt und es gibt keine allgemeine analytische Lösung. Dieser Fall soll hier näher untersucht werden. So wird zunächst eine allgemeine selbstähnliche Lösung hergeleitet sowie eine dimensionslose Kennzahl identifiziert, mit der die Ausströmung ohne aufwändige numerische Berechnungen charakterisiert werden kann. Dieses selbstähnliche Modell wird anhand von numerischen Simulationen und experimentellen Untersuchungen validiert.

Weiter bildet sich bei der Ausströmung aus dem Kessel in eine freie Umgebung ohne begrenzende Wände ein Freistrahl aus, welcher ebenfalls näher untersucht wird. Hierzu wird das transiente Geschwindigkeitsfeld von Luft-, Kohlenstoffdioxid- und Helium-Freistrahlen nach der schlagartigen Öffnung eines Kessels experimentell erstmalig mittels Laser Doppler Anemometrie und Phasen Doppler Anemometrie vermessen. Hierbei steht neben der Fragestellung nach der Selbstähnlichkeit des Geschwindigkeitsfeldes der Einfluss der Reynolds-Zahl und der Dichte des ausströmenden Gases im Fokus. Weiterführend werden die experimentellen Ergebnisse der transienten Freistrahlen mit numerischen Simulationen verglichen. Hierzu werden sowohl das etablierte k-ε Turbulenzmodell als auch das relativ neue verallgemeinerte k-ω (GEKO) Turbulenzmodell verwendet. Hierbei sollen potentielle Fehlerquellen wie Auftriebseffekte und schwankende Umgebungsbedingungen, wie sie in den experimentellen Untersuchungen auftauchen können, gezielt ausgeschaltet werden. Weiter wird untersucht, ob das GEKO Modell möglicherweise Vorteile gegenüber dem k-ε Turbulenzmodell bei der Berechnung von Freistrahlen aufweist.

Abstract

The outflow of a gas from a pressurised vessel is one of the classical fundamental problems in fluid mechanics. However, the compressible and subcritical case is more complex than one might think and there is no general analytical solution. This case will be examined in more detail in this dissertation. A general self-similar solution is first derived and a dimensionless number is identified with which the outflow can be characterised without time-consuming numerical simulations. This self-similar model is validated by means of numerical simulations and experimental investigations.

Furthermore, a free jet is formed during the outflow from the vessel into a free environment without bounding walls, which is also investigated in more detail. For this purpose, the transient velocity field of air, carbon dioxide and helium free jets after the sudden opening of a vessel is measured experimentally for the first-time using laser Doppler anemometry and phase Doppler anemometry. In addition to the question of the self-similarity of the velocity field, the influence of the Reynolds number and of the density of the outflowing gas will be examined. The experimental results of the transient free jets are then compared with numerical simulations. For this purpose, both the established k-ε turbulence model and the relatively-new generalised k-ω (GEKO) turbulence model are used. Here, potential sources of error such as buoyancy effects and fluctuating ambient conditions, which can occur in the experimental investigations, are to be specifically eliminated. Finally, the question of whether or not the GEKO model possibly has advantages over the k-ε turbulence model in the simulation of free jets is investigated.

Contents

Nomenclature

Latin symbols

Symbol	Meaning	Unit
a	fitting parameter	-
a_s	speed of sound	m s^{-1}
A	area, cross section	m^2
A^*	constricted cross section	m^2
A_u	spreading constant	-
A_V	vessel surface	m^2
b	fitting parameter	-
c	area averaged velocity	m s^{-1}
c_p	specific heat capacity at constant pressure	m^2 s^{-2} K^{-1}
c_V	specific heat capacity at constant volume	m^2 s^{-2} K^{-1}
$c_{1,a}$	coefficient to model $K_{1,u}(\mathrm{Re})$	-
$c_{1,b}$	coefficient to model $K_{1,u}(\mathrm{Re})$	-
$c_{2,a}$	coefficient to model $K_{2,u}(\mathrm{Re})$	-
$c_{2,b}$	coefficient to model $K_{2,u}(\mathrm{Re})$	-
d	diameter	m
d_e	effective diameter	m
d_p	particle diameter	m
d_{pc}	diameter of particle class centre	m
$d_{p,\max}$	maximum measurable particle diameter	m
d_V	vessel diameter	m
D_S	diffusion coefficient of species S	m^2 s^{-1}
$f_{i\pm}$	auxiliary function for the determination of the phase factor	-
F_1	GEKO model function	-
F_2	GEKO model function	-
F_3	GEKO model function	-
h	specific enthalpy	m^2 s^{-2}
h_{tot}	specific total enthalpy	m^2 s^{-2}
$j_{S,i}$	diffusion flux density of species S in spatial direction i	mol m^{-2} s^{-1}
k	turbulent kinetic energy per unit mass	m^2 s^{-2}
K	absolute roughness of a surface	m
$K_{1,u}$	velocity decay constant	-
$K_{2,u}$	spreading rate	-
L	length	m
L_V	length of the vessel	m
m	gas mass	kg
$\dot{m}_{\mathrm{dis}}$	discharging gas mass flow	kg s^{-1}
M	molar mass	kg mol^{-1}

n	refraction index	-
n_{rel}	relative refraction index	-
N	number of discrete points in time used to determine the discharge average values	-
p	pressure	kg m^{-1} s^{-2}
p-value	significance value	-
p_{mod}	modified pressure	kg m^{-1} s^{-2}
p^*	critical pressure	kg m^{-1} s^{-2}
P_k	turbulent production due to viscous forces	kg m^{-1} s^{-3}
P_{kb}	turbulent production due to buoyancy	kg m^{-1} s^{-3}
$P_{\varepsilon b}$	turbulence dissipation due to buoyancy	kg m^{-1} s^{-3}
q_j	heat flux density in direction j	kg s^{-3}
Q_0	cumulative number distribution	-
r	radius	m
R^2	coefficient of determination	-
s	spatial coordinate along the streamline	m
S	strain	s^{-1}
S_E	energy sources or sinks	kg m^{-1} s^{-3}
$S_{M,i}$	momentum sources or sinks in the direction i	kg m^{-2} s^{-2}
t	time	s
t_{dis}	discharge duration	s
t_{inertia}	discharge duration that is inertia dominated	s
T	absolute temperature	K
u	axial velocity component in x direction	m s^{-1}
$u_{0,p}$	velocity of the tracer particles at the pipe outlet	m s^{-1}
V	vessel volume	m^3
V^*	characteristic volume	m^3
x	spatial coordinate	m
x_0	virtual jet origin	m
$\vec{x}$	spatial vector	m
x_c	core length	m
y	spatial coordinate	m
Y_S	mass fraction of component S	kg kg^{-1}
z	spatial coordinate	m
$z_{0.5u}$	half width	m

Greek symbols

Symbol	Meaning	Unit
α	significance level	-
α_h	heat transfer coefficient	W m^{-2} K^{-1}
β_g	phase factors	-
Γ_t	eddy diffusion	kg m^{-1} s^{-1}

δ_{ij}	Kronecker delta	-
Δf	frequency of the scattered laser light	s^{-1}
$\Delta p_{\mathrm{fritction}}$	frictional pressure losses	Pa
$\Delta p_{\mathrm{inertia}}$	inertial pressure losses	Pa
Δp_{loss}	pressure losses	Pa
Δt	time step size	s
$\Delta \hat{t}$	averaging interval to determine the current mean velocity	s
Δx	mesh spacing	m
Δx_f	fringe spacing	m
$\Delta \phi_{gh}$	phase shift	rad
ε	turbulent dissipation rate	$m^2\ s^{-3}$
ϵ_H	discretisation error	$[\Phi]$
ζ	pressure loss coefficient	-
ϑ	angle of intersection between the two incident laser beams	°
λ	thermal conductivity	$W\ m^{-1}\ K^{-1}$
λ_f	drag coefficient	-
λ_w	wavelength	m
μ	dynamic viscosity	Pa s
μ_{eff}	effective viscosity	Pa s
μ_c	contraction coefficient	-
μ_t	turbulent viscosity	Pa s
ϱ	density	$kg\ m^{-3}$
σ	standard deviation	$[\sigma]$
σ_{rel}	relative standard deviation	-
τ_{ij}	shear stress tensor	$kg\ m^{-1}\ s^{-2}$
φ	angle between transmitting and receiving head	°
ϕ	scalar quantity	$[\phi]$
Φ	exact solution	$[\Phi]$
ψ	angle between transmitting and receiving head	°
ω	turbulent frequency	s^{-1}
Ω	vorticity	s^{-1}

Mathematical symbols

Symbol	Meaning	Unit
$\bar{x}$	time averaged value of x	$[x]$
x'	turbulent fluctuation of x	$[x]$
$\hat{x}$	current mean value of x	$[x]$
$\bar{\hat{x}}$	discharge average current mean value of x	$[x]$

Dimensionless numbers

Symbol	Definition	Meaning
CFL	$= \frac{u\,\Delta t}{\Delta x}$	Courant–Friedrichs–Lewy number
Fr	$= \frac{\varrho_{in} u_0^2}{g\,d\,\lvert\varrho_a - \varrho_{in}\rvert}$	Froude number
Ma	$= \frac{u_0}{a_s}$	Mach number
$\mathrm{Pr_t}$	$= \frac{c_{p,t}\,\mu_t}{\lambda_t}$	turbulent Prandtl number
Re	$= \frac{u_0 d \varrho_{in}}{\mu_{in}}$	Reynolds number
R_ϱ	$= \frac{\varrho_{in}}{\varrho_a}$	density ratio
$\mathrm{St_0}$	$= \frac{\varrho_p d_p^2 \lvert\hat{u}_0 - \hat{u}_{0,p}\rvert}{18\mu_{in} d}$	exit Stokes number
$\mathrm{X_F}$	$= \mathrm{Fr}^{-\frac{1}{2}} \left(\frac{\varrho_d}{\varrho_\infty}\right)^{-\frac{1}{4}} \frac{x}{d_R}$	buoyancy parameter
Π_1	$= \frac{V^*}{V} = \frac{(p_0 - p_\infty)^{1/2} d_2^2\, t_{\mathrm{dis}}\, \kappa}{V \left(\frac{p_0 M}{R\,T_0}\right)^{1/2}}$	similarity discharge number
κ	$= \frac{c_p}{c_v}$	heat capacity ratio

Constants

Symbol	Meaning	Value
C_{CORNER}	corner parameter of the GEKO model	0
C_{JET}	jet parameter of the GEKO model	0.9
C_{MIX}	mixing parameter of the GEKO model	0.30
C_{NW}	Near wall parameter of the GEKO model	0.5
C_{Realize}	GEKO model constant	0.577
C_{SEP}	separation parameter of the GEKO model	2.2
$C_{\varepsilon 1}$	k-ε model constant	1.44
$C_{\varepsilon 2}$	k-ε model constant	1.92
C_μ	k-ε model constant	0.09
$C_{\omega 1}$	auxiliary coefficients for GEKO model	1.7
$C_{\omega 2}$	auxiliary coefficients for GEKO model	1.4
g	gravitational acceleration	9.81 m s^{-2}
R	ideal gas constant	8.3145 J mol^{-1} K^{-1}
σ_k	k-ε model constant	1
σ_ε	k-ε model constant	1.3
σ_ω	GEKO model constant	2

π	mathematical constant	3.1415

Indices

Index	Meaning
a	ambient gas
cl	condition on the centre line
dis	condition at the end of the discharge
g	index for sensor number
i	index for coordinate direction
in	injected gas
j	index for coordinate direction
h	index for sensor number
H	mesh spacing reference mesh
$2H$	double mesh spacing relative to the reference mesh
$4H$	quadruple mesh spacing relative to the reference mesh
k	index for coordinate direction
P	particle
s	spreading domain
t	turbulent
v	vessel
0	outlet, initial
1	point inside the vessel
2	point at the vessel outlet
∞	infinite point in the non-affected ambient atmosphere

Abbreviations

Abbreviation	Meaning
BSA	burst spectrum analyser
CFD	computational fluid dynamics
C. & R.	Chen and Rodi
exp.	experimental
FILM	frictional and inertial loss model
GEKO	generalised k-ω turbulence
ILM	inertial loss model
LDA	laser Doppler anemometry
LES	large-eddy simulations
num.	numerical
PDA	phase Doppler anemometry
PIV	particle image velocimetry
W. & F.	Wygnanski and Fiedler

1. Introduction and motivation

In the period from 1960 to 2003, there were 242 documented accidents involving storage vessels in industrial facilities. The 10 worst accidents alone caused a financial damage of 1.204 billion US dollars (Chang and Lin, 2006).
Therefore, the unplanned release of pressurised gases is a relevant safety scenario in process engineering (Loerbroks and Mitropetros, 2017). In addition, controlled pressure relief to avoid safety-critical conditions is another scenario that has to be considered in process engineering. Hydrogen is one of the most important energy sources of the future (Rosen and Koohi-Fayegh, 2016). During the production, transport, storage and use of hydrogen, situations can arise where it has to be vented into the environment in a controlled manner (Najjar, 2013). It is especially important in these cases of flammable or toxic gases to be able to predict the process of gas discharge.

In the present work, a compressible, transient, subcritical gas release is considered. For this purpose, the pressure relief is divided into two basic fluid mechanical problems: first, the outflow from a vessel, where predictions of the conditions inside the vessel and the outflow duration are particularly important; and second, the consideration of a transient free jet, which is formed during the outflow into the environment. Even though these are basic problems of fluid mechanics, there are still some open points. For example, until this work, there has been no universal model for predicting the discharge duration of subcritical vessel discharges. Furthermore, there are still no experimental studies on the velocity field of free jets, which are formed during transient vessel discharges. In addition, it is unclear whether and what influence the Reynolds number has on the propagation of a free jet. For example, according to Pope (2015), there is no dependence of the Reynolds number on the propagation of a free jet and the observed influences of the Reynolds number are due to measurement inaccuracies. However, Rushton (1980), for example, gives a specific correlation between the Reynolds number and the velocity field of a free jet.

1.1. Objective

Within the scope of this work, the following research questions are to be answered:

1. What is a self-similar approach to describe a subcritical vessel outflow?
2. How can the outflow duration be determined by simple means?
3. What influence does the Reynolds number have on the propagation of subcritical free jets?
4. What influence does the density ratio have on the propagation of subcritical free jets?
5. Can a self-similar propagation also be observed for transient free jets?
6. Are the experimental results of the free jets replicable with numerical simulations?
7. Is the new generalised k-ω turbulence (GEKO) model superior to the standard k-ε turbulence model for the simulation of round free jets?

1.2. Outline

The research questions will be worked through and answered using the following outline. In chapter 2, the theoretical principles for describing a gas free jet are presented and the state of the art is discussed. The methods in the form of the test facility for the experimental investigations, the measurement principles and some basics of computational fluid dynamics are then explained in chapter 3. The complete test facility is specifically designed and optimised for the requirements. Among other things, a special mechanism was developed for the sudden and reproducible opening of the custom-designed vessel.

Since the propagation of a free jet depends to a decisive degree on the conditions at the nozzle outlet, and thus in the vessel, the temporal behaviour within the vessel is considered in chapter 4. Here, an attempt will be made to derive the first self-similar outflow model to describe the temporal conditions in the vessel. The ideal target would be to identify a dimensionless number that can be used to describe any subcritical discharge based on the Π-theorem according to Buckingham (1914). The model is then validated using numerical simulations and experimental investigations.

After the conditions inside the vessel have been considered, the velocity field, which is formed when the gas flows out into the free environment, is investigated further in chapter 5. Here, the pressure reliefs of density-neutral air, less-denser helium and denser carbon dioxide free jets will be investigated experimentally. In addition to the conditions inside the vessel, such as pressure and temperature, the velocity field of the transient vessel discharges is measured for the first-time using laser Doppler anemometry (LDA) and phase Doppler anemometry (PDA). Here, the universal self-similar behaviour of a free jet and the influence of the density ratio of the injected gas to the ambient gas is investigated.

In chapter 6, the experimental findings are reproduced and verified using computational fluid dynamics (CFD) simulations. In this way, for example, disturbance effects such as buoyancy can be specifically eliminated. The validation of the numerical simulations based on experimental data provides the basis for transferring the results to other systems that are very difficult to investigate in reality due to toxicity or explosion hazards. The data of chapter 5 and 6 have been analysed in cooperation with the Statistical Consulting and Analysis Centre for Higher Education TU Dortmund University to ensure a sound statistical evaluation.

Finally, chapter 7 summarises the thesis and gives an outlook about future research areas that should be further explored based on this work. The procedure of the work is summarised in Figure 1.1.

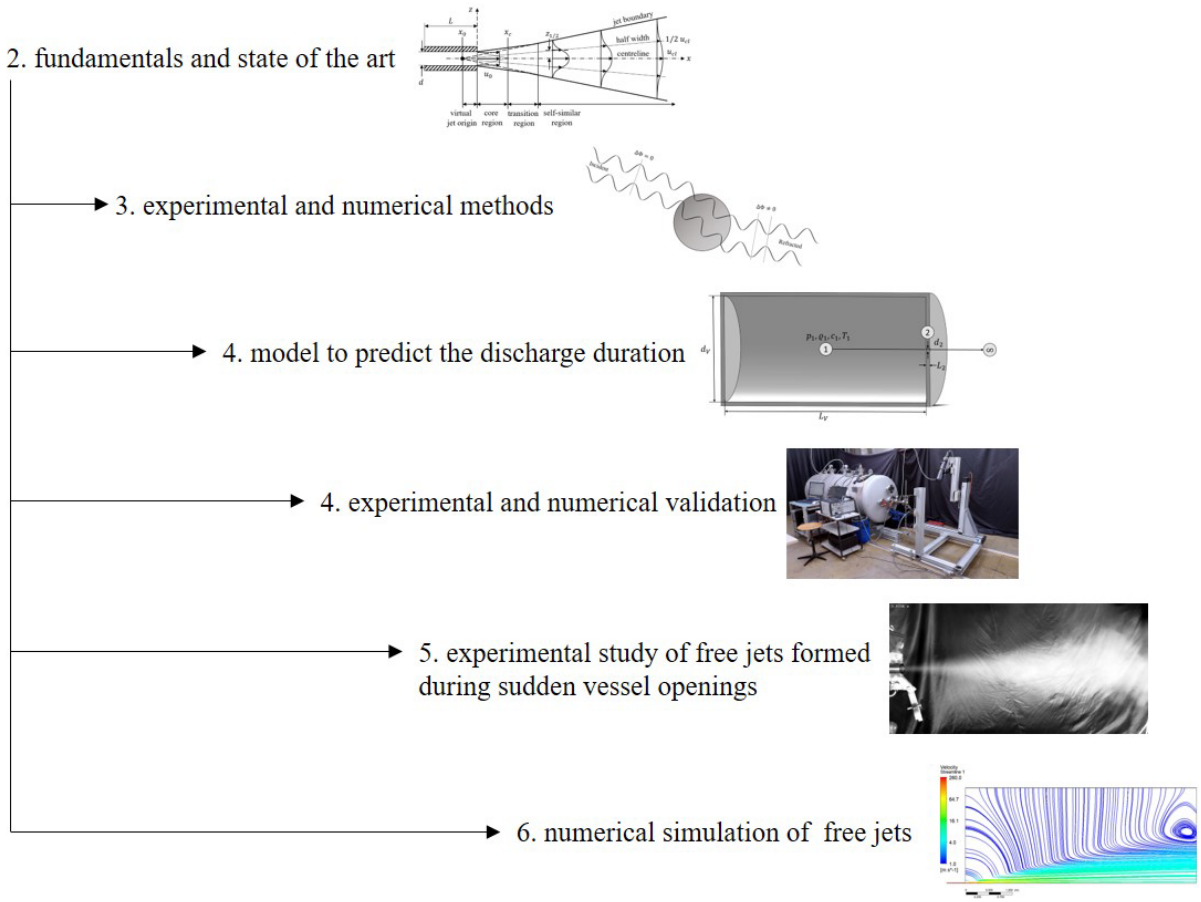

Figure 1.1.: Graphical abstract of the procedure of this dissertation. Modified from PA2 and PPA1.

2. Fundamentals

This chapter will give an overview of the theoretical background important for this work. In particular, the physical fundamentals for the description of a free jet are presented. This includes the introduction of characteristic quantities and dimensionless numbers. A literature review will then be carried out and the controversially discussed questions will be highlighted in more detail.

2.1. Free jet theory

According to Schlichting and Gersten (2006), a free jet describes an outflow into an environment without boundary walls. Figure 2.1 shows a sketch of an axisymmetric free jet, including some characteristic regions and parameters in the propagation area. A Cartesian coordinate system is used, with the x-direction aligned with the nozzle axis, the positive z-direction is going upwards and the positive y-direction is orthogonal on the view plane. The origin with $x = 0$, $y = 0$, $z = 0$ is at the nozzle outlet. The velocity components in the x, y and z direction are denoted by u, v and w, respectively. The centre line defines the course of the maximum axial velocity $u_{cl}(x)$. For the case of an axisymmetric round jet with the coordinate origin in the centre of the nozzle outlet, the centre line is defined as $\vec{x} = (x, 0, 0)$. To delimit the free jet from the environment, the free jet boundary is defined. According to Schlichting and Gersten (2006), the free jet boundaries are defined by the region in which the free jet entrains the practically stationary ambient gas due to viscosity, thus leading to a widening of the free jet. Quantitatively, the free jet boundaries are defined by those radial distances at which $u(x, z)/u_{cl}(x) = 0.01$ applies. Here u_{cl} is the centre-line velocity in axial direction. By extending the free jet boundaries from the self-similar region in the direction of the nozzle exit, the virtual jet origin is determined at the intersection of the lines. The virtual jet origin x_0 represents the location where the free jet would originate if it came from a point source.

Outlet geometries such as convergent nozzles, orifices and pipes have been studied in the literature (Mi et al., 2000). Hereby, the velocity fields of these outlet geometries should differ somewhat according to George (1989). In this dissertation, a pipe is deliberately examined, because this corresponds to the standardised geometry of an exhaust opening for emergency pressure relief according to Ernst et al. (2015). In the present case, a $L = 400$ mm long pipe with a diameter $d = 25$ mm is used.

[PPA1] Parts of this chapter are based on the article: Measurement of the Reynolds number dependence of a transient air jet from a pressure vessel by M.-D. Fischer, F. Ryll and K. Boettcher; it was first published as preprint article on Research Square, 2022 and is licensed under a Creative Commons Attribution 4.0 International License (http://creativecommons.org/licence/by/4.0/).

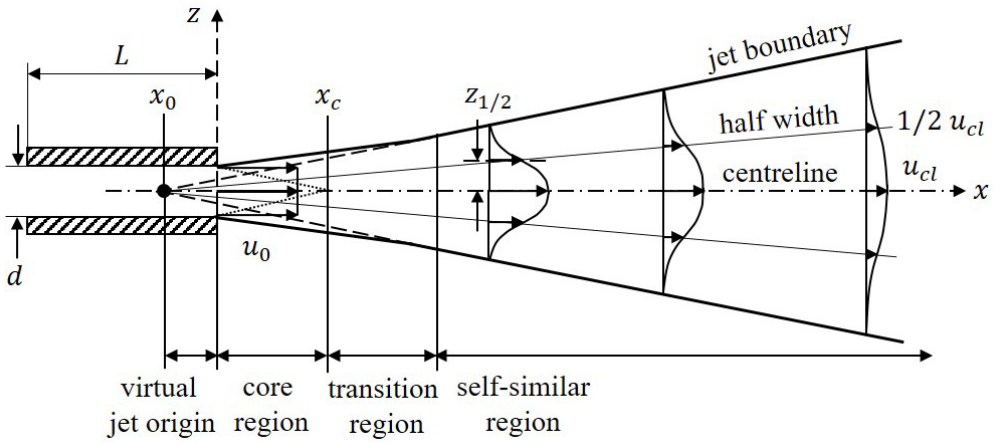

Figure 2.1.: Defining sketch of an axisymmetric free jet. Reproduced from PPA1.

A distinction is made between three regions. In the core region, which converges conically from the nozzle edge, the same flow conditions prevail as at the nozzle outlet. In this region, there is almost no mixing with the surrounding gas. According to Rajaratnam (1976), this region is defined by the core length $x_c \approx 6\, d$. According to Grandchamp and van Hirtum (2013) the core length x_c depends on the nozzle geometry, the turbulence intensity and density ratio. Hrycak et al. (1974) showed that the core length x_c is independent of the Reynolds number for turbulent free jets and is directly proportional for laminar free jets. According to Milanovic and Hammad (2010), the fully-developed flow region from $25 \leq x/d$ is self-similar and a self-preserved flow exists, in which the radial profile of the axial velocity component $u(z)$ is modelled with a Gaussian distribution according to Chen and Rodi (1980). According to Chen and Rodi (1980), a velocity field is considered self-similar if one velocity and one length scale are sufficient to describe the entire velocity field as a function of only one geometrical variable. Between the core region and the self-similar region, $6 \leq x/d \leq 25$ is the transition region in which a continuous transition of the flow properties takes place.

According to Schlichting and Gersten (2006), the velocity profile on the centre line $u_{cl}(x)$ can be modelled with a hyperbola

$$\frac{u_{cl}(x)}{u_0} = \frac{K_{1,u} d_e}{x - x_0}, \tag{2.1}$$

where u_0 is the velocity at the outlet and $K_{1,u}$ is the velocity decay constant, which is the characteristic parameter to describe the decrease of the maximal velocity along the jet axis x. A greater decay constant corresponds to a smaller velocity decrease and vice versa. Furthermore, d_e is the effective diameter according to Thring and Newby (1953)

$$d_e = d \left(\frac{\varrho_{in}}{\varrho_a}\right)^{1/2} = d\, R_\varrho^{1/2}, \tag{2.2}$$

which takes the density ratio R_ϱ of the injected gas at the pipe exit ϱ_{in} to the ambient gas density ϱ_a into account. The density of the injected gas at the pipe exit ϱ_{in} corresponds to the density of the gas in the vessel with ambient pressure and the temperature present at the vessel outlet. This results from the basic fluid mechanical assumption that the ambient pressure always prevails at the outlet for subcritical flows. To make this hyperbolic character more visible, the inverted equation is often used because this results in a linear function:

$$\frac{u_0}{u_{cl}(x)} = \frac{1}{K_{1,u}}\frac{x}{d_e} - \frac{x_0}{K_{1,u}\,d_e} \tag{2.3}$$

The velocity decay constant $K_{1,u}$ can be determined from the gradient and the virtual jet origin x_0 from the intercept of the linear function (2.3). These diagrams make deviations from a linear behaviour more visible, especially for jet positions that are further away. The radial velocity profile of the axial velocity in the self-similar region can be approximated with a Gaussian profile according to Chen and Rodi (1980):

$$\frac{u(x,z)}{u_{cl}(x)} = \exp\left(-A_u\left(\frac{z}{x-x_0}\right)^2\right). \tag{2.4}$$

Here, A_u is a spreading constant, which is less common in literature. More commonly, the half width $z_{0.5u}$ is used to describe the spreading behaviour of a free jet. According to Squire and Trouncer (1944), the jet half width $z_{0.5u}$ is the location where the velocity is just half as great as on the centre line $u(x, z_{0.5u}) = 0.5\ u_{cl}$, which behaves linearly in a good approximation

$$z_{0.5u} = K_{2,u}(x - x_0). \tag{2.5}$$

Here, $K_{2,u}$ is the spreading rate, which is the characteristic parameter to describe the propagation in radial direction and the increase of the jet width with increasing jet length x. A greater spreading rate $K_{2,u}$ corresponds to a greater spreading angle of the free jet. Since a point-like measurement method is used, it is unlikely to measure at the half width $z_{0.5u}$ exactly. Therefore, the spreading rate is determined from the fit of the velocity profile according to equation (2.4):

$$K_{2,u} = \sqrt{\frac{\ln(0.5)}{-A_u}}. \tag{2.6}$$

For a self-similar flow, there appears to be a constant relation between the decay constant and the spreading rate $K_{1,u} \cdot K_{2,u} = 0.55$ according to Pope (2015). As can be seen in section 2.1.1, some authors observed a dependency of the decay constant $K_{1,u}$ and spreading rate $K_{2,u}$ from the Reynolds number:

$$\mathrm{Re} = \frac{u_0 d \varrho_{in}}{\mu_{in}}. \tag{2.7}$$

Here, μ_{in} is the dynamic viscosity of the injected gas. The Reynolds number is used to estimate the ratio of the inertial and frictional forces, and further determine whether a flow is laminar or turbulent. For the case of a free jet, however, no clear limit value has yet been defined above which a free jet is defined as

turbulent. Thus, the transition to a transient free jet depends on the exact jet exit conditions. Values from Re = 300 according to Reynolds (1962) to Re = 15 000 according to Spalding (1979) can be found in the literature, above which a free jet is said to be fully turbulent. However, the experiments carried out here are all clearly in the turbulent range with a Reynolds number of 30 000 ≤ Re ≤ 600 000, which is why the deviating behaviour of a laminar free jet is not discussed. Another dimensionless number is the Mach number

$$\mathrm{Ma} = \frac{u_0}{a_s}, \tag{2.8}$$

which describes the ratio of the outlet velocity u_0 to the speed of sound a_s

$$a_s = \sqrt{\kappa \frac{RT}{M}}\,. \tag{2.9}$$

Here, κ is the heat capacity ratio, R is the ideal gas constant, T is the absolute gas temperature and M is the molar mass of the gas (Zierep, 2018). According to Lau (1981), the Mach number is supposed to have an influence on the velocity decay constant $K_{1,u}$, spreading rate $K_{2,u}$ and the core length x_c.

Since free jets with a density ratio $R_\varrho \neq 1$ are also investigated, an estimate must be made as to when buoyancy should be taken into account. The influence of buoyancy is especially relevant for horizontal free jets because they are investigated here. Thus, buoyancy effects lead to a shift of the centre line relative to the x-axis. Chen and Rodi (1980) introduced a dimensionless buoyancy number

$$\mathrm{X}_F = \mathrm{Fr}^{-\frac{1}{2}} R_\varrho^{-\frac{1}{4}} \frac{x}{d}, \tag{2.10}$$

where Fr is the Froude number, which is used to estimate the ratio of inertial and buoyant forces, and is defined as follows

$$\mathrm{Fr} = \frac{\varrho_{in} u_0^2}{g\, d\, |\varrho_a - \varrho_{in}|}. \tag{2.11}$$

Here, $g = 9.81$ m/s² is the gravitational acceleration. According to Chen and Rodi (1980) a free jet is no longer dominated by inertial forces for $\mathrm{X}_F > 0.5$ and is in transition to a buoyancy jet. This limit is used in the later investigations for the classification into buoyancy-influenced free jets.

This work is limited to subcritical outflows. Subcritical conditions are present if the critical pressure ratio is smaller than the ratio of the ambient pressure p_∞ to the initial pressure inside the vessel p_0

$$\frac{p^*}{p_0} = \left(\frac{2}{\kappa + 1}\right)^{\frac{\kappa}{\kappa - 1}} < \frac{p_\infty}{p_0}. \tag{2.12}$$

The critical pressure ratio is determined with the heat capacity ratio κ. The case where the pressure ratios are just equal is called the critical pressure ratio. This indicates the transition from supercritical to subcritical pressure conditions (Zierep, 2018).

2.1.1. Density-neutral free jets

The following section focuses on studies that have dealt with density-neutral free jets. In particular, the dependence of the propagation on the Reynolds number will be examined. Abramovich (1963) stated that turbulent jets are not dependent on the Reynolds number in a wide range $2 \cdot 10^4 \leq \mathrm{Re} \leq 4 \cdot 10^6$. However, the spreading rate $K_{2,u}$ depends on the turbulence intensity and there would be a linear relationship between these two. On the basis of the literature published to that date, Rushton (1980) established an approach for determining the axial velocity component $u_{cl}(x)$ for rotationally symmetrical free jets as a function of the Reynolds number.

Chen and Rodi (1980) reviewed many experimental data on vertical turbulent buoyant jets in addition to their own experimental investigations. They gave a universal self-similarity for turbulent jets independent of the Reynolds number as long as the Reynolds number is great enough. Consequently, the Reynolds number is only important for deciding whether a turbulent or laminar flow is present. Although in eq. (2.1) the axial velocity decay $u(x)$ depends on the density ratio R_ϱ, which is taken into account by the effective diameter d_e, the spreading rate $K_{2,u}$ is independent of the density ratio R_ϱ. George (1989) questions the self-similar behaviour of a free jet based on an analytical asymptotical solution of the conservation equations. Accordingly, the common constants such as the decay constant $K_{1,u}$ and the spreading rate $K_{2,u}$ would have to be reconsidered and further constants would have to be introduced to capture the different outflow conditions.

Panchapakesan and Lumley (1993a) observed deviations from the decay constant $K_{1,u}$ and turbulence intensities of Wygnanski and Fiedler (1969), which have long been considered to be a standard. In particular, they could not confirm if the deviations were due to the different Reynolds numbers Re. In flows investigated by Panchapakesan and Lumley (1993a) the Reynolds number was Re = 11 000, i.e., one order of magnitude smaller than the Reynolds number of Wygnanski and Fiedler (1969). However, Capp (1983) re-examined the data of Wygnanski and Fiedler (1969) and found a shortfall in the momentum flux across the jet. This was probably due to wall influences in the propagation area of the free jet that may have initiated a backflow.

Hussein et al. (1994) states that the questions of the nature of dissipation and Reynolds number dependence of a jet remain open and require further investigation. Olsson and Fuchs (1996) performed large-eddy simulations (LESs) of round jets in the range $10\,000 \leq \mathrm{Re} \leq 500\,000$ and found no notable influence of the Reynolds number Re in the self-similar region. Borée et al. (1996) performed experimental investigations of sudden velocity decreases in free jets and observed a smaller decay constant $K_{1,u}$ and virtual origin x_0 for the jet with smaller Reynolds number Re. Kwon and Seo (2005) have carried out experimental studies on the Reynolds number dependence of water jets in the range

$177 \leq \mathrm{Re} \leq 5\,142$. According to these authors, a greater Reynolds number causes a slightly smaller decay constant $K_{1,u}$ and a smaller spreading rate $K_{2,u}$. Bogey and Bailly (2006) performed LES of transitional round jets to investigate the Reynolds number influence on the flow development. They observed that as the Reynolds number Re increases, the decay constant $K_{1,u}$ increases, which corresponds to a slower velocity decay, and simultaneously the spreading rate $K_{2,u}$ decreases.

Pope (2015) supports the statement that in an ideal experiment the Reynolds number Re is the only non-dimensional parameter, but he clearly states that the propagation of a round free jet does not depend on the Reynolds number Re. The small deviations that exist in literature are due to experimental inaccuracies. For example, Romano (2020) performed experimental investigations of turbulent orifice round water jets based on particle image velocimetry (PIV) measurements in the range $2\,000 \leq \mathrm{Re} \leq 70\,000$. Thus, the Reynolds number Re can be observed to have an influence up to 15 outlet diameters downstream and disappears almost completely thereafter. Bonelli et al. (2021) have performed LES in the range $\mathrm{Re} \leq 20\,000$ and observed that the decay constant $K_{1,u}$ increases with increasing Reynolds number Re, corresponding to a slower velocity decay, and simultaneously the spreading rate $K_{2,u}$ decreases. This agrees with the observations of Bogey and Bailly (2006), who had studied this behaviour at greater Reynolds numbers. Table 2.1 summarises the literature reviewed, which indicates whether it is a theoretical (theo.), numerical (num.), experimental (exp.) or review work. Here, $f(\mathrm{Re})$ indicates, that the authors have qualitatively observed a dependence on the Reynolds number but it was not defined quantitatively. The type of fluid in the last column indicates that the work covers both gases and liquids. The product of the mean decay constant $K_{1,u}$ and the spreading rate K_{2u}, averaged over all of the results in literature, is $K_{1,u} \cdot K_{2,u} = 0.58$. This value is, therefore, an indication of momentum conservation.

Table 2.1.: Decay constants $K_{1,u}$ and spreading rates $K_{2,u}$ for density neutral free jets, published by several authors. Modified from PPA1.

Authors	Based on	Re	x/d	$K_{1,u}$	$K_{2,u}$	Type
Abraham (1996)	num.	-	-	6	0.085	gas
Abramovich (1963)	review	$2{\cdot}10^4$ - $4{\cdot}10^6$	-	6.32-7.27	0.096	fluid
Bogey and Bailly (2006)	num.	1 700 - 400 000	-	$f(\mathrm{Re})$	$f(\mathrm{Re})$	fluid
Bonelli et al. (2021)	num.	10 000 - 20 000	-	$f(\mathrm{Re})$	$f(\mathrm{Re})$	gas
Borée et al. (1996)	exp.	6 000	0 - 60	5.75	0.092	air
		12 500	0 - 60	5.99	0.091	air
Chen and Rodi (1980)	review	> 10 000	-	6.2	0.086	gas
Craske (2016)	num.	6 810	28 - 55	6.06	0.096	gas
Ferdman et al. (2000)	exp.	$2.4{\cdot}10^4$	0 - 80	6.7	0.088	air
Hinze and van der Hegge Zijnen (1949)	exp.	20 100 - 83 750	0 - 20	6.39	0.083	air
Hussein et al. (1994)	exp.	95 500	30 - 120	5.8	0.094	air
Kwon and Seo (2005)	exp.	1 305	2.5 - 80	5.5	0.140	water
		2 163		5.5	0.114	
		3 208		5.5	0.113	
		5 142		5.5	0.106	
Panchapakesan and Lumley (1993a)	exp.	11 000	30 - 160	6.06	0.096	air
Rajaratnam (1976)	theo.	-	-	6.3	0.100	fluid
Romano (2020)	exp.	2 000 - 70 000	< 20	6.67	0.100	water
Rushton (1980)	review	-	-	$1.41\ \mathrm{Re}^{0.135}$	-	fluid
Spalding (1979)	theo.	> 15 000	-	6.57	0.085	fluid
Tollmien (1926)	theo.	-	-	6.44	0.082	fluid
Witze (1974)	review	-	-	$f(\mathrm{Ma}, R_\varrho)$	-	gas
Weisgraber and Liepmann (1998)	exp.	5 500 - 16 000	15 - 30	6.7	$f(\mathrm{Re})$	water
Wygnanski and Fiedler (1969)	exp.	10^5	5 - 100	5.4	0.086	air
mean				6.05	0.096	
standard deviation				0.50	0.014	

2.1.2. Non-density-neutral free jets

According to Mi et al. (2001), it is easier to prove the self-similarity of a free jet based on scalar quantities such as concentration or mass fraction. According to Sreenivasan (1996), a self-similarity of a scalar quantity in an inhomogeneous shear flow can only exist if not only one but all velocity components are self-similar. A great number of studies have, therefore, dealt with the propagation of scalar quantities in free jets (Gerold, 2015; Mi et al., 2001; Pitts, 1991b, 1991a; Richards and Pitts, 1993).

However, Fischer (1979) found that there are differences in the propagation of the concentration and velocity in free jets of almost 20%. The reason for these differences in the propagation of concentration and velocity has led to unresolved speculation. Since the propagation of a scalar quantity does not allow for an exact conclusion about the velocity field, this literature review is limited to work that considers the velocity field (as studied in the present work). Furthermore, this literature review does not consider work dealing with variable density jets into an air co-flow, such as Amielh et al. (1996) and Sautet and Stepowski (1995). For example, the decay constants $K_{1,u}$ in a co-flow were up to 40 % greater and thus, the flow conditions are not comparable with a free jet into a quiescent environment.

Keagy and Weller (1949) investigated the velocity and concentration fields of stationary nitrogen, carbon dioxide and helium jets. It was also observed that the non-density-neutral free jets of helium and carbon dioxide show a self-similar behaviour for a certain axial distance $x > 10\ d$. Furthermore, the spreading rate $K_{2,u}$ showed a dependence on the density ratio R_ϱ. Thus, the spreading rate $K_{2,u}$ becomes smaller as the density ratio R_ϱ increases.

Thring and Newby (1953) studied the combustion of turbulent jet flames. They found that all free jets are self-similar if the Reynolds number Re is above a certain minimum. Furthermore, the spreading rate $K_{2,u}$ of a free jet is only a function of the Reynolds number Re. However, the dependence of the spreading rate $K_{2,u}$ on the Reynolds number Re is so weak that the self-similarity is still valid. As far as the axial velocity profile is concerned, Thring and Newby (1953) introduced the concept of an effective diameter d_e as a characteristic length scale, which led to the existence of a universal decay constant $K_{1,u}$ independent of the density ratio R_ϱ.

Birch et al. (1978) studied the velocity field of a methane jet using LDA, in addition to the concentration field using Raman spectroscopy. They used a pipe with a diameter of d = 12.65 mm and a length-to-diameter ratio of L/d = 50. This resulted in a fully-developed pipe flow at a Reynolds number of Re = 16 000. They observed that the density influence for the axial velocity decay can be captured by the effective diameter d_e according to Thring and Newby (1953), and thus the decay constant $K_{1,u}$ is independent of the density ratio R_ϱ.
Chen and Rodi (1980) investigated the influence of the density ratio R_ϱ on the decay constant $K_{1,u}$ and spreading rate $K_{2,u}$ based on a review of the experimental data. Experimental data from stationary air, helium and carbon dioxide jets were used. As a result, there can be no self-similarity within the transition jet region because the density ratio R_ϱ is still changing there. However, this is always followed by a region where the density ratio is $R_\varrho \approx 1$ and self-similarity is present. According to Chen and Rodi (1980), the axial velocity decay is influenced by the density ratio R_ϱ, but this can be captured by the effective diameter d_e (cf. eq. (2.2)) according to Thring and Newby (1953). Thus, the decay constant $K_{1,u}$ remains independent of the density ratio. Contrary to the axial velocity decay, the spreading rate $K_{2,u}$ is independent of the density ratio R_ϱ according to Chen and Rodi (1980).

So et al. (1990) carried out experimental investigations on helium-air binary gas jets into an air environment. The density ratio was R_ϱ = 0.64 at a Reynolds number of Re = 4 300. A self-similar velocity profile could be observed for $x/d > 24$. Furthermore, So et al. (1990) compared their data with experimental investigations by Wygnanski and Fiedler (1969), among others, and suggested that the flow is independent of the Reynolds number Re and the density ratio R_ϱ if a self-similar state is reached in the self-similar region. So et al. (1990) determined a decay constant of $K_{1,u}$ = 5.45 and a spreading rate of

$K_{2,u}$ = 0.103. However, according to So et al. (1990), the self-similarity in non-density-neutral free jets $R_\varrho \neq 1$ cannot persist beyond a certain axial distance because density influences become noticeable.

Panchapakesan and Lumley (1993b) performed experimental investigations on vertical helium jets. At the nozzle outlet the Reynolds number was Re = 3 650 and the Froude number was Fr = 14 000. For the investigated range $50 \leq x/d \leq 120$ values of the buoyancy parameter in the range $0.69 \leq X_F \leq 1.66$ were found according to equation (2.10). Thus, the measurements were carried out in the buoyancy-affected regime. The buoyancy effect could be the reason for the slightly higher decay constant $K_{1,u}$ = 6.50 compared to other values in the literature. For vertical free jets with a density ratio $R_\varrho < 1$, the buoyancy effect leads to slower axial velocity decay.

Wang and Andreopoulos (2010) investigated the density effects in stationary, horizontal helium, nitrogen and krypton jets using PIV and high-frequency-response pressure transducers. The jets were formed at the exit of a L = 170 mm long pipe with a diameter of d = 7 mm. It was found that the spreading rate decreases from $K_{2,u}$ = 0.103 to $K_{2,u}$ = 0.048 with increasing density ratio R_ϱ. Furthermore, the spreading rate $K_{2,u}$ decreases with increasing Mach number Ma. It is noticeable that the axial velocity initially increases after emergence and then decreases. This suggests that the tracer particles that were used were too great for an ideal following behaviour. This could also be the reason for the considerably greater decay constants $K_{1,u}$ and smaller spreading rates $K_{2,u}$ compared to the rest of the literature.
Chernyavsky et al. (2014) performed LES of a vertical hydrogen jet at a Mach number of Ma = 0.3. The results were compared with experimental data from PIV measurements of air and helium jets, as well as LES data from a helium jet from Chernyavsky et al. (2011). It was observed that the spreading rate of a hydrogen jet with $K_{2,u}$ = 0.18 was greater than the previously observed spreading rates for air of $K_{2,u}$ = 0.095 and helium jets of $K_{2,u}$ = 0.105. In summary, despite the great number of studies on non-density-neutral free jets, there is no consensus in the literature.

Table 2.2.: Published decay constants $K_{1,u}$ and spreading rates $K_{2,u}$ for non-density-neutral free jets.

Authors	Based on	R_ϱ	Re	x/d	$K_{1,u}$	$K_{2,u}$	Type	Direction
Aihara (1974)	exp.	0.14	2 950	30-100	-	0.12	He	vertical
Birch et al. (1978)	exp.	0.55	16 000	0-70	5.01	-	CH_4	unclear
Chernyavsky et al. (2011)	exp.	1	10 600	0-30	6.93	0.095	air	vertical
	exp.	1	31 000	0-30	6.35	0.095	air	vertical
	exp.	0.14	4 100	0-30	5.48	0.105	He	vertical
	exp.	0.14	11 900	0-30	5.53	0.105	He	vertical
	num.	0.14	11 900	0-30	4.92	0.105	He	vertical
Chernyavsky et al. (2014)	num.	0.07	14 000	0-38	5.21	0.18	H_2	vertical
Chen and Rodi (1980)	review	0.14-1.51	>10 000	-	6.2	0.093	gas	vertical
Keagy and Weller (1949)	exp.	0.14	3 300	8-50	6.77	0.11	He	vertical
		0.96	25 300		7.02	0.089	N_2	vertical
		1.52	47 800		7.41	0.083	CO_2	vertical
Panchapakesan and Lumley (1993a)	exp.	1	11 000	30-160	6.06	0.096	air	vertical
Panchapakesan and Lumley (1993b)	exp.	0.14	3 650	50-120	6.50	0.110	He	vertical
So et al. (1990)	exp.	0.64	4 300	1-30	5.45	0.103	He/Air	vertical
Wang and Andreopoulos (2010)	exp.	0.09	11 000	0-45	16.67	0.113	He	horizontal
		0.09	25 000	0-45	24.39	0.076	He	horizontal
		0.09	40 000	0-45	25.00	0.081	He	horizontal
		0.72	34 000	0-45	7.52	0.086	N_2	horizontal
		0.80	74 000	0-45	9.17	0.067	N_2	horizontal
		0.84	122 000	0-45	10.99	0.055	N_2	horizontal
		2.44	45 000	0-45	7.14	0.051	Kr	horizontal
		2.37	91 000	0-45	7.69	0.048	Kr	horizontal

3. Methods

In this chapter, the experimental and numerical methods are addressed. This includes a short introduction to the measurement principles of LDA and PDA. After that, the experimental setup is presented. Finally, the methods of the CFD simulations are presented. These include the governing equations and turbulence models that were used.

3.1. Measurement principles

In this section, the fundamental principles of the LDA and PDA are described. The focus is on the PDA because this is not very common due to its complexity.

3.1.1. Laser Doppler anemometry

LDA is an optical, non-contact velocity measurement method that is characterised by its very high temporal and spatial resolution. The measurement volume is only a few mm³, which is why it can be considered to be a point-like measurement method. Here, two coherent laser beams meet at an angle of $\vartheta/2$ to the axis. The angle depends on the focal length and the beam distance. A defined interference fringe pattern is formed, where the fringe spacing Δx_f depends on the wavelength λ_w of the laser light and the incident angle $\vartheta/2$. A sketch of this interference fringe pattern is shown in Figure 3.1.

[PA1] Parts of this chapter are based on the article: A fast method to predict the transient, subcritical gas discharge from a pressure vessel by M.-D. Fischer and K. Boettcher; it was first published in *Chem. Eng. Sci*. 2022

[PA2] Parts of this chapter are based on the article: Similarity solution of subcritical pressure discharges from vessels for arbitrary gases by M.-D. Fischer, S. Baier and K. Boettcher; it was first published in *Chem. Eng. Sci*. 2023

[PPA1] Parts of this chapter are based on the article: Measurement of the Reynolds number dependence of a transient air jet from a pressure vessel by M.-D. Fischer, F. Ryll and K. Boettcher; it was first published as preprint article on Research Square, 2022 and is licensed under a Creative Commons Attribution 4.0 International License (http://creativecommons.org/licence/by/4.0/).

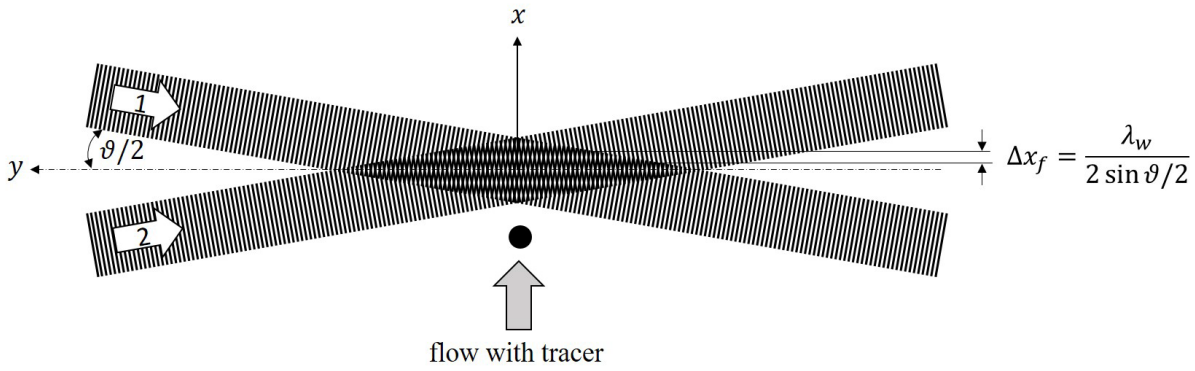

Figure 3.1.: Schematic representation of the LDA principle (Nitsche and Brunn, 2006).

If a particle passes through this interference fringe pattern, the laser light is scattered and detected by an optical sensor. The frequency

$$\Delta f = \frac{u_p}{\Delta x_f} = \frac{u_p \, 2 \sin(\vartheta/2)}{\lambda_w} \tag{3.1}$$

of the scattered light depends on the one hand on the fringe spacing Δx_f and on the other hand on the x-component of the velocity of the particle u_p. The fringe spacing Δx_f is a constant system parameter, which leads to a direct linear correlation between the particle velocity u_p and the frequency Δf of the scattered light. This accounts for the high accuracy of the measurement procedure of well below 1 % according to Albrecht et al. (2003). Further information on the LDA technique can be found in Albrecht et al. (2003) and Nitsche and Brunn (2006).

3.1.2. Phase Doppler anemometry

PDA is an extension of the LDA technique and is used to measure the particle velocity u_p in x-direction (cf. Figure 3.1) as well as the particle diameter d_p. This is a unique measurement principle because there is no other method to perform this on discrete particles with such high temporal and spatial resolution (Albrecht et al., 2003). The PDA technique is based on the fact that the incident spatially and temporally coherent laser light undergoes a phase shift depending on the particle diameter d_p. How the phase shift is initiated due to the particle is shown schematically in Figure 3.2. The velocity at which light travels in a medium depends on the refraction index. When light passes through an optically denser particle, it is slowed down. Since the incident light rays hit the particle at different locations, the distance that the light has to travel through the particle varies. Consequently, although the light rays in the particle have the same velocity, they have to cover a different distance. As a result, the light rays have a phase difference when they emerge from the particle.

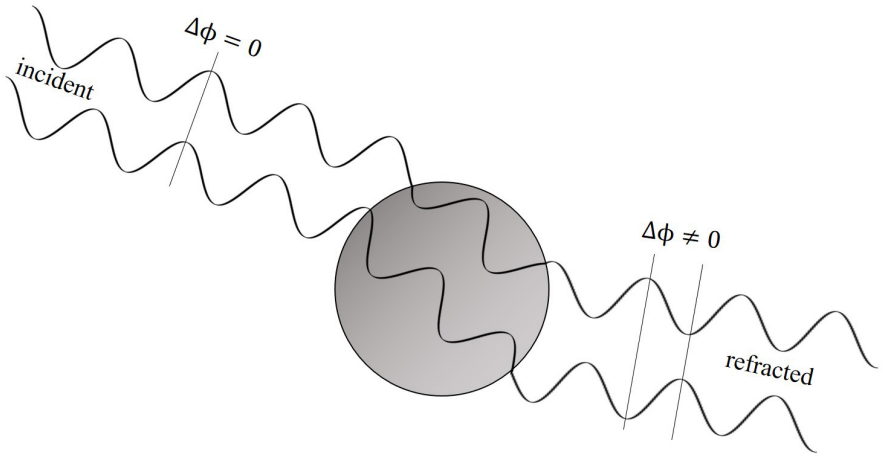

Figure 3.2.: Principle of phase shift due to refraction of incident light.

The phase shift

$$\Delta\phi_{gh} = \phi_h - \phi_g = \frac{\pi}{\lambda_w} d_p \cdot (\beta_h - \beta_g) \tag{3.2}$$

depends on the particle diameter d_p and various constant system parameters, which are captured by the phase factors β_g of the detector system. The phase factors depend on the type of light scattering mechanism. It is, therefore, essential to choose an angle between the transmitter and receiver head at which a single light scattering mode dominates almost exclusively. Figure 3.3 shows a scheme of the three most important light scattering modes for transparent particles. A distinction is made between reflection, refraction and second-order refraction. Of course, higher-order refraction mechanisms are also possible, but these are not of major relevance, and are therefore not considered here.

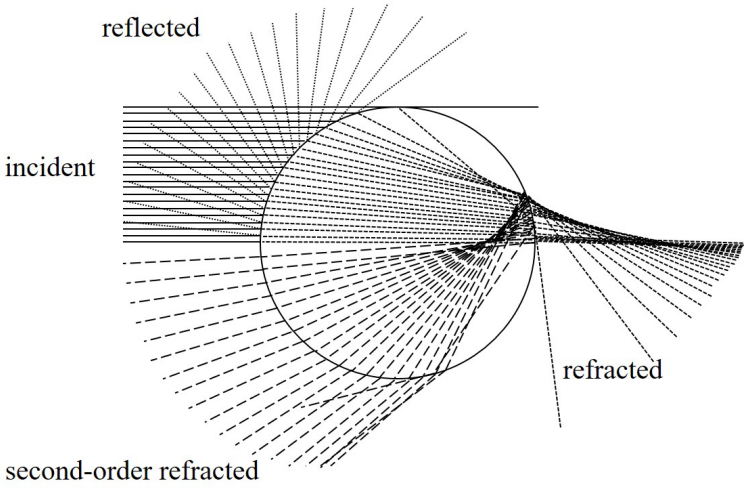

Figure 3.3.: Schematic illustration of three different light scattering modes for transparent particles according to Dantec Dynamics A/S (2011).

The optimal angle between the transmitter and receiver head φ depends on the relative refractive index between the particle and fluid phase n_{rel} and the polarisation of the laser light. Using a tool from Dantec Dynamics, an angle of $\varphi = 56°$ was selected between the transmitting and receiving head. This results in 97.9 % confidence for first-order refraction as the predominant scattering mode for the ethylene glycol tracers with $n_{\mathrm{rel}} = 1.357$ used. The phase factors β_g for first-order refraction are calculated as follows:

$$\beta_g = 2\left[\sqrt{1 + n_{\mathrm{rel}}^2 - \sqrt{2}\cdot n_{\mathrm{rel}}\cdot\sqrt{f_{g+}}} - \sqrt{1 + n_{\mathrm{rel}}^2 - \sqrt{2}\cdot n_{\mathrm{rel}}\cdot\sqrt{f_{g-}}}\right], \tag{3.3}$$

with

$$f_{g\pm} = 1 + \cos\frac{\vartheta}{2}\cdot\cos\varphi\cdot\cos\psi_g \pm \sin\frac{\vartheta}{2}\cdot\sin\psi_g. \tag{3.4}$$

Here φ and ψ_g are angles between the transmitting head and the sensors. The Figure 3.4 shows how these angles are defined. Here, ψ_g is the azimuth angle that defines the rotational position about the z-axis and φ is the scattering angle measured from the axis of the transmitting optics to the bisector of the two incident beams. For the present case the angle of the incident laser beams is $\vartheta = 5.44°$ and the scattering angle is $\varphi = 56°$. The azimuth angle ψ_g depends on the aperture mask and the sensor pair.

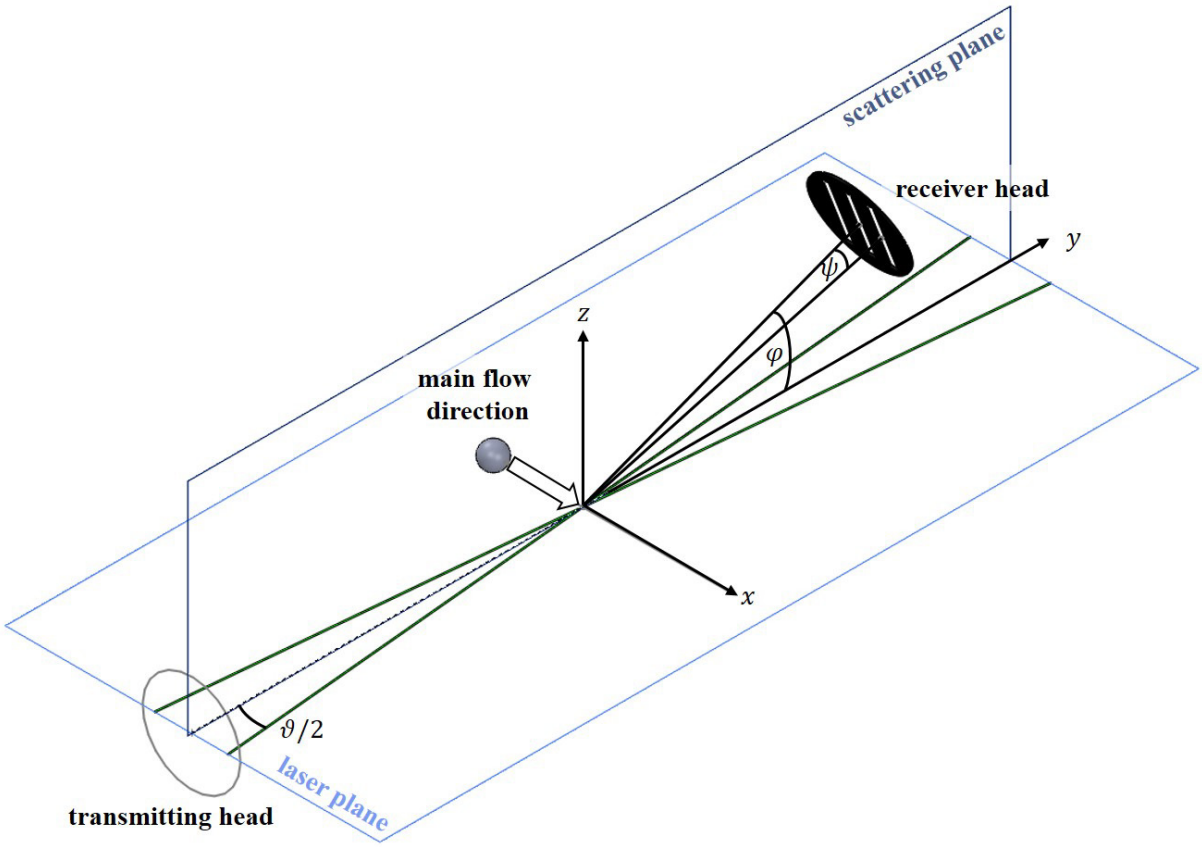

Figure 3.4.: Coordinate system used with the PDA system.

In the *112 mm Fiber PDA* system (Dantec Dynamics) that was used, two sensors are used to detect one phase shift and three sensors are used to measure two phase shifts because with the 2π-clarity of the phase shift there is an increase in accuracy and additional validation. The arrangement of the sensors is explained in Figure 3.4. The aperture mask of the receiver head has three slits. Behind the slit in negative x-direction is sensor 1, in the middle at $x = 0$ is sensor 3 and in positive x-direction is sensor 2.

In Figure 3.5, the correlation between the phase shift $\Delta\Phi_{gh}$ and the particle diameter d_p from equation (3.2) is shown in an idealised way. The characteristics of the sensor pairs 1-2 and 1-3 are given by the thick solid lines and dashed lines. For the sensor pair 1-2, the 2π-clarity is shown by the fact that there are several intersections with the characteristic line for a phase difference, and thus potentially several possible particle diameters. This means that it is not possible to distinguish between a phase shift of 2 π or 4 π, for example, because the maximum phase shift is 2 π. A second pair 1-3 is used to overcome this problem. The maximum measurable particle diameter $d_{p,\max}$ is predefined by the sensor pair 1-3 because this has the smaller gradient. For particle diameters greater than $d_p > d_{p,\max}$, the sensor pair 1-3 also has a problem with the 2π-clarity and it is no longer possible to clearly determine the particle's diameter. If even greater particle diameters are to be measured, various aperture masks can be used, which influence the characteristic lines for the sensor pairs.

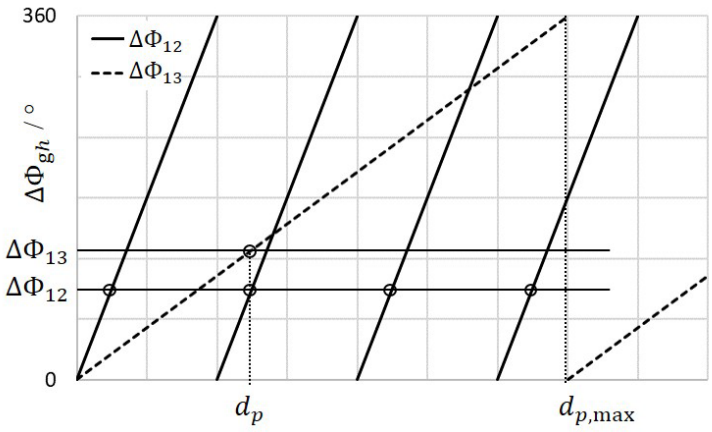

Figure 3.5.: Idealised scheme of phase shift $\Delta\phi_{gh}$ against particle diameter d_p.

3.2. Experimental setup

The used individual apparatuses and instruments are shown in a piping and instrumentation diagram in Figure 3.6 and are listed in Table 3.1. At the centre of the facility is a custom-designed stainless steel pressure vessel (Walter Ludwig, Behälter- und Anlagenbau e.K.) (E-1) with a volume of V = 2.085 m³, which was manufactured specifically for the experiments. The vessel's volume was determined by filling with water and measuring the result with an interconnected water meter for cold water (Zenner

International GmBH & Co. KG, accuracy better 1 %). The vessel is designed for a maximal positive operating pressure of 3 bar. The vessel is filled either via a compressed air network or via compressed gas cylinders (E-2) with helium or carbon dioxide. Helium 4.6 with a purity of 99.996 % and carbon dioxide 2.5 with a purity of 99.5 % are used here. The gas supply is opened or closed with valve (V-1).

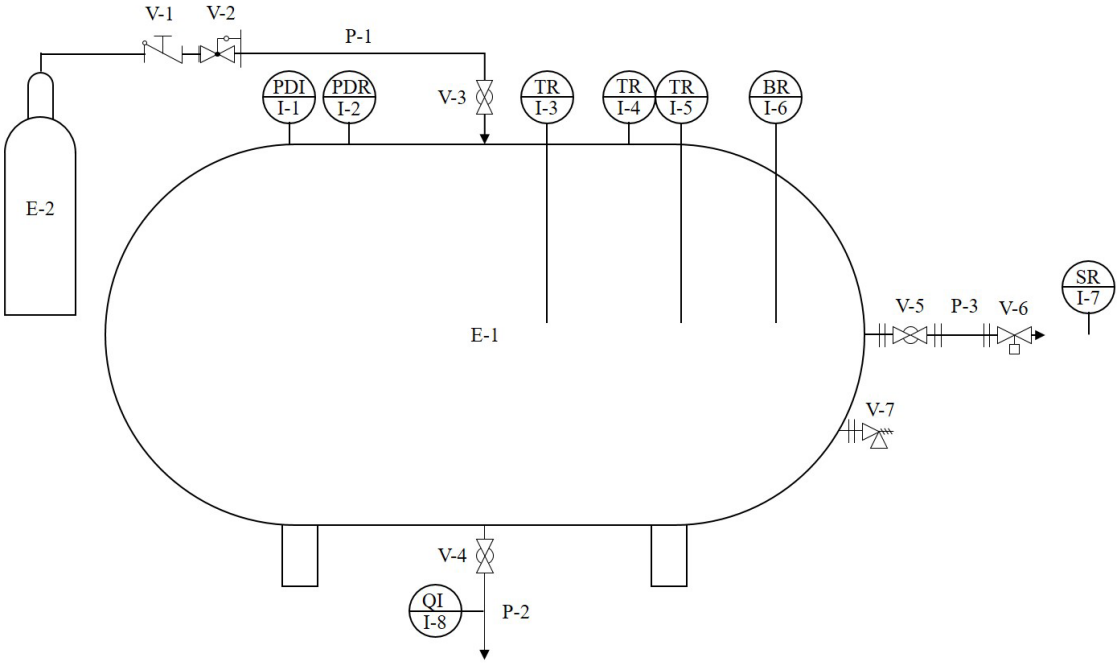

Figure 3.6.: Piping and instrumentation diagram of the experimental setup. Modified from PPA1.

Since the pressure of the gas supply is considerably greater than the positive pressure of 0.5 bar to be investigated, a pressure reducer *Kendall Model 10* (Fairchild) for air or *Constant 2000* (Messer SE & Co. KGaA) (V-2) for carbon dioxide and helium is used. The supply pipe (Festo SE & Co. KG) (P-1) is an 8 m long polyurethane hose with an inner diameter of 8 mm. The connection to the vessel is made via an extension of a push-in fitting (Festo SE & Co. KG) to a 1" ball valve (Nieruf GmbH) (V-3). The upper part of the vessel contains the access points for the measuring equipment, which are screwed into three DN100 blind flanges. An analogue 0–2.5 bar pressure display *RF100 D101* (I-1) (AFRISO-EURO-INDEX GmbH, accuracy better than $\pm$ 1.6 %) and a 0–0.6 bar pressure sensor *A-10* (I-2) (WIKA Alexander Wiegand SE & Co. KG, accuracy better than $\pm$ 0.18 %, settling time < 4 ms) are installed. For temperature measurement, a PT100 (I-3) (RS PRO, class b) and a NiCr fine-wire thermocouple (I-5) (mawi-therm Temperatur-Prozesstechnik GmbH, t_{99} = 0.5 s) are installed in a flange. The sensor heads reach into the centre of the vessel. The PT100 is used to validate the measurement results. The deviation between the PT100 and the NiCr fine-wire thermocouple for a steady-state temperature of T_{Pt100} = 288.55 K is +0.14 %. Due to the large extensive heat capacity of the vessel's, the vessel temperature is taken as the differential reference temperature. The reference temperature is measured with a temperature probe (I-4) (Driesen + Kern GmbH, accuracy better than $\pm$ 0.5 %). Its deviation from a stationary temperature is T_{Pt100} = 288.55 K is + 0.20 %.

A fog machine *N-19* (eurolite) is placed inside the vessel to generate the flow tracers. The fog liquid is an ethylene glycol-water solution with a refraction index of $n = 1.357$ and a density of ϱ_P = 1 030 kg/m³. The median particle size at the nozzle outlet is $d_{P50,0}$ = 6.07 µm. Further information on the particle size distribution and the following behaviour of the particles will be given in Figure 5.2.

Table 3.1.: Apparatus and instrument list.

Number	PCE-Category	Description	Manufacturer
E-1		Pressure vessel 2.085 m³, 3 bar	Walter Ludwig, Behälter- und Anlagenbau e.K.
E-2		Compressed gas cylinder, He 4.5, 300 bar, 50 L or CO_2 2.5, 57.25 bar, 37.5 kg	Messer SE & Co. KGaA
V-1	H	Valve	Messer SE & Co. KGaA
V-2	H	Pressure reducer	Messer SE & Co. KGaA
V-3	H	1" ball valve	Nieruf GmbH
V-4	H	1" ball valve	Nieruf GmbH
V-5	H	1" ball valve	Nieruf GmbH
V-6	N	Quick valve	workshop TU Dort-mund/Fischer
V-7	Y	Safety valve SF01, response pressure 2 bar	Nieruf GmbH
P-1		Supply line, 8 mm, 8 m, PUR	Festo SE & Co. KG
P-2		Outlet 1 " fabric hose	Festo SE & Co. KG
P-3		Discharge pipe, d = 25 mm, L = 400 mm	workshop TU Dort-mund/Fischer
I-1	PDI	Pressure indicator 0-2.5 bar, ½ "	AFRISO-EURO-INDEX GmbH
I-2	PDR	Pressure sensor A-10, 0-600 mbar or 0-1600 mbar	WIKA Alexander Wie-gand SE & Co. KG
I-3	TR	PT100	RS PRO
I-4	TR	cold junction reference, DKRF300S	Driesen + Kern GmbH
I-5	TR	NiCr fine-wire thermocouple	mawi-therm Temperatur-Prozesstechnik GmbH
I-6	BR	Camera C270	Logitech international S.A.
I-7	SR	60X FiberFlow LDA, 112 mm Fiber PDA	Dantec Dynamics
I-8	QI	Gas concentration sensor	SOLO Divesoft

To check the amount of fog added, a camera and a lamp (I-6) were installed inside the vessel. The free jet to be examined is released via the outlet pipe (P-3), which is a stainless-steel pipe with a diameter of d = 25 mm and a length of L = 400 mm. A ball valve (V-5) is installed at the beginning of the pipe section to close the vessel for a longer period of time. For the sudden opening of the vessel during the experiment, valve (V-6) is used. Since all of the usual valves available on the market have opening times that are too great to guarantee a sudden opening of the vessel, a "quick valve" was specially designed. The opening mechanism is able to open the vessel reproducibly in 34 ± 1 ms.

The valve (V-6) is opened remotely by means of a linear actuator *LEZ 1* (isel Germany AG). An *IMC1-10* (isel Germany AG) is used as the controller. The controller is connected to a computer that in addition to controlling the opening of the valve (V-6), also records the data from the pressure sensor (I-2) and the temperature sensors (I-3, I-4 and I-5) at a sampling rate of 4.5 Hz or 16 Hz. Digital multimeters *34144A* (Agilent Technologies, Inc.) are used to convert the sensors' signals.

A *DN50/DN50 SF01* safety valve (Nieruf GmbH) (V-7) is used to prevent safety-critical conditions in which the permissible vessel pressure is exceeded. The instrument (I-7) is representative of the entire technology of the PDA. Information about the measurement principle of a PDA can be found in section 3.1.2. A PDA system from Dantec Dynamics is used here. Despite the greater effort measuring particle size alongside particle velocity using the PDA, it has proven to be very useful—large particles that may not have the gas velocity could be cut off. For more information, see Figure 5.3. A water-cooled 8W argon ion laser *95* (Lexel Laser INC) with two dominant wavelengths of $\lambda_w = 488$ nm and $\lambda_w = 514.5$ nm. Here, the green $\lambda_w = 514.5$ nm wavelength is used because it has a higher intensity, and should therefore provide a better signal.

The transmitting head is a *60X FiberFlow* (Dantec Dynamics). The transmitting head has a focal length of 400 mm and the beam spacing is 38 mm. This leads to an angle of intersection between the two incident laser beams of $\vartheta/2 = 2.72°$. A *112 mm Fiber PDA* (Dantec Dynamics) is used as the receiving head. The focal points of the transmitting and receiving heads must be aligned in the three spatial directions x, y, z with an accuracy better than 100 µm and the three spatial angles $\varphi_{xy}, \varphi_{xz}, \varphi_{yz}$ must also be adjusted as accurately as possible (cf. Figure 3.7).

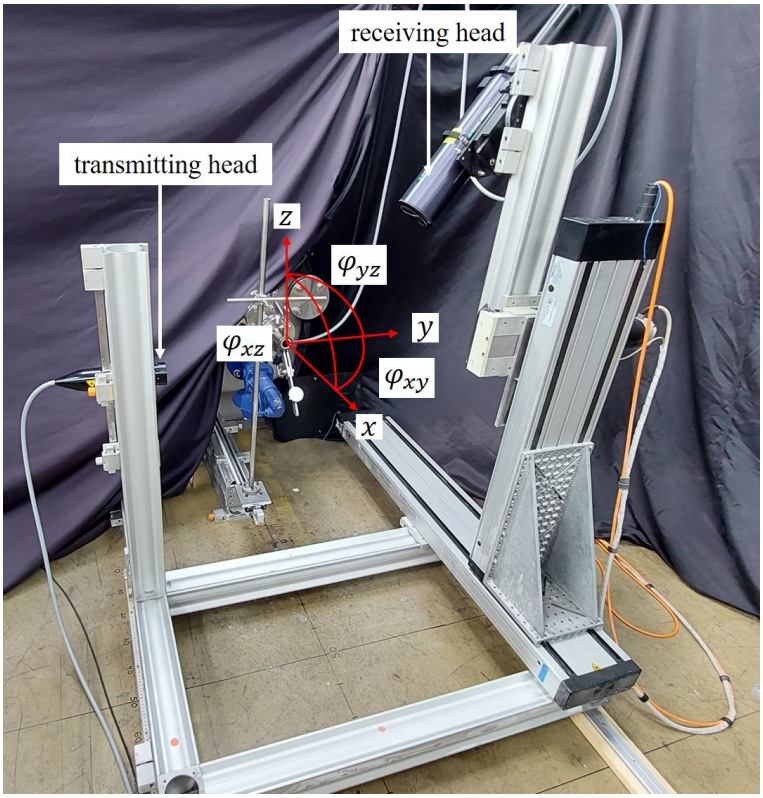

Figure 3.7.: Definition of the coordinate system used to measure the velocity field of the transient gas jets. The transmitting head and the receiving head are arranged in forward scattering mode to maximise the scattered light intensity. The receiving head is mounted on a three-axis traverse for optimum adjustment. Modified from PPA1.

A manual adjustment is almost impossible because the tightening of the adjustment screws alone had a great effect on the quality of the receiver's signal. Therefore, the receiving head is bolted to a three-axis traverse system. In x- and z-directions a traverse *LES 6* (isel Germany) and in y-direction a traverse *86.8.18 M* (Zebotronics Schrittmotoren GmbH) is used. These are connected to a controller *IMC-P1-4* (isel Germany), which is controlled via a computer with the *BSA Flow Software v6.01* (Dantec Dynamics). This makes it possible to control the three spatial directions with an accuracy of 10 µm. To avoid a completely new adjustment for each position, the transmitter and receiver head are interconnected in x-direction by a frame made of torsion-resistant 95x95 mm aluminium profiles (Spindler and Hoyer). This frame was in turn bolted to four linear runners *LFV 6-48* (isel Germany), which run on linear guide rails *LSV 6-48* (isel Germany) with a length of 2998 mm. The linear runners are adjustable without play due to eccentric rollers. Overall, when setting up the rails, it is essential that they run parallel to the jet axis. To ensure this, the alignment was carried out with a *GCL 2-15* (Bosch Professional) cross-line laser with automatic levelling. The two angles are set to $\varphi_{xy} = \varphi_{xz} = 0° \pm 0.02°$. The angle φ_{yz} between the emitting and receiving heads depends on the refractive index, the polarisation and the desired refraction mechanism. Using a calculation tool (Dantec Dynamics), the angle was set at φ_{yz} = 56°. The angle is selected depending on the relative refractive index of the particles and the type of polarisation so that one light scattering mechanism dominates (Albrecht et al., 2003). The dominant scatter order for the present PDA set up in forward scatter mode is chosen to first-order refraction. Therefore, the confidence of linearity to determine the particle diameter is 97.9 %.

The signal from the *112 mm Fiber PDA* receiver head is evaluated with a three channel *BSA P600-1D* (Dantec Dynamics) burst spectrum analyser. The system is able to process velocities of up to 433 m/s and a data rate of up to 200 kHz. The particle size is determined based on three sensors that measure two phase differences $\Delta\phi_{gh}$. The particles are assumed to hava a spherical shape because the particle size is only determined in one dimension. This assumption seems suitable given that as the particles are droplets of a few µm in size and are unlikely to be deformed by the surrounding gas flow if they have no relative velocity (cf. Table 5.2). The measured values are assigned a time stamp with a resolution of 1 µs. A black laser-protection curtain was hung to separate the control area from the measuring area, so that no person has to be in the hazardous area during the measurements. The laser-protection curtain is so heavy that it practically does not move during the discharge experiment. The arrangement of the vessel and the PDA measurement equipment is shown in Figure 3.8. For a better overview, the laser-protection curtain separating the measuring area and the control area shown in Figure 3.7 was removed for the photo. The left-hand side of the picture shows the pressure vessel with all the pressure and temperature sensors connected to it and the computers for data recording. The PDA system can be seen on the traverse system on the right-hand side of the picture, which in turn can be moved on linear axes.

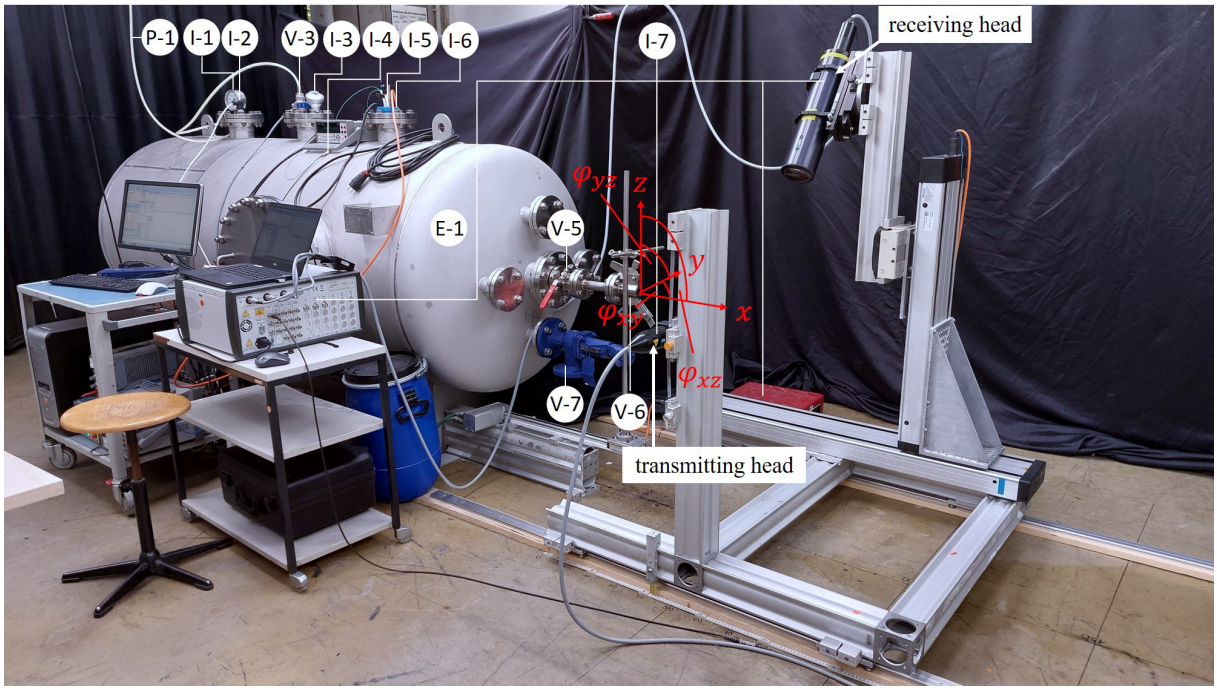

Figure 3.8.: Experimental setup to measure transient vessel outflows and form a horizontal gas jet. The PDA system is mounted on linear rails to measure different axial positions without adjustment. Modified from PPA1.

3.3. Numerical principles

The general workflow of numerical simulations is shown in Figure 3.9. The physical principles and numerical methods must be clarified in advance and all required material data must be determined. Then, the geometry in which the computational mesh is generated is defined. After that, the boundary and initial conditions are defined and the numerical simulations are performed. In the subsequent graphical evaluation, loops are run through in which an optimisation of the geometry, the mesh and the solver is worked out. For the purpose of clarity, a detailed presentation of the individual iteration steps of the workflow is not provided in the simulation chapters that follow.

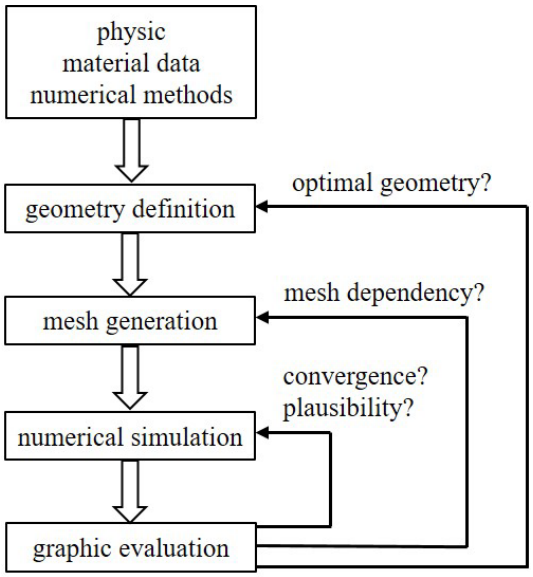

Figure 3.9.: Scheme of the workflow of a numerical calculation according to Oertel and Laurien (1995).

In the following sections, the physics are presented in the form of the governing conservation and state equations. Furthermore, the general mesh requirements are described and the principle of a Richardson extrapolation for the validation of a mesh independence is explained. The specific geometries, computational meshes, boundary and initial conditions are discussed in the simulation chapters 4 and 6.

3.3.1. Governing equations

The conservation equations of mass, momentum and energy are used for the basic description of the free jets, as well as the equations of state for the coupling of the state variables. Based on these equations, solution algorithms for numerical calculations are described. In this work, the CFD simulations are performed with the software Ansys CFX 2021 R2.
The conservation of mass is described by the continuity equation

$$\frac{\partial \varrho}{\partial t} + \frac{\partial}{\partial x_j}\left(\varrho u_j\right) = 0. \tag{3.5}$$

Here, ϱ is the density of the fluid, t is the time, x_j is the j-component of the spatial vector $\vec{x} = (x, y, z)$ and u_j is the j-component of the velocity vector $\vec{u} = (u, v, w)$. Thus, the first summand represents the accumulation of mass and the further summands represent the spatial change of the mass flux.

The conservation of momentum for flows is described by the Navier–Stokes equation

$$\frac{\partial}{\partial t}(\varrho\, u_i) + \frac{\partial}{\partial x_j}\left(\varrho\, u_i\, u_j\right) = -\frac{\partial p}{\partial x_i} + \frac{\partial \tau_{ij}}{\partial x_j} + S_{M,i}. \tag{3.6}$$

Here, p is the pressure and τ_{ij} is the shear stress tensor. On the left-hand side of the Navier–Stokes equation (3.6), the inertia terms are listed in the form of the local and convective volume-based acceleration. On the right-hand side of equation (3.6) are the mass-related surface and volume forces. The surface forces include pressure and friction forces. The volume forces, such as gravity, are summarised in the source/sink term $S_{M,i}$.

The shear stress tensor

$$\tau_{ij} = \mu\left(\frac{\partial u_i}{\partial x_j} + \frac{\partial u_j}{\partial x_i}\right) - \frac{2}{3}\,\mu\,\frac{\partial u_k}{\partial x_k}\,\delta_{ij} \tag{3.7}$$

describes the friction of the fluid. Here, μ is the dynamic viscosity and δ_{ij} is the Kronecker delta. The second term of the shear stress tensor in equation (3.7) describes the volume viscosity according to Stokes (2009), which (to date) has not been universally proven (Wendt, 2009).

The conservation of energy is described by

$$\frac{\partial}{\partial t}(\varrho h_{\mathrm{tot}}) - \frac{\partial p}{\partial t} + \frac{\partial}{\partial x_j}\left(\varrho\, u_j\, h_{\mathrm{tot}}\right) = \frac{\partial q_j}{\partial x_j} + \frac{\partial}{\partial x_j}\left(u_i\, \tau_{ij}\right) + S_E \tag{3.8}$$

with the specific total enthalpy h_{tot}

$$h_{\mathrm{tot}} = h(T) + \frac{u_i\, u_i}{2}. \tag{3.9}$$

Here, $h(T)$ is the temperature dependend enthalpy without kinetic energy. On the left-hand side of the energy conservation equation are the accumulation term and the convective heat fluxes. On the right-hand side the term $\partial q_j/\partial x_j$ is for diffusive energy transport in the form of heat conduction and is described according to Fourier's law

$$q_j = \lambda\frac{\partial T}{\partial x_j}. \tag{3.10}$$

Here, λ is the thermal conductivity and T is temperature. The term $\partial(u_i\tau_{ij})/\partial x_j$ in equation (3.8) represents the work of viscous stresses dissipated into heat due to shearing of the fluid and is called viscous dissipation. Energy sources and sinks are summarised in the term S_E. (Schlichting and Gersten, 2006)
To close the system of equations (3.5), (3.6) and (3.8), the dependencies of the state variables such as the density $\varrho(p,T)$ must be described as a function of pressure and temperature. Assuming a calorically ideal gas, the thermal equation of state of ideal gases

$$\varrho = \frac{pM}{RT} \tag{3.11}$$

is used according to Rist (1996). Here, R is the ideal gas constant and M is the mean molar mass. To describe the temperature dependent enthalpy $h(T)$, the caloric equation of state is used

$$dh = c_p(T)dT. \tag{3.12}$$

Here, $c_p(T)$ is the specific heat capacity at constant pressure p. Since multicomponent systems are investigated, an equation for the transport of the mass fraction Y_S of species S is needed (Gerold, 2015). This reads as

$$\frac{\partial}{\partial t}(\varrho Y_S) + \frac{\partial}{\partial x_i}(\varrho u_i Y_S) = \frac{\partial j_{S,i}}{\partial x_i}. \tag{3.13}$$

Here, $j_{S,i}$ is the diffusion flux per unit area of species S in the spatial direction $i = x, y, z$; which is described by the law of Fick (1855)

$$j_{S,i} = -\varrho D_S \frac{\partial Y_S}{\partial x_i}, \tag{3.14}$$

where D_S is the diffusion coefficient of species S.

Theoretically, these equations with the corresponding models for the viscous stress tensor and the heat flux density as well as the thermodynamic state equations are sufficient to describe almost all fluid mechanical problems. However, in turbulent flows the local and temporal fluctuations are in such a wide range of scales that it is impossible to solve practical fluid mechanical problems by direct numerical simulation with today's computing power (Spalart and Venkatakrishnan, 2016).

To solve this problem, all flow variables $\phi(\vec{x}, t)$ are divided into time averages $\bar{\phi}(\vec{x})$ and turbulent fluctuations $\phi'(\vec{x}, t)$ according to Reynolds (1895)

$$\phi(\vec{x}, t) = \bar{\phi}(\vec{x}) + \phi'(\vec{x}, t), \tag{3.15}$$

with

$$\bar{\phi} = \frac{1}{\Delta t}\int_t^{t+\Delta t} \phi \, dt. \tag{3.16}$$

Therefore, the exact equations are time averaged. Here, Δt is a time scale, which is large compared to the turbulent fluctuation time scale but small relative to the physical time scale of the fluid mechanical problem. Using the time-averaging rules of Wilcox (1988), the following conservation equations are obtained.

$$\frac{\partial \varrho}{\partial t} + \frac{\partial}{\partial x_j}\left(\varrho \bar{u}_j\right) = 0, \tag{3.17}$$

$$\frac{\partial}{\partial t}(\varrho\, \bar{u}_i\,) + \frac{\partial}{\partial x_j}\left(\varrho\, \bar{u}_i\, \bar{u}_j\right) = -\frac{\partial \bar{p}}{\partial x_i} + \frac{\partial}{\partial x_j}\left(\bar{\tau}_{ij} - \varrho\overline{u_i' u_j'}\right) + S_{M,i}, \tag{3.18}$$

with

$$\bar{\tau}_{ij} = \mu\left(\frac{\partial \bar{u}_i}{\partial x_j} + \frac{\partial \bar{u}_j}{\partial x_i}\right) - \frac{2}{3}\,\mu\,\frac{\partial \bar{u}_k}{\partial x_k}\,\delta_{ij}; \tag{3.19}$$

$$\frac{\partial \varrho \bar{h}_{\mathrm{tot}}}{\partial t} - \frac{\partial \bar{p}}{\partial t} + \frac{\partial}{\partial x_j}\left(\varrho \bar{u}_j\,\bar{h}_{\mathrm{tot}}\right) = \frac{\partial}{\partial x_j}\left(\lambda \frac{\partial\,\bar{T}}{\partial x_j} - \varrho\overline{u_j' h'}\right) + \frac{\partial}{\partial x_j}\left(\bar{u}_i\left(\bar{\tau}_{ij} - \varrho\,\overline{u_i' u_j'}\right)\right) + S_E, \tag{3.20}$$

with

$$\bar{h}_{\mathrm{tot}} = \bar{h} + \frac{1}{2}\bar{u}_i\,\bar{u}_i + \underbrace{\frac{1}{2}\overline{u_i' u_i'}}_{k}. \tag{3.21}$$

Here, the term $\varrho\,\overline{u_i' u_j'}$ is the Reynolds stress and $\frac{1}{2}\overline{u_i' u_i'}$ is the turbulent kinetic energy k. A closure problem of the differential equations system arises because it is unterdetermined due to the unknown Reynolds stresses $\varrho\,\overline{u_i' u_j}'$ and no unique solution exists. To solve the problem, the Reynolds stresses $\varrho\,\overline{u_i' u_j}'$ are approximated through models.

According to the hypothesis of Boussinesq (1877), turbulence can be described in terms of small vortices that are constantly forming and dissipating. Accordingly, turbulent fluctuation causes an increase in viscosity. The so-called eddy viscosity μ_t has to be added to the molecular viscosity μ, i.e.,

$$\mu_{\mathrm{eff}} = \mu + \mu_t, \tag{3.22}$$

and taken into account in the conservation equations in the form of the effective viscosity μ_{eff}. This model approximation is called eddy-viscosity model. According to this approximation, the Reynolds stresses are proportional to the mean velocity gradients because there is an analogy to the friction law of Stokes for laminar flows (Oertel and Laurien, 1995), hence

$$-\varrho\,\overline{u_i' u_j}' = \mu_t\left(\frac{\partial \bar{u}_i}{\partial x_j} + \frac{\partial \bar{u}_j}{\partial x_i}\right) - \frac{2}{3}\delta_{ij}\left(\varrho k + \mu_t \frac{\partial \bar{u}_k}{\partial x_k}\right). \tag{3.23}$$

The eddy viscosity μ_t must also be approximated by models, which will be presented in the next sections. Analogous to the eddy-viscosity hypothesis, there is the eddy-diffusion hypothesis, which states that the time-averaged fluxes of a scalar are linearly related to the mean gradient of the scalar, i.e.;

$$-\varrho\overline{u_i' \phi'} = \Gamma_t \frac{\partial \overline{\phi}}{\partial x_i}. \tag{3.24}$$

Here, Γ_t is the eddy diffusion

$$\Gamma_t = \frac{\mu_t}{Pr_t}, \tag{3.25}$$

which is described with the turbulent viscosity μ_t and the turbulent Prandtl number Pr_t. Furthermore, a modified pressure

$$\overline{p}_{\mathrm{mod}} = \overline{p} + \frac{2}{3}\varrho k \tag{3.26}$$

is implemented in ANSYS CFX. Rigorously, the right-hand side of equation (3.26) also contain the term $+2/3\ \mu_{\text{eff}}\,\partial\bar{u}_k/\partial x_k$ and it is correct in this form only for incompressible fluids. The additional term is neglected in ANSYS CFX and is not implemented. Considered strictly, the eddy-viscosity model is only valid for isotropic turbulence. For flows where anisotropic turbulence is present, second-order closure would have to be performed, according to Oertel and Laurien (1995). These more complex models, which take into account the anisotropy of the turbulence, include (for example) the Reynolds stress models. However, the model parameters required for this are still the subject of current research and a much greater computational effort is required. The two turbulence models used are presented in the following sections.

3.3.1.1. *k-ε* turbulence model

The first turbulence model used in this work is the standard k-ε turbulence model according to Jones and Launder (1972). It is validated for the simulation of free shear layers and is the established model for such problems. According to Launder and Spalding (1974), it is based on the following approach

$$\mu_t = \varrho\, C_\mu \frac{k^2}{\varepsilon}. \tag{3.27}$$

Here, ε is the isotropic dissipation rate of the turbulent kinetic energy k and C_μ is a model constant. This leads to the following equation for the conservation of momentum

$$\frac{\partial \varrho \bar{u}_i}{\partial t} + \frac{\partial}{\partial x_j}\left(\varrho \bar{u}_i\, \bar{u}_j\right) = -\frac{\partial \bar{p}_{\text{mod}}}{\partial x_i} + \frac{\partial}{\partial x_j}\left((\mu + \mu_t)\left(\frac{\partial \bar{u}_i}{\partial x_j} + \frac{\partial \bar{u}_j}{\partial x_i}\right)\right) + S_{M,i}. \tag{3.28}$$

The following equation applies to the conservation of energy

$$\frac{\partial \varrho \bar{h}_{\text{tot}}}{\partial t} - \frac{\partial \bar{p}}{\partial t} + \frac{\partial}{\partial x_j}\left(\varrho \bar{u}_j\, \bar{h}_{\text{tot}}\right) = \frac{\partial}{\partial x_j}\left(\lambda \frac{\partial\, \bar{T}}{\partial x_j} - \frac{\mu_t}{Pr_t}\frac{\partial \bar{h}}{\partial x_j}\right) + \frac{\partial}{\partial x_j}\left(\bar{u}_i\left(\bar{\tau}_{ij} - \varrho\, \overline{u_i' u_j'}\right)\right). \tag{3.29}$$

To close the differential equation system, two further equations are introduced according to Launder and Spalding (1974). On the one hand, the equation for the transport of turbulent kinetic energy k

$$\frac{\partial \varrho k}{\partial t} + \frac{\partial}{\partial x_j}\left(\varrho \bar{u}_j k\right) = \frac{\partial}{\partial x_j}\left(\left(\mu + \frac{\mu_t}{\sigma_k}\right)\frac{\partial k}{\partial x_j}\right) + P_k - \varrho\varepsilon + P_{kb}, \tag{3.30}$$

and on the other hand the equation for the transport of the isotropic dissipation rate ε

$$\frac{\partial \varrho \varepsilon}{\partial t} + \frac{\partial}{\partial x_j}\left(\varrho \bar{u}_j\, \varepsilon\right) = \frac{\partial}{\partial x_j}\left(\left(\mu + \frac{\mu_t}{\sigma_\varepsilon}\right)\frac{\partial \varepsilon}{\partial x_j}\right) + \frac{\varepsilon}{k}\left(C_{\varepsilon 1} P_k - C_{\varepsilon 2}\varrho\varepsilon + C_{\varepsilon 1} P_{\varepsilon b}\right). \tag{3.31}$$

Here, P_k is the turbulence production due to viscous forces, which is modelled as

$$P_k = \mu_t\left(\frac{\partial \bar{u}_i}{\partial x_j} + \frac{\partial \bar{u}_j}{\partial x_i}\right)\frac{\partial \bar{u}_i}{\partial x_j} - \frac{2}{3}\frac{\partial \bar{u}_k}{\partial x_k}\left(3\mu_t \frac{\partial \bar{u}_k}{\partial x_k} + \varrho k\right). \tag{3.32}$$

The term P_{kb} is the turbulence production

$$P_{kb} = -\frac{\mu_t}{\varrho} g_i \frac{\partial \varrho}{\partial x_i}, \tag{3.33}$$

where i is the component of the gravitational acceleration vector and $P_{\varepsilon b}$ is the turbulence dissipation

$$P_{\varepsilon b} = \max(0, P_{kb}) \tag{3.34}$$

due to buoyancy. The constants C_μ = 0.09, σ_k = 1, σ_ε = 1.3, $C_{\varepsilon 1}$ = 1.44 and $C_{\varepsilon 2}$ = 1.92 have been calibrated in the literature by comparing experimental and numerical studies and there are several proposed sets. Here, the constants of Launder and Spalding (1974) are used because they are carefully studied and capture most problems well. The constants were adapted for the calculation of free turbulent flows, such as plane free jets and shear flows. Further details on the equations used can be found in ANSYS (2019).

3.3.1.2. Generalised k-ω (GEKO) turbulence model

The second turbulence model is the generalised k-ω (GEKO) turbulence model. The GEKO model is a relatively new two-equation turbulence model by Menter et al. (2019), which is based on the k-ω model according to Wilcox (1998). However, it can be adapted to a wide variety of fluid mechanical problems. The advantage of this is that problems are not adapted by using different turbulence models, as is usually the case, but rather by using different parameter sets for one turbulence model. Of course, the parameters of the k-ε turbulence model can also be adjusted, but a slight change of one parameter may have a direct and major impact on the overall result of the model, so this is generally not recommended.

In the following, the governing equations of the GEKO model and the six free parameters are presented. The equations for the conservation of mass (3.17), momentum (3.28) and energy (3.29) of the GEKO model do not differ from the k-ε turbulence model. The difference is the calculation of turbulent viscosity by

$$\mu_t = \varrho \frac{k}{\max(\omega, S/C_{\text{Realize}})}, \tag{3.35}$$

which ensures that the Reynolds stresses do not become negative and that the eddy viscosity μ_t cannot grow arbitrarily in the case where the turbulent frequency tends to zero, i.e., $\omega \to 0$. Here, S is the strain

$$S = \sqrt{2\, S_{ij} S_{ij}}, \tag{3.36}$$

with

$$S_{ij} = \frac{1}{2}\left(\frac{\partial \bar{u}_i}{\partial x_j} + \frac{\partial \bar{u}_j}{\partial x_j}\right). \tag{3.37}$$

Furthermore, $C_{\mathrm{Realize}} = 0.577$ is the realisation coefficient, which is an additional limit of turbulence production beside the production limiter P_k, which reads as

$$P_k = -\bar{\tau}_{ij}\frac{\partial \bar{u}_i}{\partial x_j}. \tag{3.38}$$

The shear stress tensor $\bar{\tau}_{ij}$ of the GEKO model has a third non-linear stress-strain term to account for secondary flows in corners Mani et al. (2013), i.e.

$$\begin{aligned}\bar{\tau}_{ij} = \mu_t\left(\frac{\partial \bar{u}_i}{\partial x_j}+\frac{\partial \bar{u}_j}{\partial x_i}\right) - \frac{2}{3}\,\varrho k\,\delta_{ij} \\ - C_{\mathrm{CORNER}}\frac{1.2\,\mu_t}{\max\left(0.3\,\omega, \sqrt{0.5(S^2+\Omega^2)}\right)}\left(S_{ik}\Omega_{kj}-\Omega_{ik}S_{kj}\right).\end{aligned} \tag{3.39}$$

Furthermore, Ω is the vorticity given by

$$\Omega = \sqrt{2\Omega_{ij}\Omega_{ij}}, \tag{3.40}$$

with

$$\Omega_{ij} = \frac{1}{2}\left(\frac{\partial \bar{u}_i}{\partial x_j}-\frac{\partial \bar{u}_j}{\partial x_i}\right). \tag{3.41}$$

The transport equation for the turbulent kinetic energy k in the GEKO model is

$$\frac{\partial(\varrho k)}{\partial t}+\frac{\partial(\varrho \bar{u}_j k)}{\partial x_j} = P_k - C_\mu \varrho k\omega + \frac{\partial}{\partial x_j}\left[\left(\mu+\frac{\mu_t}{\sigma_k}\right)\frac{\partial k}{\partial x_j}\right]. \tag{3.42}$$

Here, $C_\mu = 0.09$ and $\sigma_k = 1.0$ are the common k-ε model constants according to Launder and Spalding (1974) and ω is the turbulent frequency, which is captured in a separate transport equation, namely

$$\frac{\partial(\varrho\omega)}{\partial t}+\frac{\partial(\varrho \bar{u}_j \omega)}{\partial x_j} = C_{\omega1}F_1\frac{\omega}{k}P_k - C_{\omega2}F_2\varrho\omega^2 + \varrho F_3 CD + \frac{\partial}{\partial x_j}\left[\left(\mu+\frac{\mu_t}{\sigma_\omega}\right)\frac{\partial \omega}{\partial x_j}\right]. \tag{3.43}$$

Here, $C_{\omega1} = 1.7$ and $C_{\omega2} = 1.4$ are auxiliary model coefficients and CD is defined as

$$CD = \frac{2}{\sigma_\omega}\frac{1}{\omega}\frac{\partial k}{\partial x_j}\frac{\partial \omega}{\partial x_j}, \tag{3.44}$$

with the k-ω turbulence model constant $\sigma_\omega = 2$. Furthermore, F_1, F_2 and F_3 are functions, which are tuned by six parameters $\{C_{\mathrm{SEP}}, C_{\mathrm{NW}}, C_{\mathrm{MIX}}, C_{\mathrm{JET}}, C_{\mathrm{CORNER}}, C_{\mathrm{CURV}}\}$ in such a way that the physics in the various fluid mechanical regions are correctly captured. The details of these functions are not published. Since these six parameters are mainly used to capture boundary layer and free shear flows, it makes the GEKO model interesting for free jets. The main parameter to influence the spreading behaviour of free shear flows is the separation coefficient C_{SEP}. An increase of the separation parameter C_{SEP} reduces the eddy viscosity and spreading rate $K_{2,u}$. Based on some test simulations and comparison with experimental data in chapter 4, the separation coefficient is set to $C_{\mathrm{SEP}} = 2.2$. The near wall parameter $C_{\mathrm{NW}} = 0.5$ influences the velocity profile close to the wall and, therefore, mainly influences the heat flux

at the wall. The mixing parameter $C_{\mathrm{MIX}} = 0.35\mathrm{sign}(C_{\mathrm{SEP}} - 1)\sqrt{|C_{\mathrm{SEP}} - 1|}$ only influences free shear flows and an increase of the mixing parameter C_{MIX} increases the eddy viscosity and spreading rate $K_{2,u}$. Here, the default formula was not used and a mixing parameter $C_{\mathrm{MIX}} = 0.3$ is set. The jet parameter $C_{JET} = 0.9$ adjusts the spreading rate $K_{2,u}$ of jet flows, while retaining the spreading of the mixing layer. The jet parameter is intended to prevent an overestimation of the spreading rate and an underestimation of the decay constant, which is one of the main problems of the k-ε model (Pope, 1978). The corner parameter C_{CORNER} is used to capture secondary flows in corners, and is therefore not relevant for the present problem of a free jet. The curvature correction parameter C_{CURV} is an already existing model for all eddy-viscosity models that suppresses or enhances turbulence based on the flow curvature (Smirnov and Menter, 2009). (Menter et al., 2019)

3.3.2. Mesh requirements

In computational fluid mechanics, the balance equations given in the previous sections are solved at discrete points. The entirety of these discretisation points of a numerical method is called a numerical mesh or computational grid (Oertel and Laurien, 1995). Figure 3.10 is used as an example to explain how the control volumes are generated. A control volume (grey area) is generated around each mesh node using the “median dual”, which is defined by lines joining the element centres and the centres of the edges surrounding the node (ANSYS, 2019).

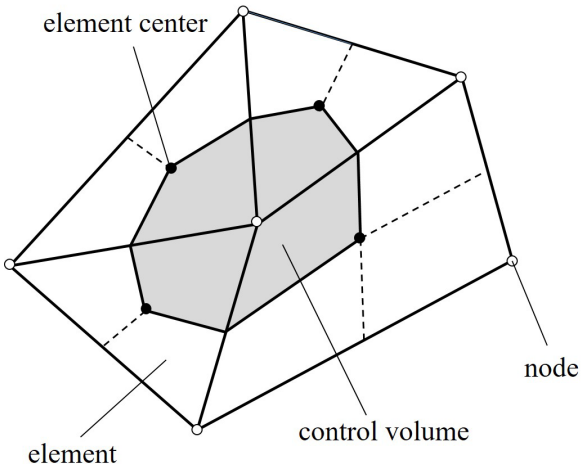

Figure 3.10.: Control volume definition according to ANSYS (2019).

According to Paschedag (2006), the solution of a simulation is considerably influenced by the quality of the mesh. A distinction is made between geometric, physical and numerical mesh requirements. In geometric requirements the domain should be meshed, if possible, in such a way that each cell belongs completely to the domain and the cell edges coincide with the edges of the domain (Paschedag, 2006).

One of the physical requirements is that the mesh density is oriented to the solution of the partial differential equations. This means that a denser mesh is needed in areas of steep gradients. Furthermore, the main flow direction should flow orthogonally through the cells to minimise numerical diffusion. However, this requires that the approximate behaviour of the simulation result is known. For this purpose, a so-called mesh adaptation simulation with an unstructured mesh was also carried out. The simulation runs through several iteration loops, in which the mesh was refined independently in areas of higher shear gradients. The mesh created by this method was a reference point for the structured meshes that will be used later.

Numerical requirements include low skewness, orthogonality, an aspect ratio close to one and a moderate growth rate of the cells (Paschedag, 2006). It is not always possible to fulfil all criteria equally. In particular, the point of an aspect ratio close to one is only fulfilled to a limited extend to reduce the number of cells and the computing power.

In general, computational grids are divided into structured and unstructured meshes, as shown in Figure 3.11. Unstructured meshes have the advantage that they can even be automatically generated for complex 3D geometries and that there is no preferred direction in which the numerical error becomes minimal (Oertel and Laurien, 1995). Since there are no well-defined neighbourhood relationships of nodes in an unstructured grid, the relationship between nodes and elements is established by an allocation matrix (Oertel and Laurien, 1995). This increases the computational effort and memory requirements by a factor of 3 to 4 compared to a structured grid (ANSYS, 2019). For this reason, a structured computational grid is aimed at in the following.

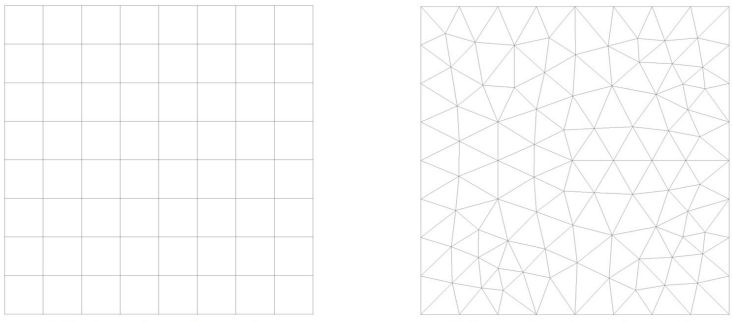

(a) structured mesh (b) unstructured mesh

Figure 3.11.: Example of a structured mesh (a) and an unstructured mesh (b).

3.3.3. Richardson extrapolation

The systems of equations presented in the section 3.3.1.1 and 3.3.1.2 are discretised using an element-based finite volume method. The equations are approximated by means of a Taylor series. In Ansys

CFX, the Taylor series is usually terminated after the second element, which corresponds to a second-order accuracy. This is a compromise between accuracy, robustness and computing power. The equations discretised in space and time are approximations to the differential equations describing the problem (ANSYS, 2019). Therefore, the discretisation generates an error, which can be estimated with a mesh-independence study. The discretised solution Φ_H, where the index H is the mesh spacing of the reference mesh, deviates from the exact solution Φ by the discretisation error ϵ_H, i.e.,

$$\Phi = \Phi_H + \epsilon_H. \tag{3.45}$$

To determine the discretisation error, Richardson (1911) has developed a method where the exact solution of the differential equations is extrapolated. The extrapolation is based on mesh resolutions of varying fineness. This proves the convergence of the solution and the independence towards a refinement of the mesh. The exact solution Φ, i.e.

$$\Phi \approx \Phi_H + \frac{(\Phi_H - \Phi_{2H})^2}{2\Phi_{2H} - \Phi_{4H} - \Phi_H}, \tag{3.46}$$

is directly approximated from the solution of the single Φ_H, double Φ_{2H} and quadruple Φ_{4H} mesh distance. (Ferziger et al., 2020)

However, such an extrapolation of the exact solution Φ is only possible if the solutions with different mesh resolutions are strictly-monotonic in relation to each other. The deviations of the solutions with different mesh resolution from the approximated exact solution Φ is considered as a quality criterion of convergence. Therefore, this procedure is carried out as a validation step in the subsequent simulations.

4. Similarity solution for subcritical pressure relief

Based on the Bernoulli's equation, a fast and accurate model for the prediction of transient gas outflow from vessels is to be derived in this chapter. The system is considered adiabatic, isentropic, and subcritical and the gas is considered ideal and compressible. Two cases are considered. In the first case, a thin-wall vessel is considered in which frictional pressure losses are negligible. In the second case, a thick-wall vessel is considered in which frictional pressure losses inside the outlet must be taken into account. For the first case, a dimensionless number is to be identified based on the Π-theorem according to Buckingham (1914), which is to be used to describe any subcritical, adiabatic discharge. The model and the dimensionless number will be validated by numerical simulations and experiments.

4.1. Introduction

Although the efflux of a compressible gas from a vessel is a basic problem, the derivation of a solution is quite complex because there is no general analytical solution, and is therefore error-prone (Batchelor, 2010). Motivated by the acute case of safety problems at a nuclear power plant, Schmidt (1965) derived a model for calculating supercritical and subcritical vessel discharges. The model by Schmidt (1965) is fundamentally based on the energy conservation equation for adiabatic gas systems without work and friction. The energy conservation was combined with equations of state of ideal gases, isentropic equations, and a mass balance. A closed-form solution for a heat capacity ratio of $\kappa = 1.4$ was determined. The subcritical solution is only for the case that the discharge just starts at the critical pressure ratio. Furthermore, pressure losses are not taken into account.

Rist (1996) derived a model using a similar approach to Schmidt (1965). The assumptions of an adiabatic vessel wall and ideally isentropic system are also made in the model according to Rist (1996). In contrast to the model according to Schmidt (1965), pressure losses can be taken into account by a loss coefficient. Therefore, it should be closer to the real case scenario. If pressure losses are neglected, the model of Rist (1996) returns the same discharge durations as the model of Schmidt (1965). The model of Rist (1996) is able to capture arbitrary subcritical pressure ratios and is not limited to the critical pressure ratio as initial condition. Closed-form solutions for the heat capacity ratios $\kappa = 1.33$ and $\kappa = 1.4$ are available.

[PA1] Parts of this chapter are based on the article: A fast method to predict the transient, subcritical gas discharge from a pressure vessel by M.-D. Fischer and K. Boettcher; it was first published in *Chem. Eng. Sci*. 2022

[PA2] Parts of this chapter are based on the article: Similarity solution of subcritical pressure discharges from vessel for arbitrary gases by M.-D. Fischer, S. Baier and K. Boettcher; it was first published in *Chem. Eng. Sci*. 2023

John and Keith (2006) derived a model using a similar approach to Schmidt (1965) and Rist (1996). An adiabatic, isentropic system with an ideal gas is also assumed. As with the work of Schmidt (1965), no pressure losses are taken into account, but it is not limited to the critical pressure ratio as an initial condition for the discharge. A closed-form solution for a heat capacity ratio of κ = 1.4 was determined. In the case where the critical pressure ratio is an initial condition, the models of John and Keith (2006) and Schmidt (1965) give the same results.

Kümmel (2007) modified the model of Schmidt (1965) and Rist (1996) and was able to calculate closed-form solutions for the heat capacity ratios κ = 1.25; 1.33; 1.4; 1.5. The model according to Kümmel (2007) can also calculate subcritical discharges that do not have the critical pressure ratio as an initial condition. For this, however, the initial condition must be calculated back to a fictitious critical condition. The time from the critical condition to the actual initial condition must then be subtracted from the total discharge duration. These models had only solutions for very specific heat capacity ratios and need a longer training period to understand them. Since these models are quite complex and are not generally applicable, they were not very practical for quick estimates. Up to this point, no attempts had been made to find a self-similar solution that would suggest a more straightforward calculation.

4.2. Model and dimensionless number

The Bernoulli equation is one of the basic tools for describing one-dimensional, frictionless flows (Zierep, 2018). It can also be extended to take pressure losses due to friction and inertia into account, thus enabling the calculation of technical pipe flows. The discharge from a pressure vessel is regarded as a discontinuous narrowing and widening of a pipe flow. These flows through orifices have already been discussed extensively in the literature. The focus was often on stationary flows and the characterisation of the flow conditions in and behind the orifice (Liepmann, 1961; Renn and Hsiao, 2004; Shah et al., 2012; Yan and Thorpe, 1990). However, a transient discharge from a vessel, where the focus is on the time-dependent flow variables in front of the orifice, has rarely been investigated. In general, the compressible Bernoulli equation from a point 1 inside the vessel (cf. Figure 4.1), via the point 2 at the vessel outlet, to an infinite point ∞ in the non-affected ambient atmosphere is given by

$$\frac{1}{2}c_1^2 + gz_1 = \frac{1}{2}c_\infty^2 + gz_\infty + \int_{p_1}^{p_\infty}\frac{1}{\varrho}dp + \int_{s_1}^{s_\infty}\frac{\partial c}{\partial t}ds + \frac{\Delta p_{\mathrm{loss}}}{\varrho_2}, \tag{4.1}$$

where c_1 is the average absolute velocity in the vessel, g is the gravitational acceleration, $z_1 = z_\infty$ is the height, $c_\infty = 0$ is the average velocity at an infinite point, p_1 is the pressure in the vessel, p_∞ is the ambient pressure, ϱ is the density of the gas, ds is the differential path element of the streamline and Δp_{loss} are additional pressure losses. According to Rist (1996) the acceleration of the gas inside the

vessel is negligibly small and quasi-stationarity can be assumed. This assumption will also be tested in the numerical simulations that follow.

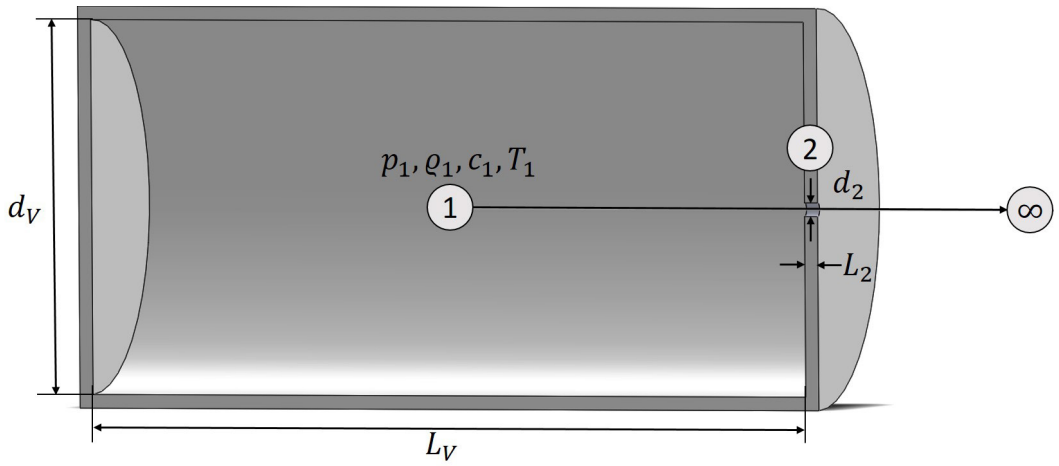

Figure 4.1.: Illustration of the streamline set-up. Modified from PA2.

The pressure loss Δp_{loss} is composed of inertial pressure losses $\Delta p_{\text{inertia}}$ and frictional pressure losses $\Delta p_{\text{friction}}$

$$\Delta p_{\text{loss}} = \Delta p_{\text{inertia}} + \Delta p_{\text{friction}}. \tag{4.2}$$

The inertial pressure losses $\Delta p_{\text{inertia}}$

$$\Delta p_{\text{inertia}} = \sum \frac{\varrho_2}{2} c_2^2 \zeta, \tag{4.3}$$

depend on the cross-sectional average velocity at the vessel outlet c_2, the density ϱ_2 at the outlet and the pressure loss coefficient ζ, which is related to the flow geometry.

The frictional pressure losses $\Delta p_{\text{friction}}$

$$\Delta p_{\text{friction}} = \frac{\varrho_2}{2} \frac{L_2}{d_2} \lambda_f, \tag{4.4}$$

depend on the drag coefficient λ_f, the density ϱ_2 and the length-to-diameter ratio of the outlet L_2/d_2. Two cases are considered here. The first case is the more common case of thin-wall vessels, where the frictional pressure inside the outlet loss is considerably smaller than the inertial pressure loss due to the cross-sectional changes at the outlet. The frictional pressure loss is neglected in this case $\Delta p_{\text{friction}} = 0$. The inertial pressure loss in a discontinuous narrowing of the cross-sectional area arises by a constriction of the streamlines after passing the narrower cross section. This effect is shown in Figure 4.2 and can be described by the so-called contraction coefficient μ_c. This is defined as the ratio of the constricted flow cross section A_2^* to the opening cross section A_2, i.e.

$$\mu_c = \frac{A_2^*}{A_2}. \tag{4.5}$$

Consequently, the values of the contraction coefficient are constrained to $\mu_c \leq 1$. Since in this case a thin-wall vessel is considered, it is assumed that the opening of the vessel behaves like a thin orifice. According to Truckenbrodt (2008), the contraction coefficient is $\mu_c \approx 0.61$ for a blended cross-sectional change where the vessel cross section A_1 is considerably larger than the opening cross section A_2. This is supported by Batchelor (2010) and Oertel (2012), who observed a contraction coefficient of $\mu_c \approx 0.6$ for a hole in a plane wall.

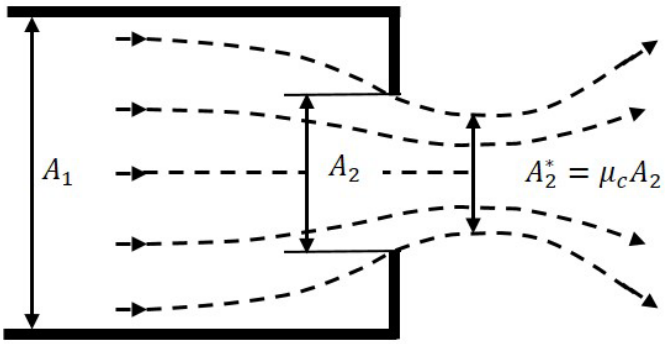

Figure 4.2.: Schematic illustration of the constriction of a flow through a hole in a plane wall according to Truckenbrodt (2008). Modified from PA2.

The sum of the pressure loss coefficients ζ is calculated using the contraction coefficient μ_c according to Truckenbrodt (2008), i.e.,

$$\sum\zeta \approx 1.5\left(\frac{1-\mu_c}{\mu_c}\right)^2 + 1. \tag{4.6}$$

The discharge into an infinite resting environment is taken into account with the term +1 at the end of the equation. Thus, the sum of the pressure loss coefficients for the first case of thin-wall vessels is $\sum\zeta$ = 1.61.

The second case is a thick-wall vessel or a vessel with a pipe outlet, as will be investigated experimentally later in section 4.5. From a length-to-diameter ratio of $L/d_2 > 5$, the frictional pressure loss accounts for about 10 % of the total pressure loss and should no longer be neglected. For this case the pressure loss coefficient is $\sum\zeta$ = 0.5+1 = 1.5 according to Idel'Chik (2008). The drag coefficient λ_f for the frictional pressure loss $\Delta p_{\text{friction}}$ is determined by the equation of Colebrook and White (1937)

$$\frac{1}{\sqrt{\lambda_f}} = -2\log\left(\frac{2.51}{\text{Re}\sqrt{\lambda_f}} + \frac{K}{3.71\,d_2}\right). \tag{4.7}$$

Here, K is the absolut roughness of the surface.

According to John and Keith (2006), the change of state during gas discharge from a pressure vessel can be approximated as ideal isentropic with no heat transfer between the vessel walls and the gas. Together with the assumption of an ideal gas, the following relationship results for an isentropic change of state

$$\frac{p}{\varrho^{\kappa}} = \text{const.}\ . \tag{4.8}$$

By using the isentropic equation (4.8) and the assumption according to Zierep (2018) that the outlet pressure is equal to the ambient pressure $p_2 = p_\infty$, the integral of the static pressure term from equation (4.1) can be solved as follows:

$$\int_{p_1}^{p_\infty} \frac{1}{\varrho} dp = -\frac{\kappa}{\kappa-1}\frac{p_1}{\varrho_1}\left(1-\left(\frac{p_\infty}{p_1}\right)^{\frac{\kappa-1}{\kappa}}\right) = -\frac{\kappa}{1-\kappa}\frac{p_\infty}{\varrho_2}\left(1-\left(\frac{p_1(t)}{p_\infty}\right)^{\frac{\kappa-1}{\kappa}}\right). \tag{4.9}$$

By substituting equations (4.3) and (4.9) into equation (4.1) and rearranging, the following correlation results for the cross-sectional average flow velocity at the vessel outlet c_2, namely

$$c_2(p_1(t)) = \sqrt{\frac{2}{\sum\zeta + \frac{L_2}{d_2}\lambda_f}\frac{\kappa}{1-\kappa}\frac{p_\infty}{\varrho_2}\left(1-\left(\frac{p_1(t)}{p_\infty}\right)^{\frac{\kappa-1}{\kappa}}\right)}\ . \tag{4.10}$$

The temporal development of the internal pressure inside the vessel p_1 is determined with a balance for the mass of the gas in the vessel, i.e., by

$$m(t) = m_0 - \int_{t_0}^{t} \dot{m}_{\text{dis}}(c_2(p_1(t)))\, dt. \tag{4.11}$$

The gas mass in the vessel $m(t)$ corresponds to the initial gas mass m_0 subtracted by the gas mass that has been discharged up to time t, which is calculated via the gas mass flow $\dot{m}_{\text{dis}}$. According to the ideal gas equation, the following results for the gas masses m_0 and m(t) :

$$m_0 = \frac{VMp_0}{RT_0}, \tag{4.12}$$

$$m(t) = \frac{VMp_1(t)}{RT_1(t)}, \tag{4.13}$$

where V is the vessel volume, M is the molar mass of the gas, p_0 is the absolute pressure at the time $t = 0$, R is the ideal gas constant and T_0 is the absolute temperature in K at the time $t = 0$. The gas mass flow

$$\dot{m}_{\text{dis}}(t) = \varrho_2 A_2 c_2\big(p_1(t)\big) = \varrho_2 \frac{\pi}{4} d_2^2 c_2\big(p_1(t)\big) \tag{4.14}$$

is determined via the gas density ϱ_2, the cross-sectional area of the vessel opening A_2 and the area averaged flow velocity at the outlet c_2. The circular cross section A_2 is determined with the outlet diameter d_2. By substituting equations (4.12), (4.13) and (4.14) into (4.11) and applying the isentropic equation (4.8) the following differential equation for the internal pressure of the vessel $p_1(t)$ is obtained:

$$\frac{dp_1}{dt} = -\sqrt{\frac{2p_\infty \varrho_2}{\sum\zeta + \frac{L_2}{d_2}\lambda_f}} \frac{RT_0 p_0^{\frac{1-\kappa}{\kappa}}}{VM} \kappa \frac{\pi}{4} d_2^2 \sqrt{\frac{\kappa}{1-\kappa}\left(p_1(t)^{\frac{2\kappa-2}{\kappa}} - p_\infty^{\frac{1-\kappa}{\kappa}} p_1(t)^{\frac{3\kappa-3}{\kappa}}\right)}. \tag{4.15}$$

This differential equation is solved numerically using the 4th-order Runge–Kutta method according to Runge (1895) and Kutta (1901). A time step size of $\Delta t = 10^{-5}$ s is used.

In addition to the model based on the Bernoulli equation, a dimensionless number for the characterisation of thin-wall vessel discharges is to be identified. The dimensionless number should, therefore, only cover the first case without frictional pressure losses, i.e., $\Delta p_{\text{friction}} = 0$. The Π-theorem according to Buckingham (1914) is used for this purpose. The first step is to collect all of the input variables that can affect the outflow. The variables of the Bernoulli model are used as the basis for the input variables. Subsequently, all influencing variables are converted into their SI base units and sorted by mass, length, time and temperature. The input variables and their corresponding SI base units are used to generate a dimension matrix. By determining the rank of the dimension matrix and the number of input variables, the number of independent dimensionless numbers can be determined. The dimensionless numbers are then determined by a coefficient comparison. The following dimensionless number has been found to be the most promising for characterising the vessel discharge

$$\Pi_1 = \frac{V^*}{V} = \frac{(p_0 - p_\infty)^{1/2} d_2^2 \, t_{\text{dis}} \, \kappa}{V \left(\frac{p_0 M}{R T_0}\right)^{1/2}}. \tag{4.16}$$

The dimensionless number Π_1 describes the ratio of a characteristic, discharged volume V^* to the total vessel volume V. The characteristic volume V^* results from the product of the cross-sectional area d_2^2, the characteristic discharge time t_{dis}, the heat capacity ratio κ and a characteristic frictionless velocity for the gas $\sqrt{\Delta p/\varrho}$.

To clarify when the model with frictional pressure losses is used and when the model without frictional pressure losses is used, two abbreviations are introduced. The general model with frictional and inertial pressure losses is called the frictional inertial loss model (FILM). The model without frictional losses and with inertial losses is called the inertial loss model (ILM). The validity of the ILM and the dimensionless number Π_1 will be proven by a comparison with numerical simulations. The FILM will be proven with experimental investigations.

4.3. CFD simulation and validation

To validate the inertial loss model and the dimensionless number Π_1, numerical simulations are carried out with different parameters. The ANSYS CFX software is used for the simulations. The geometry is presented in Figure 4.3, which corresponds to the case of a thin-wall vessel without frictional pressure

losses. The computational domain consists of the vessel (grey) and the spreading region (green). It is necessary to include the spreading region to correctly determine the pressure loss due to the constriction of the flow and the influence of air as ambient gas. The vessel with a volume V = 2 m³ has a length-to-diameter ratio of d_V/L_V = 1. For the simulations with a different vessel volume, the volume variation is adjusted to the length of the vessel L_V while keeping the diameter d_V constant. The ratio of the vessel thickness to the outlet diameter is L_2/d_2 = 1. Since the problem appears to be rotationally symmetric, the geometry is reduced to a 4° wedge, i.e., two-dimensional (2D) simulations are performed. Thus, only one cell is present in the azimuthal direction. Due to the points listed in section 3.3.2, a structured mesh is used. For better identification of the mesh structure, a coarse mesh with 6 871 cells is shown in Figure 4.3. The mesh fulfils different requirements from Paschedag (2006), as listed in section 3.3.2. The region is meshed in such a way that each cell belongs completely to the computational domain and the cell edges coincide with the edges of the geometry. The mesh resolution is oriented to the solution of the differential equation system. The mesh is structured and refined according to Oertel and Laurien (1995) in regions of great gradients. Therefore, the mesh in the region around the outlet has a finer resolution, which can be seen in the darker areas due to the higher number of mesh lines. The refinement of the mesh on the complete vessel wall on the outlet side does not appear to be necessary at this point, but is not possible in any other way due to the structured mesh. Furthermore, the cells should be oriented orthogonally to the main flow direction to minimise numerical diffusion.

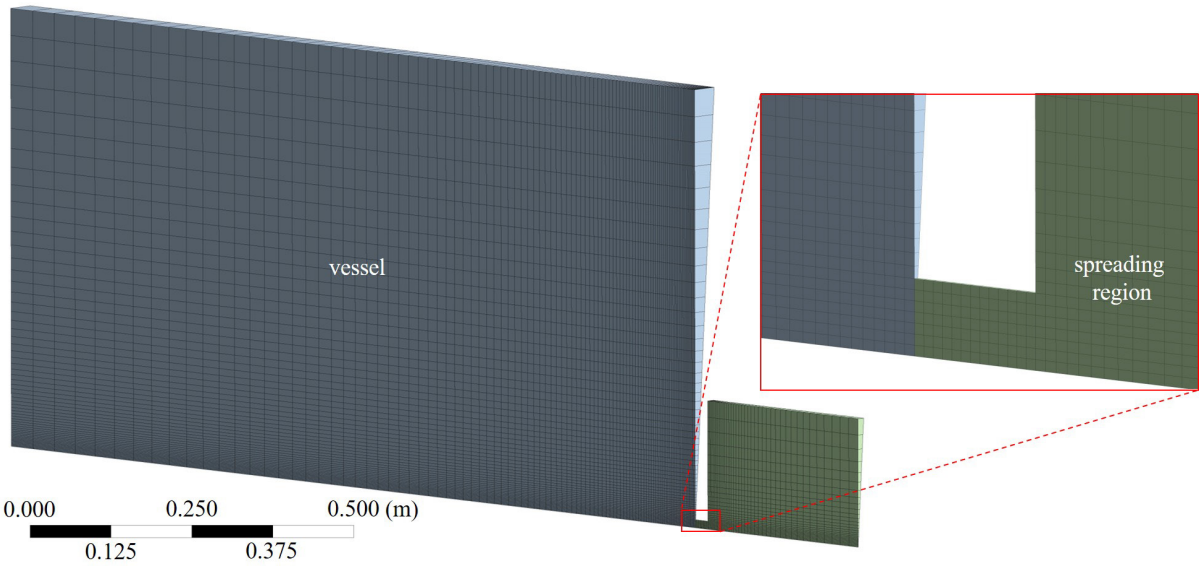

Figure 4.3.: Used geometry and coarse mesh with 6 871 elements for a vessel with V = 2 m³ and a vessel length-to-diameter ratio of L_V/D_V = 1.

The conservation equations for mass, momentum and energy in combination with the k-ε turbulence model according section 3.3.1.1 are used for the simulation. The following boundary conditions are used for the simulation. The vessel wall is defined as a no slip wall. This requires a no slip condition $u_{j,\mathrm{wall}} = 0$ m/s on the vessel wall and, in the case of an adiabatic wall, no heat flow through the wall,

i.e., $q_{\mathrm{wall}} = 0$ J/(m²·s). The assumption of an adiabatic wall is based on the work of Cumber (2001), according to which the influence of the heat flow from the vessel wall into the internal fluid during the discharge period is negligible. The cutting planes of the wedge have to fulfil a symmetry condition. Thus, that the velocity normal to the plane of symmetry is $u_n = 0$ m/s and the gradient of a scalar quantity normal to the plane is $\partial\phi / \partial \mathrm{n} = 0$. The edges of the spreading region are considered as opening, allowing for entrainment, with a static pressure of $p_{\mathrm{opening}} = 0$ Pa and $T_{\mathrm{opening}} = 298$ °C. Due to this boundary condition, gas can be drawn in by the entrainment effect and at the same time the gas flow can leave the computational domain. As an initial condition, the vessel has a defined pressure. Furthermore, a relative pressure of 0 Pa prevails in the spreading region and the initial temperature in the entire computational domain is at $T_0 = 298$ °C.

The maximum value of the residuals of 10^{-4} and an error of mass conservation of 0.01 were selected as convergence criteria. An important point that influences the convergence and robustness of the simulation is the choice of a reasonable time scale. The time step size Δt of the simulations is controlled by the maximum Courant–Friedrichs–Lewy number of the computational domain, i.e.

$$\mathrm{CFL} = \frac{u \Delta t}{\Delta x}, \tag{4.17}$$

defined according to Courant et al. (1928). To obtain a numerically stable solution, a maximum CFL number of CFL < 5 - 50 is specified for most of the simulations. To clarify, the maximum CFL number means that the CFL number may not be greater than this value at any point in the entire computational domain. This follows the requirement CFL < [1, 100] to ensure a stable solution according to Ferziger et al. (2020). Therefore, the initial time step size has to be very small with $\Delta t \approx 10^{-7}$ to 10^{-8} to achieve convergence at the high flow velocity of several hundred m/s. However, it is important to reduce the "increasing relaxation factor" for the time step to $\approx 10^{-5}$ to 10^{-7}. Otherwise, the phenomenon occurs where the time step size is increased by several orders of magnitude after the first time step and the simulation is aborted. This has to do with the fact that no notable velocity has been established in the first time steps and the CFL number is close to 0.

A grid-independence study is performed, according to section 3.3.3, to prove the convergence of the solution and the independence towards a mesh refinement. The mesh with 27 165 elements shown in Figure 4.3 corresponds to the mesh with a medium resolution. A coarser mesh with 6 871 elements and a finer mesh with 108 050 elements were also used in the grid independence study.

The results of the grid study are shown in the Figure 4.4. The pressure difference $p_1 - p_\infty$ is plotted against the time t. The curves for all resolutions overlap almost perfectly and there is hardly any deviation to be seen. Only the curve of the simulation with the fine mesh and $p_0 - p_\infty = 50\,000$ Pa is slightly above the simulations with coarser resolution, which corresponds to a slower pressure decrease.

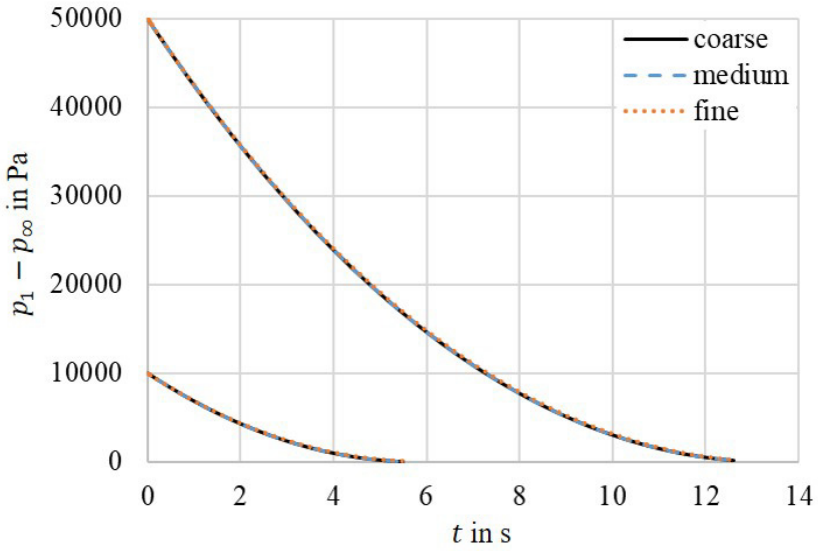

Figure 4.4.: Pressure difference $p_1 - p_\infty$ against time t for different mesh resolutions. Modified from PA2.

To better compare the simulations, the discharge duration t_{dis} is defined from the initial pressure difference $p_0 - p_\infty$ at the beginning of the discharge, i.e.

$$\Delta p(t_{\mathrm{dis}}) = 0.01(p_0 - p_\infty). \tag{4.18}$$

This definition is useful because the duration until the pressure difference of $\Delta p = 0$ is reached tends to infinity, $t \to \infty$. Table 4.1 shows the discharge durations t_{dis} of the mesh independency study. Since the simulation with the fine mesh and $p_0 - p_\infty = 50\,000$ Pa would have taken almost 100 days with a maximum CFL number of 5, the maximum CFL number was gradually increased from 5 to 100.

Table 4.1.: Overview of the results from the grid independence study with air and $p_\infty = 101\,300$ Pa. Reproduced from PA2.

Mesh	CFL	No. elements	$p_0 - p_\infty$ / Pa	t_{dis} / s	Mean t_{dis} / s	Deviation / %
coarse	5	6 871	10 000	5.264	5.277	-0.25
medium	5	27 165	10 000	5.257		-0.38
fine	5	108 050	10 000	5.297		0.38
coarse	5	6 871	50 000	11.997	12.021	-0.20
medium	5	27 165	50 000	11.990		-0.26
fine	5-100	108 050	50 000	12.075		0.45

Since the discharge durations t_{dis} do not have a clear trend, an extrapolation of the exact solution according to Ferziger et al. (2020) is not feasible in a logical way. The greater CFL number with the fine mesh for $p_0 - p_\infty = 50\,000$ Pa does not seem to have had a mentionable effect on the solution. The deviation is similar to the simulation with a fine mesh for $p_0 - p_\infty = 10\,000$ Pa where the CFL number

was left at CFL = 5. However, it can be shown that there is no grid dependency due to the small deviations of the discharge durations relative to the mean discharge duration of less than < 0.5 %. The deviations are thus smaller than the specified "conservation target" of 1 %. In most of the later simulations, the medium mesh is used. However, in a few simulations extremely long simulations times occurred, which is why the coarse mesh was used in such cases.

In the derivation of the Bernoulli discharge model, the assumption was used that the flow velocity in the vessel is almost zero, $c_1 \approx 0$, at all points with the exception of the outlet surroundings. This assumption is examined based on the numerical simulations. Figure 4.5 shows the flow velocity in the vessel and in the spreading region for a transient air outflow with an initial pressure of $p_0 = 50\,000$ Pa. Here, two points in time are considered—at the beginning with t = 0.5 s and at the end of the discharge t = 12 s. The representation is reduced to the regions where the velocity is greater than 1 % of the maximum velocity on the plane. This region inside the vessel has a radial extension of less than five outlet diameters d_2. Over the entire duration, the region within the vessel at which a mentionable velocity occurs changes only slightly. Therefore, a distance of the outlet to other walls or edges of more than five d_2 outlet diameters can be considered as a geometric requirement for the model.

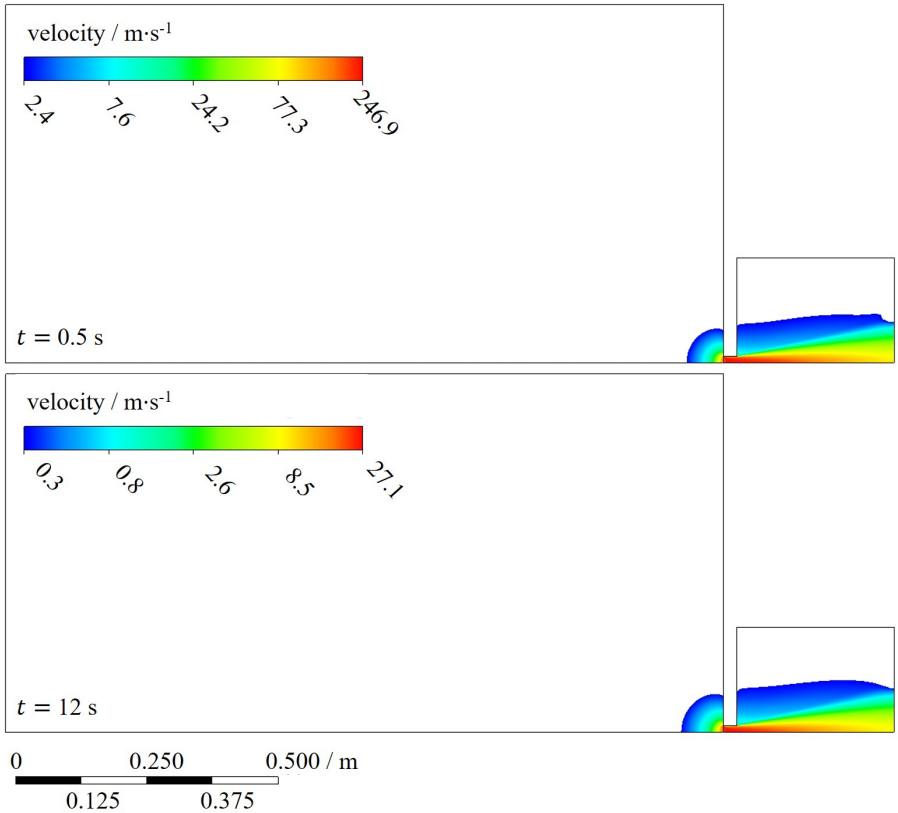

Figure 4.5.: Illustration of the regions where the velocity is greater than 1% of the maximum velocity of the free jet. Modified from PA1.

4.4. Parameter study

In this section, the results of the parameter studies with the ILM and the CFD simulations for the case of thin-wall vessels are presented. The aim is to determine a correlation for the dimensionless number Π_1 from equation (4.16) depending on several different parameters and to identify the dependencies. Therefore, the vessel volume V, the initial pressure inside the vessel p_0, the ambient pressure p_∞, the initial temperature T_0, the outlet diameter of the vessel d_2, the molar mass M and the heat capacity ratio κ of the discharged gas are varied. The outflow duration t_{dis} is then determined with either the inertial loss model from section 4.2 or numerical simulations (cf. section 4.3). The first parameter study is carried out with the inertial loss model. It was ensured that subcritical pressure conditions according to equation (2.12) were always present. Therefore, for example, no discharge duration t_{dis} was investigated for a propane outflow at p_0 = 180 000 Pa in an ambient pressure of p_∞ = 101 300 Pa. An overview of the different parameter sets can be found in Table 4.2, where the gas properties are taken from Linstrom (1997).

Table 4.2.: Overview of the varied parameters of the similarity model. Modified from PA2.

Gas / -	M / kg·mol^{-1}	κ / -	$p_0 - p_\infty$ / Pa	p_∞ / Pa	d_2 / m	V / m³	T_0 / K
air	0.0289	1.40	{1 000, 2 500, 5 000, 7 500, 10 000, 20 000, 30 000, 40 000, 50 000, 60 000, 70 000, 80 000}	{60 000, 80 000, 101 300, 201 300, 301 300, 401 300}	{0.025, 0.05, 0.075}	{1, 2, 4}	{298, 323, 373}
helium	0.0040	1.67					
hydrogen	0.0020	1.41					
methane	0.0160	1.31					
nitrogen	0.0280	1.40					
propane	0.0441	1.13					
sulphur dioxide	0.0640	1.28					

The evaluation of the parameter study showed that the dimensionless number Π_1 yields almost identical values for all gases at constant pressure differences if scaled with the ambient pressure $(p_0 - p_\infty)/p_\infty$. Thus, in Figure 4.6 the dimensionless number Π_1 is plotted against the dimensionless pressure difference $(p_0 - p_\infty)/p_\infty$. The individual values are linked with dotted regression curves. Since the numerator of the dimensionless number Π_1 contains the pressure difference $p_0 - p_\infty$, the curves must pass through the origin, and are therefore placed into the origin. The curves of the dimensionless number Π_1 increase with increasing pressure difference $p_0 - p_\infty$, whereby the gradient is decreasing for higher pressure differences. All in all, the curves overlap almost perfectly and no noticeable deviations can be detected.

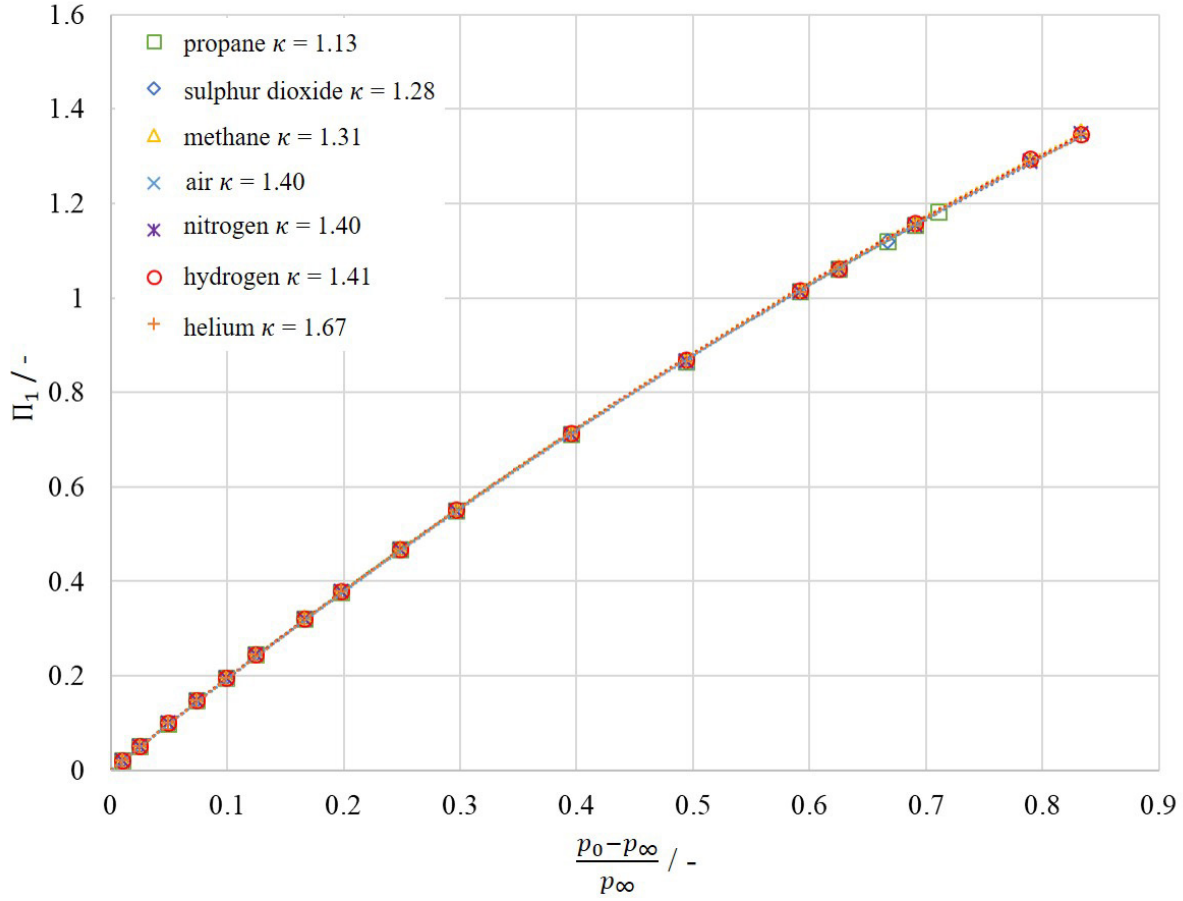

Figure 4.6.: Dimensionless number Π_1 plotted against the pressure ratio $(p_0 - p_\infty)/p_\infty$. Modified from PA2.

Thus, a universal correlation for describing the discharge behaviour for all gases at subcritical pressure conditions is developed. The function of Π_1 can be approximated with the quadratic function

$$\Pi_1 = a \left(\frac{p_0 - p_\infty}{p_\infty}\right)^2 + b \left(\frac{p_0 - p_\infty}{p_\infty}\right) = \frac{(p_0 - p_\infty)^{1/2} d_2^2 \, t_{\mathrm{dis}} \, \kappa}{V \left(\frac{p_0 M}{R \, T_0}\right)^{1/2}}. \tag{4.19}$$

The coefficients a = -0.4569 and b = 1.9899 result from a least-square fit of the curves from Figure 4.6. An overview of the individual regression curves is compiled in Table 4.3. The universal correlation of the new dimensionless number Π_1 is confirmed by small standard deviations and high coefficients of determination.

Table 4.3.: Quadratic functions of the dimensionless number Π_1. Reproduced from PA2.

Gas	a	b	Coefficient of determination R^2
propane	-0.47770	1.9990	0.99997
sulphur dioxide	-0.46614	1.9926	0.99995
methane	-0.45155	1.9935	0.99993
air	-0.43818	1.9748	0.99993
nitrogen	-0.45251	1.9879	0.99994
hydrogen	-0.45672	1.9937	0.99995
helium	-0.45552	1.9881	0.99994
mean value	**-0.4569**	**1.9899**	0.99994
standard deviation	0.01145	0.0071	$1.29 \cdot 10^{-5}$

This knowledge can now be used to determine the discharge duration t_{dis} for any subcritical, isentropic gas outflow from a thin-wall vessel. By rearranging the dimensionless number Π_1 from equation (4.16), the discharge duration can be determined as

$$t_{\mathrm{dis}} = \frac{\Pi_1 V \left(\frac{p_0 M}{R T_0}\right)^{0.5}}{(p_0 - p_\infty)^{0.5} d_2^2 \kappa}. \tag{4.20}$$

The dimensionless number Π_1 is determined by equation (4.19) using the averaged coefficients a = -0.4569 and b = 1.9899 from Table 4.3. All other variables, such as the vessel volume V in m³, the initial pressure p_0 in Pa, the ambient pressure p_∞ in Pa, the molar mass M in kg/mol, the ideal gas constant $R = 8.3145$ kJ/(kmol·K), the initial temperature T_0 in K, the outlet diameter d_2 in m and the heat capacity ratio κ, should be known for the calculation. In addition to the parameter study with the inertial loss model, a parameter study based on numerical simulations is carried out for validation. An overview of the varied setups can be found in Table 4.4. The table also lists the outflow durations t_{dis} of the simulations and the inertial loss model, which were defined according to equation (4.18). To be able to determine the influence of the variables of the dimensionless number Π_1, only one variable was varied per simulation. Thus, the vessel volume V, the initial temperature T_0, the outlet diameter d_2 and the molar mass M were varied. Subsequently, three initial pressures p_0 were considered for each gas, which also resulted in a variation of the heat capacity ratio κ. Overall, the differences of the discharge durations t_{dis} between the simulations, the ILM and the correlation based on the dimensionless number Π_1 are small. The largest deviations are found between the Π_1-correlation and the simulations at the smallest examined pressure difference of $p_0 - p_\infty$ = 10 000 Pa. However, for the helium discharge with the largest relative deviation of 4.844 % and -6.632 %, this only means an absolute error of 77 ms and 111 ms. The reason for this is probably that the curves of the ILM are not perfectly fitted and the Π_1-correlation based on them takes over these deviations. This theory is supported by the fact that the deviations from the ILM are smaller overall. Another reason for the deviations between the ILM and the simulations could be that the pressure loss coefficient ζ could be a function of the Reynolds number (Idel'Chik, 2008). This theory seems plausible because the constriction of the flow after passing through the orifice may well have a dependence on the flow velocity. Thus, different inlet pressures, and thus velocities and Reynolds numbers, do not cause a uniform deviation.

Table 4.4.: Overview and results of the parameter study performed with numerical simulations. Modified from PA2.

Gas	Mesh	CFL	M kg/mol	κ -	p_∞ Pa	$p_0 - p_\infty$ Pa	d_2 m	V m³	T_0 K	t_{dis} in s sim.	t_{dis} in s ILM	Deviation in % ILM/ sim.	t_{dis} in s Π_1-model	Deviation in % Π_1 model / sim.
air	medium	5	0.0289	1.40	101 300	10 000	0.025	**1**	298	2.629	2.550	3.095	2.502	-4.824
air	medium	5	0.0289	1.40	101 300	10 000	0.025	**2**	298	5.257	5.101	3.051	5.004	-4.803
air	medium	5	0.0289	1.40	101 300	10 000	0.025	**4**	298	10.518	10.200	3.144	10.008	-4.842
air	medium	5	0.0289	1.40	101 300	50 000	0.025	**1**	298	5.923	5.884	0.657	5.918	-0.077
air	medium	5	0.0289	1.40	101 300	50 000	0.025	**2**	298	11.990	11.770	1.872	11.836	-1.286
air	medium	50	0.0289	1.40	101 300	50 000	0.025	**4**	298	23.973	23.530	1.881	23.672	-1.253
air	medium	5	0.0289	1.40	101 300	50 000	0.025	2	**283**	12.167	12.080	0.721	12.146	-0.176
air	medium	5	0.0289	1.40	101 300	50 000	0.025	2	**298**	11.990	11.770	1.872	11.836	-1.286
air	medium	5	0.0289	1.40	101 300	50 000	0.025	2	**323**	11.524	11.300	1.983	11.369	-1.347
air	medium	5	0.0289	1.40	101 300	50 000	**0.025**	2	298	11.990	11.770	1.872	11.836	-1.286
air	medium	5	0.0289	1.40	101 300	50 000	**0.050**	2	298	3.017	2.942	2.555	2.959	-1.927
air	medium	5	0.0289	1.40	101 300	50 000	**0.075**	2	298	1.354	1.308	3.529	1.315	-2.882
air	medium	5	0.0289	1.40	101 300	**10 000**	0.025	2	298	5.257	5.101	3.051	5.004	-4.803
air	medium	5	0.0289	1.40	101 300	**20 000**	0.025	2	298	7.385	7.277	1.481	7.217	-2.275
air	medium	5	0.0289	1.40	101 300	**30 000**	0.025	2	298	9.096	8.985	1.241	8.977	-1.308
air	medium	5	0.0289	1.40	101 300	**40 000**	0.025	2	298	10.560	10.450	1.051	10.492	-0.640
air	medium	5	0.0289	1.40	101 300	**50 000**	0.025	2	298	11.990	11.770	1.872	11.836	-1.286
air	medium	5	0.0289	1.40	101 300	**60 000**	0.025	2	298	13.032	12.970	0.478	13.045	0.102
air	medium	5	0.0289	1.40	101 300	**70 000**	0.025	2	298	14.125	14.100	0.175	14.140	0.107
air	medium	5	0.0289	1.40	101 300	**80 000**	0.025	2	298	15.146	15.160	-0.092	15.132	-0.093
air	medium	5	0.0289	1.40	**201 300**	**10 000**	0.025	2	298	3.715	3.602	3.141	3.510	-5.529
air	medium	5	0.0289	1.40	**60 000**	**50 000**	0.025	2	298	15.753	15.610	0.917	15.540	-1.353
helium	medium	5	0.004	1.67	101 300	**10 000**	0.025	2	298	1.670	1.593	4.844	1.559	-6.632
helium	coarse	50	0.004	1.67	101 300	**40 000**	0.025	2	298	3.400	3.264	4.166	3.270	-3.835
helium	coarse	50	0.004	1.67	101 300	**70 000**	0.025	2	298	4.559	4.399	3.646	4.406	-3.359
hydrogen	medium	5	0.002	1.41	101 300	**10 000**	0.025	2	298	1.394	1.341	3.925	1.306	-6.288
hydrogen	coarse	50	0.002	1.41	101 300	**40 000**	0.025	2	298	2.837	2.748	3.229	2.738	-3.471
hydrogen	coarse	50	0.002	1.41	101 300	**70 000**	0.025	2	298	3.787	3.707	2.169	3.690	-2.566
methane	medium	5	0.016	1.31	101 300	**10 000**	0.025	2	298	4.139	4.069	1.726	3.976	-3.946
methane	medium	5	0.016	1.31	101 300	**40 000**	0.025	2	298	8.405	8.338	0.807	8.336	-0.822
methane	medium	5	0.016	1.31	101 300	**70 000**	0.025	2	298	11.356	11.250	0.945	11.234	-1.075
nitrogen	medium	5	0.028	1.40	101 300	**10 000**	0.025	2	298	5.096	5.020	1.516	4.921	-3.427
nitrogen	medium	5	0.028	1.40	101 300	**40 000**	0.025	2	298	10.390	10.290	0.967	10.319	-0.681
nitrogen	medium	5	0.028	1.40	101 300	**70 000**	0.025	2	298	13.900	13.880	0.142	13.906	0.046
propane	medium	5	0.0441	1.13	101 300	**10 000**	0.025	2	298	7.993	7.795	2.540	7.652	-4.264
propane	medium	5	0.0441	1.13	101 300	**40 000**	0.025	2	298	15.904	15.980	-0.473	16.044	0.880
propane	medium	5	0.0441	1.13	101 300	**70 000**	0.025	2	298	21.210	21.580	-1.713	21.622	1.940
sulphur dioxide	medium	5	0.064	1.28	101 300	**10 000**	0.025	2	298	8.534	8.292	2.923	8.138	-4.643
sulphur dioxide	medium	5	0.064	1.28	101 300	**40 000**	0.025	2	298	17.534	16.990	3.199	17.063	-2.683
sulphur dioxide	medium	50	0.064	1.28	101 300	**70 000**	0.025	2	298	23.391	22.930	2.011	22.995	-1.693
mean deviation in %												1.939		-2.343
max deviation in %												4.844		-6.632

Figure 4.7 shows a comparison between the numerical simulations and the ILM. For this purpose, the pressure difference $\Delta p = p_1 - p_\infty$ is plotted against time. Here, the discharge of a V = 2 m³ vessel, filled with air, is considered. Only at the largest examined pressure difference of $p_1 - p_\infty$ = 80 000 Pa does the curve of the ILM lie slightly above the curve of the simulation, and thus corresponds to a slower pressure reduction. In addition, not only does the outflow duration, as compared in Table 4.4, have a small deviation but the pressure curves over time also have a small deviation overall.

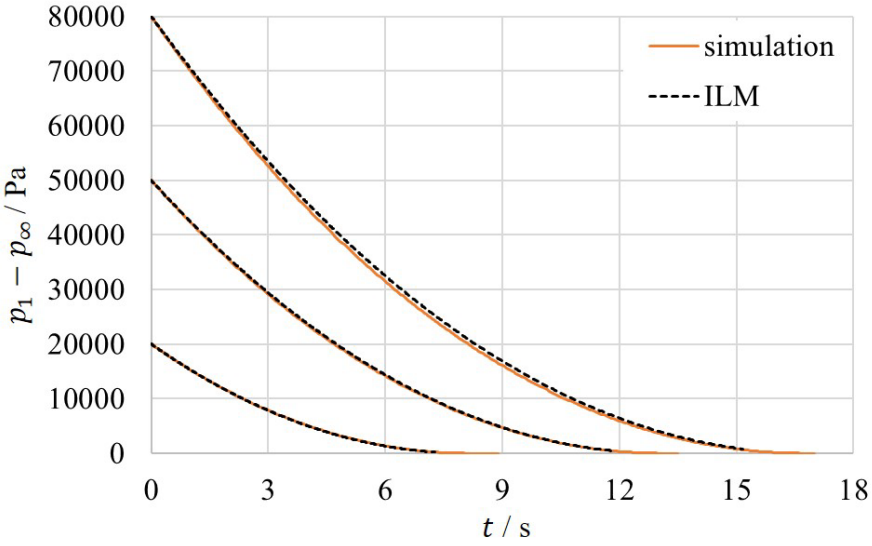

Figure 4.7.: Pressure difference $p_1 - p_\infty$ against time t for CFD simulations and the ILM. Modified from PA2.

4.5. Experimental validation

In this section, the FILM for the thick-wall vessel will be validated by means of experimental investigations. A pressure loss coefficient of ζ = 1.5 and a roughness of $K = 4 \cdot 10^{-5}$ m are used, which corresponds to the roughness of new steel pipes according to Kast and Nirschl (2013). The experimental setup used for this purpose is described in section 3.2. The setup deviates at only one point. A 0-1.6 bar pressure sensor *A-10* (I-2) (WIKA Alexander Wiegand SE & Co. KG, accuracy better than $\pm$ 0.17 %, settling time < 4 ms) is installed to measure the greater pressure differences. The vessel with a volume of V = 2.085 m³ is pressurised with various positive pressures and opened instantaneously. The gases used are air, carbon dioxide and helium, which are discharged into the air atmosphere. The results from these investigations are shown Table 4.5. To detect random measurement errors, a triple determination was carried out for each gas at each pressure. A comparison of the experimental data with the FILM shows that the discharge durations t_{dis} determined with the FILM are on average -1.75 % smaller. The deviations to the experimental data are greatest with -9.63 % for the helium discharge with an initial pressure

difference of $p_0 - p_\infty$ = 60 000 Pa. The discharge durations of carbon dioxide at an initial pressure difference of $p_0 - p_\infty$ = 10000 Pa and $p_0 - p_\infty$ = 20000 Pa deviate considerably more from the FILM than those of the higher initial pressure differences. This is probably because the vessel was not perfectly charged with carbon dioxide at the beginning of the test series but still contained some remaining air, which was diluted with the number of tests.

Table 4.5.: Overview and results of the experiments to validate the FILM.

Gas	$p_0 - p_\infty$	T_0	$\sigma(T_0)$ exp.	t_{dis} exp.	$\sigma(t_{\mathrm{dis}})$ exp.	t_{dis} FILM	Deviation FILM / exp.
	Pa	° C	s	s	s	s	%
air	10 000	26.04	0.17	6.11	0.03	5.81	-4.86
air	20 000	26.29	0.27	8.00	0.16	8.15	1.82
air	30 000	26.41	0.28	10.04	0.15	10.1	0.57
air	40 000	26.30	0.03	11.84	0.08	11.69	-1.23
air	50 000	28.60	0.96	13.02	0.20	13.15	1.00
air	60 000	29.57	0.94	14.47	0.07	14.43	-0.25
air	70 000	31.59	0.63	15.64	0.08	15.67	0.19
air	80 000	30.69	1.29	17.18	0.27	16.87	-1.80
CO_2	10 000	22.35	0.16	7.04	0.22	7.66	8.74
CO_2	20 000	23.70	0.22	10.44	0.03	11.29	8.19
CO_2	30 000	24.76	2.06	13.21	0.08	13.37	1.17
CO_2	40 000	24.91	1.57	15.61	0.16	15.57	-0.23
CO_2	50 000	24.65	1.33	17.52	0.19	17.51	-0.06
CO_2	60 000	24.48	0.21	19.38	0.03	19.3	-0.39
CO_2	70 000	26.28	1.12	21.24	0.08	20.92	-1.50
CO_2	80 000	29.26	1.34	22.33	0.41	22.38	0.22
helium	10 000	23.84	0.32	1.92	0.02	1.84	-4.27
helium	20 000	23.27	0.37	2.76	0.37	2.62	-5.14
helium	30 000	23.47	0.24	3.39	0.03	3.21	-5.25
helium	40 000	23.63	0.27	3.95	0.05	3.73	-5.56
helium	50 000	23.36	0.75	4.45	0.02	4.19	-5.86
helium	60 000	24.57	0.43	5.11	0.10	4.62	-9.63
helium	70 000	26.39	0.44	5.46	0.02	4.98	-8.81
helium	80 000	26.06	0.30	5.90	0.02	5.37	-9.00
mean deviation in %							-1.75
max deviation in %							-9.63

For further qualitative analysis, Figure 4.8 shows the pressure difference $p_1 - p_\infty$ against time t for the different gases and different initial pressures p_0 for the FILM and the experiments. The error bars, which show the standard deviation of the experiments, are so small that they are hardly visible. Especially for the smaller initial pressure differences $p_0 - p_\infty$, the profiles of the FILM and the experiments are almost congruent. For the larger initial pressure differences $p_1 - p_\infty$, deviations occur in the intermediate times of the outflow. These deviations disappear towards the end of the outflow period. This is probably due to the fact that the 0–1600 mbar sensor used here had problems with the temporal resolution of the greater pressure gradients. These deviations are not visible with the 0–600 mbar sensor used for the latter PDA tests (cf. Figure 5.4). The idea that it is more of a problem of the measurement system is supported by the fact that all of the sample simulations of thick-wall vessels have shown practically identical pressure curves to the FILM. There is a great correspondence between the experimental profiles and the profiles of the FILM.

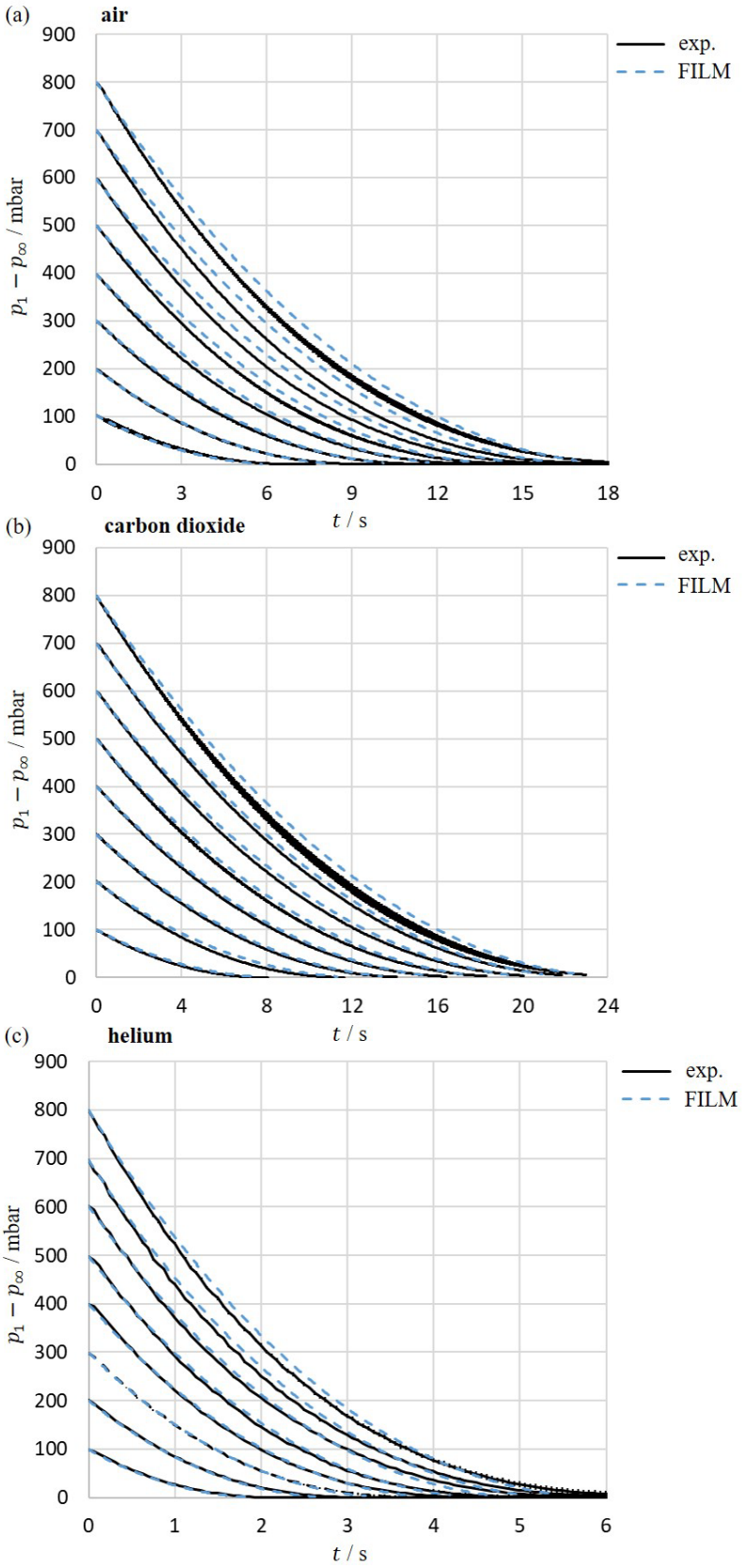

Figure 4.8.: Pressure difference $p_1 - p_\infty$ against time t based on experimental data (exp.) and the FILM for (a) air, (b) carbon dioxide and (c) helium. Error bars indicate the standard deviation.

One assumption in the derivation of the model was an adiabatic system. To check this assumption, the heat flux from the vessel wall to the internal gas during the discharge is to be estimated. Thus, the gas cools down during the discharge due to its expansion. The temperature difference between the cold gas and the warmer vessel wall is the driving force for a heat flow. An estimation is carried out based on an energy balance of the gas phase, namely

$$mc_p \frac{dT}{dt} = \alpha_h A_V (T_w - T_1). \tag{4.21}$$

Here, m is the gas mass inside the vessel, c_p is the specific heat capacity at constant pressure of the gas, α_h is the heat transfer coefficient, A_V is the vessel surface, T_w is the temperature of the vessel wall and T_1 is the temperature inside the vessel. For a worst-case estimate, the gas mass is not considered as a function of time but the smallest gas mass at the end of the discharge is used. Although the specific heat capacity of steel is smaller than that of the most gases $c_{p,\mathrm{steel}} < c_{p,\mathrm{gas}}$, see Linstrom (1997), the temperature change of the vessel wall is negligible, and is therefore considered constant T_w =const. The reason for this is that the mass of the vessel is considerably greater than the mass of the gas, and thus the extensive heat capacity of the vessel is so great that the cooling of the vessel wall by the colder gas inside is negligible. The heat transfer coefficient α_h is determined experimentally for the test setup described in section 3.2. For this purpose, discharge experiments are carried out in which the subsequent heating of the internal gas is measured. By solving equation (4.21), the following equation to determine the internal gas temperature $T_1(t)$ is derived

$$T_1 = T_w - (T_w - T_{dis}) \cdot \exp\left(-\frac{\alpha_h A_V}{mc_p} t\right). \tag{4.22}$$

Here, T_{dis} is the gas temperature after the discharge, which represents the start of the heating. The heating is modelled with equation (4.22) at a mean deviation of 0.27 %. A fitted heat transfer coefficient of α_h = 4.99 W/(m²·K) is used. The knowledge about the heat transfer coefficient α_h is now used to calculate the heat flow during the discharge process. The result is that the temperature inside the vessel is only increased by 1.02 % on average by the vessel wall during the discharge duration. According to the ideal gas law (cf. equation (3.11)), this is equivalent to a pressure change of 1.02 %, which should be negligible. This justifies the assumption of an adiabatic vessel wall and fits with the results of Cumber (2001) and Rist (1996).

4.6. Findings on the prediction of vessel discharges

Based on a parameter study of the ILM, it was shown that the dimensionless number Π_1 is able to describe transient, subcritical, adiabatic pressure reliefs of thin-wall vessels for arbitrary ideal gases. The influence of the ambient pressure p_∞ is captured by scaling the pressure difference $p_0 - p_\infty$. Thus, a plot of the dimensionless number Π_1 against the dimensionless pressure difference $(p_0 - p_\infty)/p_\infty$

results in a single curve that obtains all parameter settings. This means that it is possible to determine all isentropic, subcritical discharges from thin-wall, adiabatic pressure vessels with equations (4.19) and (4.20) within a few seconds. The mean deviation of the inertial loss model to the simulations is only 1.939 % and of the Π_1-correlation to the simulations only -2.343 %. The Π_1-correlation is characterised by its generality, fast and accurate solution, and is therefore a practical tool for calculating the discharge duration of any isentropic, adiabatic, subcritical pressure discharge. In particular, because it does not require complex numerical simulations or calculations of differential equations, it is a practical tool in daily engineering life.

The mean deviation between the FILM for thick-wall vessels and the experiments is -1.75 %. This shows that it is possible to determine the outflow duration, even for more complex problems with frictional pressure losses, quickly and accurately.

5. Experimental investigation of transient free jets

In this chapter, transient, horizontal air, carbon dioxide and helium jets formed during sudden pressure reliefs of a vessel are experimentally investigated. The velocity field of the transient free jets formed at the vessel outlet is measured with a LDA and PDA system. A statistical analysis of these data provides information as to whether and in what form a statistically significant relationship exists between the Reynolds number and gas density on the propagation. Furthermore, whether a self-similarity of the velocity field can also be observed for transient free jets is investigated.

5.1. Introduction into experimental investigation of transient free jets

Most of the studies presented in chapter 2 have in common that they have investigated stationary free jets. The self-similarity of stationary free jets has thus been extensively investigated and is considered valid (Chen and Rodi, 1980). The situation is different for transient free jets because there is much less experimental data in this case. In addition, the studies to date are theoretical or numerical (Abraham, 1996) or focus on sudden decreases of the outlet velocity (Borée et al., 1996). A transient free jet, which occurs when a pressure vessel is opened suddenly, has hardly been investigated to date. Since transient jets are examined, a continuous temporal variation of the Reynolds number is directly connected to this. Thus, the question of the self-similarity of transient free jets will be investigated as well as the Reynolds number dependence of free jets.

5.2. Measuring procedure

The experimental setup used is described in detail in section 3.2. For the experiments with carbon dioxide and helium, it is important that these gases are present in the pressure vessel as an initial condition at the highest possible concentration to minimise measurement errors. This process was monitored by means of the gas concentration meter (I-8) and only ended when the concentration exceeded > 99 %. The filling with carbon dioxide was carried out accordingly from below via line (P-2), so that the less dense air is displaced upwards.

[PPA1] Parts of this chapter are based on the article: Measurement of the Reynolds number dependence of a transient air jet from a pressure vessel by M.-D. Fischer, F. Ryll and K. Boettcher; it was first published as preprint article on Research Square, 2022 and is licensed under a Creative Commons Attribution 4.0 International License (http://creativecommons.org/licence/by/4.0/).
The following advisory/analysis services of the Statistical Consulting and Analysis Centre for Higher Education TU Dortmund University were used for this chapter: statistical methodology, selection of statistical software and statistical programming using R Core Team (2022), data analysis and statistical formulation of text passages.

This procedure does not need to be repeated for the subsequent tests because the vessel is closed again after each discharge experiment. After the first filling with a gas, the following measuring procedure can be carried out. The valves (V-3) and (V-1) are opened and by means of the pressure reducer (V-2) a pressure of about 700 mbar is set for filling the vessel. During filling, an aerosol of liquid ethylene glycol particles is generated inside the vessel by a fog machine. As soon as the internal vessel pressure is p_0 = 510 mbar, the filling process is stopped and the valves (V-3) and (V-1) are closed. At p_0 = 510 mbar, the internal vessel pressure is slightly above the desired pressure of p_0 = 500 mbar because the gas is heated by the compression and thus expands. Therefore, after the filling process is completed, waiting is required until the temperature has dropped and a pressure of p_0 = 500 mbar has been reached. The data recording of the temperature (I-3, I-4; I-5), pressure sensors (I-2) and the PDA system (I-7) is then started. The ball valve (V-5) must be opened and the quick valve (V-6) will be opened via a controller. After the outflow has stopped, the vessel is closed again by means of the ball valve (V-5). This prevents air from flowing into the vessel and thus contaminating the gas inside.

5.3. Evaluation methods

Since turbulent free jets are investigated, temporal fluctuations are present, which complicate an evaluation of the flow behaviour. To determine the decay constant $K_{1,u}$ and the spreading rate $K_{2,u}$, it is necessary to determine the mean velocity. To solve this problem, the velocity can be divided into a time averaged $\bar{u}(\vec{x})$ and a turbulent fluctuation $u'(\vec{x},t)$ according to Reynolds (1895), i.e.

$$u(\vec{x},t) = \bar{u}(\vec{x}) + u'(\vec{x},t). \tag{5.1}$$

For stationary flows, the time average velocity $\bar{u}(\vec{x})$ can be easily determined via

$$\bar{u}(\vec{x}) = \lim_{\Delta t \to \infty} \frac{1}{\Delta \hat{t}} \int_{t}^{t+\Delta \hat{t}} u(\vec{x},t)\, dt. \tag{5.2}$$

However, since transient flows are being investigated here, the mean flow velocity is dependent on time. Assuming an ergodic process, averaging over time intervalls can be used instead of averaging several different tests. Thus, the challenge is to define an averaging interval $\Delta \hat{t}$ that is large enough to filter the turbulent fluctuations and small enough not to misrepresent the transient flow character. The time-dependent mean velocity, which is calculated by averaging over a smaller finite time step, is defined as the current mean velocity $\hat{u}(\vec{x},t)$. Since it is further investigated if the assumption of a perfect following behaviour is valid, and thus whether the tracer particles have adopted the gas velocity, the velocity is first related to the particles. Generally, the average process is based on all particle sizes. To determine an appropriate time step size, the temporal velocity behaviour at the pipe outlet $\vec{x}$ = (1d, 0, 0) is considered in Figure 5.1 for the transient (a) air jet, (b) carbon dioxide jet and (c) helium jet. Therefore, the velocity of the tracer particles at the pipe outlet $u_{0,p}$ is plotted against time t. The black circles are the

raw data including all particles d_p < 14 µm, which seem to have a linear temporal behaviour. This means that the averaging interval $\Delta\hat{t}$ can be chosen to be relatively large, thereby the earlier ($t - \Delta\hat{t}/2$), faster and later ($t + \Delta\hat{t}/2$), slower data points are balanced out. An averaging interval of $\Delta\hat{t}$ = 0.5 s is used to calculate the current mean velocity

$$\hat{u}(\vec{x}, t) = \frac{1}{\Delta\hat{t}} \int_{t-\frac{\Delta\hat{t}}{2}}^{t+\frac{\Delta\hat{t}}{2}} u(\vec{x}, t)\, dt. \tag{5.3}$$

In addition to the raw data (black circles), the current mean particle velocity $\hat{u}_{cl,p}(x = 1d, t)$ of the particle class d_{pc} = 0.5 µm (blue cirlces), d_{pc} = 2.5 µm (orange circles), d_{pc} = 6.5 µm (turquoise circles) and d_{pc} = 11.5 µm (violet circles) are shown. The current mean particle velocity $\hat{u}_{cl,p}$ starts after t = 0.25 s because this is the midpoint of the averaging interval. The deviating points of the raw data are measurement errors. These amount to less than 0.1 % of the raw data, and are therefore negligible. The fact that the velocity does not drop to zero at the end of the outflow is not an error. The gas in the vessel has cooled down due to the pressure drop and is then heated up again by the heat flow from the vessel wall. This temperature increase in turn causes a pressure increase in the vessel and generates a flow. In the case of the helium jet, the maximum measurable velocity of the PDA system of 433 m/s was exceeded for the two axial positions measured closest to the outlet $\vec{x}$ = (25, 0, 0) mm and $\vec{x}$ = (105, 0, 0) mm for t < 2 s. This was not the case for the air and carbon dioxide jet because the maximum velocity was much lower at around u = 200 - 250 m/s. However, the position $\vec{x}$ = (25, 0, 0) mm is particularly important for the scaling of the subsequent axial velocity profiles. The almost perfect linear temporal behaviour of the velocity at a specific position was used for the determination. Thus, the velocity could be determined for times t < 2 s based on a linear extrapolation.

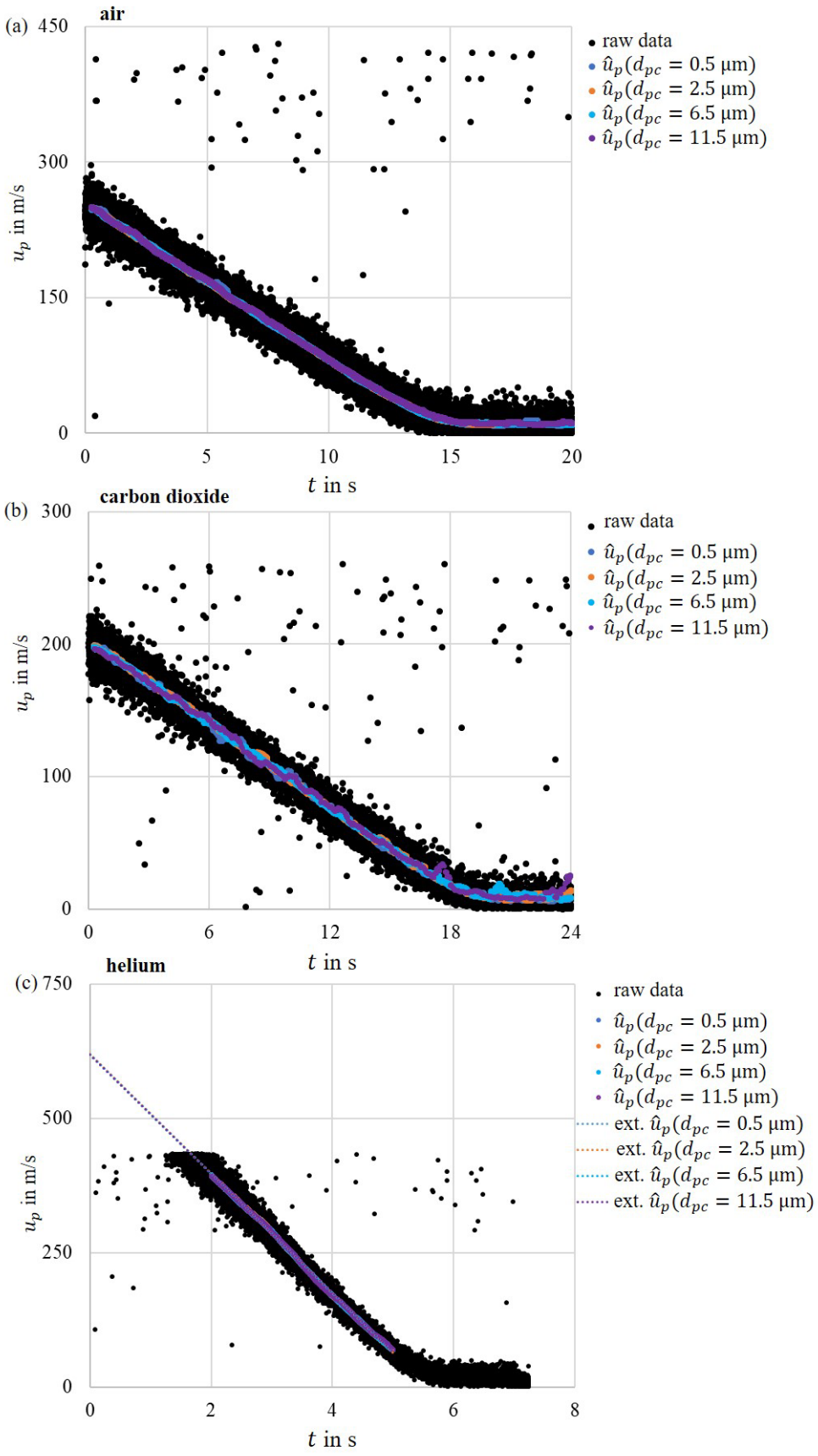

Figure 5.1.: Particle velocity u_p plotted against the time t for different particle classes d_{pc} at the pipe outlet $x = 1\ d$: (a) air jet, (b) carbon dioxide jet and (c) helium jet including extrapolations (ext.) for $t < 2$ s. Modified from PPA1.

The functions of the linear regression are summarised in Table 5.1. The assumption of a linear temporal behaviour of the velocity at a constant position is supported by the high coefficient of determination for the linear regression. The linear regressions are based on the averaging intervals $0 < t < 14$ s for air, $0 < t < 18$ s for carbon dioxide and $2 < t < 5$ s for helium.

Table 5.1.: Linear regression of the particle velocity $\hat{u}_p$ at the pipe outlet for the different particle classes.

		Air			Carbon dioxide			Helium		
d_p	d_{pc}	$\partial\hat{u}/\partial t$	$\hat{u}(t=0)$	R^2	$\partial\hat{u}/\partial t$	$\hat{u}(t=0)$	R^2	$\partial\hat{u}/\partial t$	$\hat{u}(t=0)$	R^2
µm	µm	m/s²	m/s	-	m/s²	m/s	-	m/s²	m/s	-
0										
1	0.5	-17.05	252.79	0.9988	-10.48	202.69	0.9988	-111.00	618.93	0.9988
4	2.5	-16.91	251.49	0.9992	-10.45	202.99	0.9993	-111.49	620.53	0.9989
9	6.5	-16.97	252.04	0.9994	-10.40	202.28	0.9995	-111.12	618.99	0.9990
14	11.5	-16.87	251.66	0.9990	-10.29	201.51	0.9982	-110.81	618.33	0.9989
	mean	-16.95	252.00	0.9991	-10.41	202.37	0.9990	-111.11	619.20	0.9989
	standard deviation	0.07	0.50	$2.24 \cdot 10^{-4}$	0.07	0.56	$5.02 \cdot 10^{-4}$	0.25	0.81	$7.07 \cdot 10^{-5}$

Since the ability of particles to follow the gas flow is considerably dependent on their size, the particles are divided into size classes during the evaluation. The aim is to determine the actual gas velocity as accurately as possible. If the velocities are the same for different particle classes, then it can be assumed that the actual gas velocity has been detected and the relative velocity between particle and gas phase is negligible. For the classification into particle classes, the cumulative number distribution Q_0 for the centre-line positions $x = 1\ d$ and $x = 60.2\ d$ is considered in Figure 5.2. Here, 34 917 - 66 963 particles were measure at the position $x = 1\ d$ and 942 - 3338 particles at the position $x = 60.2\ d$. More than 90 % of the particles are of a size $d_p < 15$ µm. Furthermore, the distribution shifts towards smaller particle diameters with increasing axial distance x. This is probably due to the evaporation of the liquid tracer particles, and thus the particles become smaller downstream. According to Walzel and Tropea (2004), an aerodynamic breakup is not to be expected because both the particle size d_p and the relative velocity between particle and gas phase are too small in the present case.

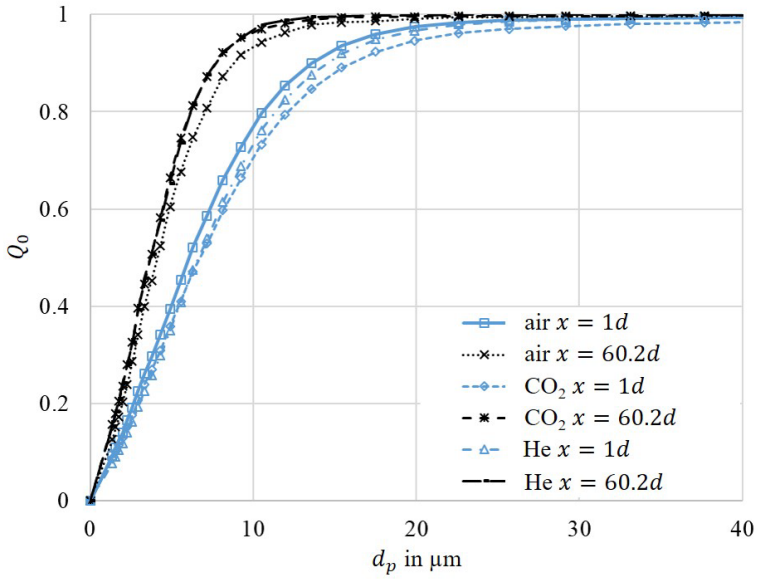

Figure 5.2.: Particle-size distribution Q_0 against the tracer particle diameter d_p for the nearest and furthest position on the centre line. Modified from PPA1.

Based on this knowledge, the limits for the particle classes d_p and class centres d_{pc} are defined in Table 5.2. The class widths increase as the particle diameter increases because the number density decreases. The exit Stokes number St_0 according to Stieß (1997) is introduced, to evaluate the following behaviour of the particles. It puts the relaxation length in relation to the characteristic flow length, in this case the pipe diameter d. The definition is

$$St_0 = \frac{\varrho_p d_p^2 \left|\hat{u}_0 - \hat{u}_{0,p}\right|}{18 \mu_{in} d}, \tag{5.4}$$

where $\hat{u}_{0,p}$ is the current mean particle velocity and $\hat{u}_0$ the current mean gas velocity at the pipe exit. The current mean gas velocity at the pipe exit $\hat{u}_0$ is determined on the assumption that the particle classes with $d_{pc} \leq 16.5$ µm have adopted the gas velocity. This assumption is based on the idea that these classes have almost the same velocity, and therefore must have the gas velocity. According to Stieß (1997), an outlet Stokes number $St_0 \ll 1$ corresponds to a perfect following behaviour and it can be assumed that particles with a diameter smaller $d_{pc} \leq 11.5$ µm will have the gas velocity (cf. Table 5.2). It must be mentioned that the PDA system is limited by the wavelength to a minimum measurable particle diameter. Therefore, the later results for the particle class $d_{pc} = 0.5$ µm are to be excluded if they appear unphysical.

Table 5.2.: Overview of the defined particle classes and their corresponding outlet Stokes number St_0. Modified from PPA1.

		Air ($t \approx 0.25\ s$)			Carbon dioxide($t \approx 0.25\ s$)			Helium($t \approx 2\ s$)		
d_p	d_{pc}	$\hat{u}_{0,p}$	$\hat{u}_{0,p} - \hat{u}_0$	St_0	$\hat{u}_{0,p}$	$\hat{u}_{0,p} - \hat{u}_0$	St_0	$\hat{u}_{0,p}$	$\hat{u}_{0,p} - \hat{u}_0$	St_0
µm	µm	m·s^{-1}	m·s^{-1}	-	m·s^{-1}	m·s^{-1}	-	m·s^{-1}	m·s^{-1}	-
0										
1	0.5	247.04	-1.68	$5.74 \cdot 10^{-5}$	198.63	0.81	$6.03 \cdot 10^{-5}$	393.30	-0.69	$3.88 \cdot 10^{-5}$
4	2.5	249.63	0.91	$7.24 \cdot 10^{-4}$	198.78	0.96	$1.79 \cdot 10^{-3}$	394.28	0.29	$4.10 \cdot 10^{-4}$
9	6.5	248.77	0.04	$2.42 \cdot 10^{-4}$	197.90	0.07	$9.27 \cdot 10^{-4}$	394.64	0.65	$6.13 \cdot 10^{-3}$
14	11.5	249.45	0.73	0.01	195.98	-1.85	0.07	393.74	-0.25	$7.33 \cdot 10^{-3}$
19	16.5	249.32	0.60	0.02	194.99	-2.83	0.23	394.19	0.20	0.01
26	22.5	255.74	7.02	0.45	195.17	-2.65	0.40	393.58	-0.41	0.05
35	30.5	255.46	6.73	0.80	192.14	-5.68	1.57	394.30	0.31	0.06
48	41.5	274.96	26.24	5.75	201.01	3.19	1.64	393.33	-0.66	0.25
71	59.5	334.11	85.38	38.44	190.29	-7.53	7.94	313.36	-80.63	63.84
114	92.5	322.61	73.88	80.39	198.60	0.78	1.98	371.05	-22.94	43.89
mean	< 16.5	248.72	$-5.42 \cdot 10^{-14}$	0.01	197.82	$1.42 \cdot 10^{-14}$	0.02	393.99	$4.26 \cdot 10^{-14}$	$3.48 \cdot 10^{-3}$
σ	< 16.5	1.18	1.18	$7.5 \cdot 10^{-3}$	1.12	1.12	0.03	0.51	0.51	$3.28 \cdot 10^{-3}$

It is noticeable that the particle velocity appears to increase for the larger-particle classes. The reason for this is explained by Figure 5.3 for the example of the transient air jet. In Figure 5.3, the current mean particle velocity $\hat{u}_{cl,p}(x = 1d, t)$ is plotted against the time t for different particle classes. To illustrate which and how the particle classes are affected by measurement errors, Figure 5.3 is divided into two charts. Chart (a) shows all particle classes $d_{pc} < 16.5$ µm and chart (b) shows all particle classes $d_{pc} \geq 16.5$ µm. The measuring points for the particle classes $d_p < 16.5$ µm lie almost perfectly on top of each other and have a mean relative standard deviation of 0.76 % during the discharge. For greater particle diameters, the measured particle velocities shift to the upper measuring range. This behaviour cannot be explained physically, especially for the particles that seem to be faster than the speed of sound (cf. eq. (2.9)), and can only be explained by measurement errors. One of the most common measurement errors is caused by multiple particles in the measurement volume in very dense sprays, where superimposed refraction and diffraction phenomena occur (Dantec Dynamics A/S, 2011). This leads to noise in the measurement signal, which, if the validation limits are not sufficiently hard, can result in apparently large particles with apparently high velocities.

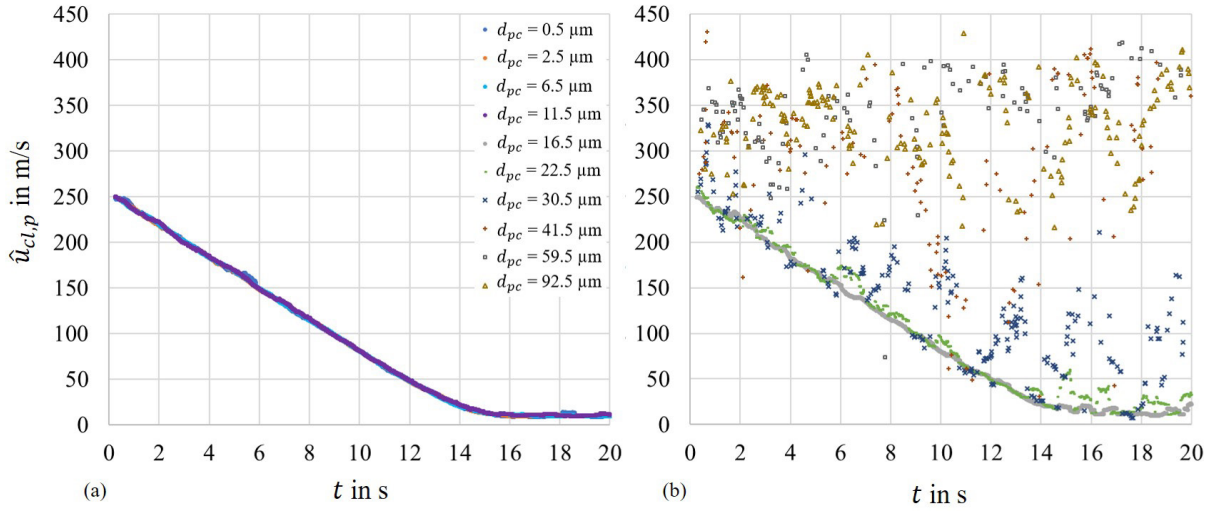

Figure 5.3.: Current mean particle velocity $\hat{u}_p$ against time t for different particle classes $\hat{u}_{cl,p}(x = 1d, t)$ at the pipe outlet for the transient air jet. (a) $d_{pc} < 16.5$ µm, (b) $d_{pc} \geq 16.5$ µm. Modified from PPA1.

Furthermore, positions with negative z-coordinate below the x-axis are increasingly affected by signal noise because the light that is collected by the receiver must pass through the free jet for this purpose, resulting in (unwanted) interactions of the light with other tracers. The idea that the deviations in particle velocity are due to additional refraction and diffraction phenomena in very dense sprays is supported by the fact that the deviations become less frequent at positions that are farther away from the outlet, where the tracer load is less dense. It would have been possible to further limit these measurement errors by specifying harder validation criteria, such as by using a higher signal-to-noise ratio and a longer recording length, but this always leads to a great drop of the overall data rate. A drop of the overall data rate also means that many valid particles are not detected, for example, because a longer record length of the burst signals is used. Therefore, it makes sense to choose a trade-off with a first somewhat lower validation level to generate a larger amount of raw data and then to filter out the measurement errors in a second step, especially because the measurement errors can be clearly identified. This shows that it is useful to perform a particle-size-specific evaluation because it adds an additional method to the data evaluation. Furthermore, the axial velocity profile depending on the particle size was modelled with a linear regression according to Fahrmeir et al. (2016). This analysis shows no significant influence (p-value = 0.225) of the particle size for $d_{pc} < 16.5$ µm on the velocity field. Based on this analysis, the velocity of the particle classes $d_{pc} < 16.5$ µm will no longer be referred to as particle velocity but as gas velocity.

5.4. Reproducibility

Since the LDA technique used to measure the velocity is a point-like measurement method, the velocity field in space must be assembled from several individual experiments. Reproducibility is assumed in the form that the velocity field from a discharge experiment corresponds to the velocity field, which has been assembled by other individual experiments. Since the discharge velocity is largely related to the vessel pressure and temperature, the variances of the pressure and temperature curves against time are considered first. For this purpose, Figure 5.4 plots the internal vessel pressure p_1 (I-2) and internal vessel temperature T_1 (I-5), as well as the ambient temperature T_∞ (I-4) against time t. The curves result from an average over all discharge experiments. The time $t = 0$ was defined based on the sudden change in the internal vessel pressure. The pressure curves have the greatest gradient at the beginning of the discharge and decrease strictly monotonously. For air and carbon dioxide, the pressure curves from the experiment and the FILM can hardly be distinguished because they have such a small deviation. This supports the idea that the deviations between the FILM and the experiments previously observed in section 4.5 could be related to the other 0–1.6 bar pressure sensor, which is an *A-10* (I-2) (WIKA Alexander Wiegand SE & Co. KG).

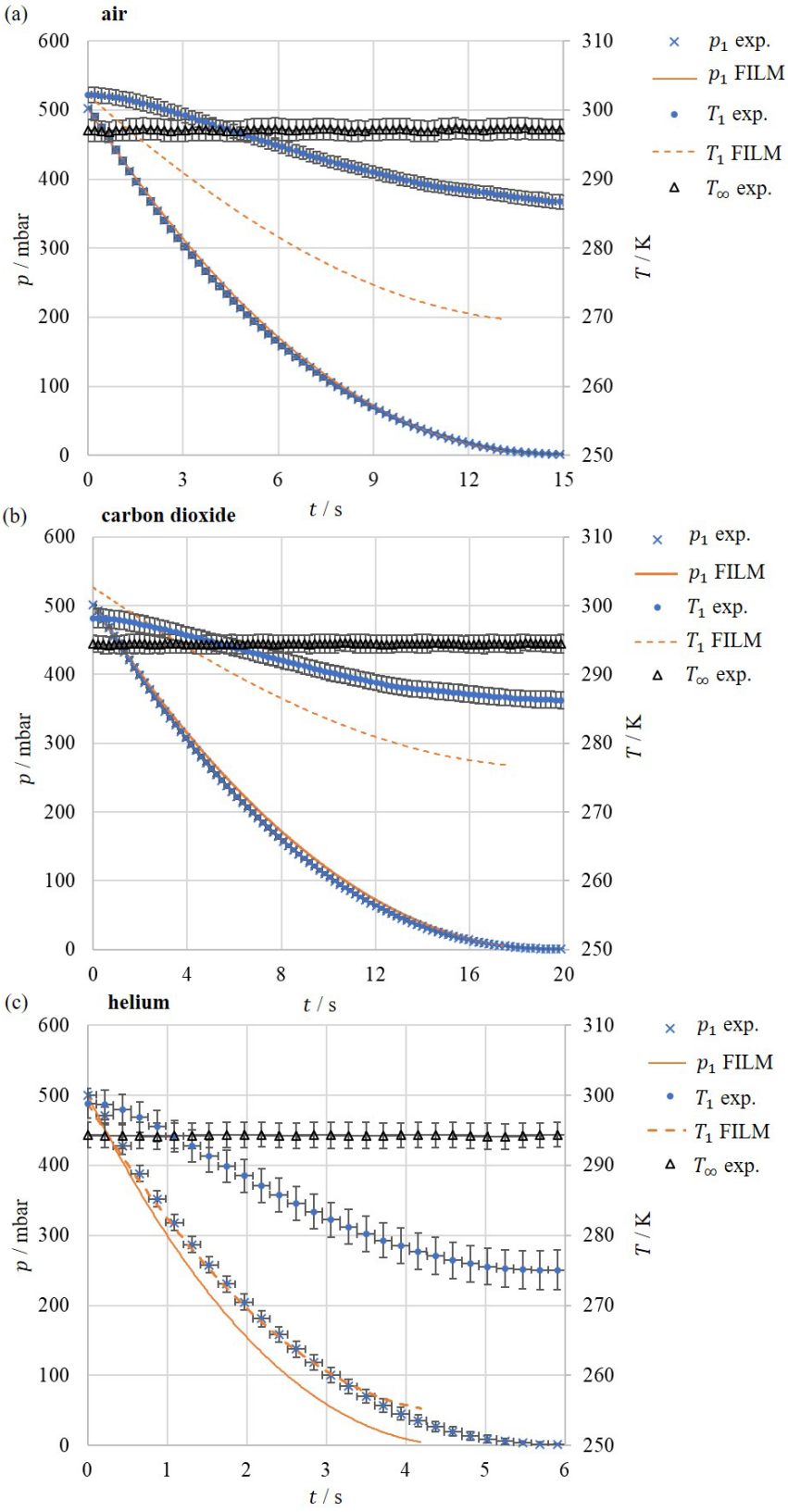

Figure 5.4.: Internal vessel pressure p_1, internal vessel temperature T_1 and ambient temperature T_∞ against time t average of all experiments for each gas compared with the FILM. Error bars indicate the standard deviation. Modified from PPA1.

An overview of the outflow durations determined experimentally and with the FILM can be found in Table 5.3.

Table 5.3.: Overview of the discharge durations determined experimentally (exp.) and with the frictional and inertial loss model (FILM)

	Air		Carbon dioxide		Helium	
	exp.	FILM	exp.	FILM	exp.	FILM
t_{dis} / s	13.66	13.17	17.55	17.52	5.33	4.19

The discharge durations of the FILM are -3.59 %, -0.17 % and -21.39 %, which are smaller than the discharge durations determined experimentally for air, carbon dioxide and helium. The experimental profiles and discharge durations t_{dis} of helium differ here from those in section 4.5. This is because in the time sequence the PDA tests with helium were done first and the individual segments of the outlet pipe were not perfectly aligned, which led to offsets relative to the pipe. This led to an increase of the pressure loss Δp_{loss} in the pipe, and thus to a slowing down of the outflow. This was only discovered and corrected after the PDA tests with helium, so that this error was no longer present in the PDA tests with air and carbon dioxide and in the validation tests of the FILM in section 4.5.

The mean standard deviation for air decreases from $\sigma(p_1(t = 0))$ = 2.14 mbar at the beginning of the discharge to $\sigma(p_1(t_{\mathrm{dis}}))$ = 0.63 mbar at the end of the discharge. According to the FILM, the influence of the standard deviation of the pressure on the air outflow velocity is thus $\pm$ 0.17 % at t = 0 s and $\pm$ 6.11 % at $t = t_{\mathrm{dis}}$.

The mean standard deviation for carbon dioxide increases from $\sigma(p_1(t = 0))$ = 0.30 mbar at the beginning of the discharge to $\sigma(p_1(t_{\mathrm{dis}}))$ = 0.69 mbar at the end of the discharge. According to the FILM, the influence of the standard deviation of the pressure on the carbon dioxide outflow velocity is thus $\pm$ 0.02 % at t = 0 s and $\pm$ 6.23 % at $t = t_{\mathrm{dis}}$.

The mean standard deviation for helium increases from $\sigma(p_1(t = 0))$ = 2.81 mbar at the beginning of the discharge to $\sigma(p_1(t_{\mathrm{dis}}))$ = 3.94 mbar at the end of the discharge. According to the FILM, the influence of the standard deviation of the pressure on the helium outflow velocity is thus $\pm$ 0.21 % at t = 0 s and $\pm$ 33.54 % at $t = t_{\mathrm{dis}}$. This deviation seems relatively large at first. However, if the helium discharge is limited to the inertia-dominated regime according to equation (2.10), then the influence drops to $\pm$ 6.37 % at t = 3.5 s. The reason for the greater deviations with helium is probably a greater variation in the environmental conditions. The helium tests had to be carried out over several months due to a helium shortage, which led to greater variations in the environmental conditions.
The internal vessel temperature T_1 is supposedly constant at first. It then monotonously drops, featuring an increasing temperature gradient that flattens out towards the end of the discharge for all three gases.

The temperature gradient is not the greatest at the beginning because the temperature sensor is not capable of correctly measuring steep temperature gradients. Although the temperature sensor (I-5) is not even the size of a pinhead, the response is delayed by the sensor's own thermal inertia. The measurement of steep temperature gradients is a general problem of the measurement technology that was used and could only be solved with a much greater experimental and financial effort. However, this was not pursued because the measurement of the vessel temperature is only subordinate.

The mean standard deviation of the internal vessel temperature at the beginning of the air discharge is $\sigma\big(T_1(t=0)\big) = 1.12$ K and $\sigma\big(T_1(t_{\mathrm{dis}})\big) = 1.00$ K at the end of the discharge. According to the FILM, the influence of the standard deviation of the internal vessel temperature on the outflow velocity is thus $\pm$ 0.19 % at t = 0 s and $\pm$ 0.14 % at $t = t_{\mathrm{dis}}$. The mean standard deviation of the internal vessel temperature at the beginning of the carbon dioxide discharge is $\sigma\big(T_1(t=0)\big) = 1.34$ K and $\sigma\big(T_1(t_{\mathrm{dis}})\big)$ = 1.19 K at the end of the discharge. According to the FILM, the influence of the standard deviation of the internal vessel temperature on the outflow velocity is thus $\pm$ 0.22 % at t = 0 s and $\pm$ 0.22 % at $t = t_{dis}$. The mean standard deviation of the internal vessel temperature at the beginning of the helium discharge is $\sigma\big(T_1(t=0)\big) = 2.12$ K and $\sigma\big(T_1(t_{\mathrm{dis}})\big) = 2.62$ K at the end of the discharge. According to the FILM, the influence of the standard deviation of the internal vessel temperature on the outflow velocity is thus $\pm$ 0.34 % at t = 0 s and $\pm$ 0.49 % at $t = t_{dis}$. Therefore, the influence of temperature differences on the discharge velocity is negligible. An overview of the effect of all of the above standard deviations is given in Table 5.4.

Table 5.4.: Overview of the impact of the standard deviation of the internal vessel pressure p_1 and temperature T_1 at the outflow velocity.

	Air	Carbon dioxide	Helium
$\sigma(p_1(t=0))$ / mbar	2.14	0.30	2.81
$\sigma(u_0(t=0))/\hat{u}_0$ / %	$\pm$ 0.17 %	$\pm$ 0.02 %	$\pm$ 0.21 %
$\sigma(p_1(t_{\mathrm{dis}}))$ / mbar	0.63	0.69	3.94
$\sigma(u_0(t_{\mathrm{dis}}))/\hat{u}_0$ / %	$\pm$ 6.11 %	$\pm$ 6.23 %	$\pm$ 33.54 %
$\sigma\big(T_1(t=0)\big)$ / K	1.12	1.34	2.12
$\sigma(u_0(t=0))/\hat{u}_0$ / %	$\pm$ 0.19 %	$\pm$ 0.22 %	$\pm$ 0.34 %
$\sigma\big(T_1(t_{\mathrm{dis}})\big)$ / K	1.00	1.19	2.62
$\sigma(u_0(t_{\mathrm{dis}}))/\hat{u}_0$ / %	$\pm$ 0.14 %	$\pm$ 0.22 %	$\pm$ 0.49 %

The ambient temperature T_∞ remains almonst constant during the discharge. The large standard deviations are caused by the ambient temperature increase during the course of an experimental day, which happened because the laboratory does not have a temperature control system. However, this influence is negligible during a single discharge experiment because the ambient temperature fluctuates less than 0.04 °C during the discharge. The actual temperature change should be even smaller because 0.04 °C

corresponds to the resolution of the complete temperature sensing system. When comparing the internal vessel temperature T_1 with the ambient temperature T_∞, it can be observed that the initial internal vessel temperature $T_1(t = 0)$ is greater and becomes smaller than the ambient temperature during the discharge. The reason for this is that the gas in the vessel heats up during filling due to compression. Cooling down to almost ambient temperature takes about 15 min per discharge, which was not waited for because the difference quotient $\Delta T/\Delta t \approx 5 \cdot 10^{-3}$ K/s is three orders of magnitude smaller than the difference quotient during the discharge $\Delta T/\Delta t \approx 1$ K/s. Overall, this shows that the influence of temperature and pressure deviations is relatively small over the great number of experiments and there is a high degree of reproducibility.

5.5. Results of the velocity field

In this section, the results from the experimental investigations on transient free jet propagation are presented and explained. The profile of the current mean axial velocity $\hat{u}_{cl}(x,t)$ on the centre line is first considered. Here, both different times during the outflow and averaged profiles are considered. Furthermore, a statistical analysis of the influence of the Reynolds number on the decay constant is performed. The radial profiles of the current mean axial velocity $\hat{u}(x,z,t)$ at different axial distances x are then considered. Potential sources of error due to buoyancy effects and their effect on measurements are also discussed. Finally, a statistical analysis of the Reynolds number influence on the spreading rate is performed.

5.5.1. Axial velocity decay

Starting with the evaluation of the axial velocity profile. In Figure 5.5 the current mean velocity $\hat{u}_{cl}(x,t)$ is scaled with the current mean exit velocity $\hat{u}_0(t)$ and plotted against the axial distance x scaled with the effective diameter d_e for the particle class d_{pc} = 6.5 µm. The density ratios of $R_\varrho \approx 1$ for the air jet, $R_\varrho \approx 1.52$ for the carbon dioxide jet and $R_\varrho \approx 0.14$ for the helium jet are determined for t = 0 s. The material data used are from Linstrom (1997). The cooling due to the isentropic expansion and consequently time-dependent densities and viscosities at the outlet are considered. Table 5.5 summarises the values at the pipe exit at the beginning t = 0 s and at the end of the discharge for the three gases. For further evaluation, the values at the pipe exit were recalculated for each time step evaluated. Several discrete points in time during the discharge process are considered to analyse the transient flow character.

Table 5.5.: Overview of the injection densities ϱ_{in}, effective pipe diameters d_e, Froude numbers Fr and buoyancy numbers X_F at the beginning $t = 0$, at the end of the inertia-dominant regime t_{inertia} and the end of the discharge t_{dis}.

	Air		Carbon dioxide			Helium		
t / s	0	t_{dis} = 13.66	0	t_{dis} = 17.55	t_{inertia} = 16 s	0	t_{dis} = 5.33	t_{inertia}= 3.5
ϱ_{in} /kg m^{-3}	1.167	1.226	1.808	1.881	1.879	0.163	0.177	0.173
μ_{in} / µPa·s	18.55	17.84	14.92	14.37	14.39	19.87	18.73	19.02
d_e / mm	24.8	25.4	30.9	31.5	31.5	9.2	9.7	9.6
Fr / -	$1.79{\cdot}10^{7}$	$6.62{\cdot}10^{4}$	$4.82{\cdot}10^{5}$	$4.85{\cdot}10^{4}$	$1.28{\cdot}10^{4}$	$2.49{\cdot}10^{5}$	$1.39{\cdot}10^{3}$	$3.60{\cdot}10^{4}$
X_F / -	0.014	0.23	0.078	0.767	0.473	0.197	2.588	0.511

Beside the experimental data (blue and orange symbols), the model according to Chen and Rodi (1980) (red line) is shown. For air and carbon dioxide a virtual jet origin of $x_0 = 0$ was used in the model of Chen and Rodi (1980), and $x_0 = 3.8\ d$ was used for helium. The orange symbols mark the area in which the free jets lie in the buoyancy-affected regime according to equation (2.10). For carbon dioxide, the buoyancy-affected regime was defined from an exit velocity less than $\hat{u}_0 < 33$ m/s and for helium from an exit velocity of less than $\hat{u}_0 < 226$ m/s. This point was reached after $t > 16$ s for the carbon dioxide discharge and after $t > 3.75$ s for the helium discharge. For air, the buoyancy-affected regime would start at an exit velocity of less than $\hat{u}_0 < 9$ m/s. This is below the velocity $\hat{u}_0 < 25$ m/s at the defined discharge duration of $t_{\mathrm{dis}} = 13.65$ s. Therefore, buoyancy effects on the air jet are negligible and are not considered further in the evaluation.

In accordance with the theory, the velocity is initially almost constant in a core region $x_c = 5\ d$ for air, $x_c = 6.2\ d$ for carbon dioxide and $x_c = 4.2\ d$ for helium and then decreases hyperbolically. This fits with the results of Rajaratnam (1976) for steady free jets. For all gases, there is a good agreement with the model of Chen and Rodi (1980) using a decay constant $K_{1,u} = 6.2$, especially in the self-similar jet region. The mean deviation from the model according to Chen and Rodi (1980) in the self-similar region is 1.32 % for air, -3.16 % for carbon dioxide and 1.13 % for helium. For the air jet, greater deviations are observed in some cases towards the end of the discharge at $t = 13$ s and $t = 14$ s. One reason for this is the decrease of the data rate towards the end of the discharge, which weakens the statistical reliability for the determination of the current mean velocity. This problem certainly also occurs with steady-state flows, but can be solved simply by extending the measurement period. However, this is not possible within a transient vessel discharge. Assuming an ergodic process, this problem could be solved by generating the measured values of a location by multiple outflow tests. However, this was not carried out due to the very time-consuming process. The single data point at $t = 14$ s at the position $x/d_e = 16.2$ in Figure 5.5 (a) is explained by the fact that the vessel was closed too early in this test. Therefore, this value is not considered for further evaluation.

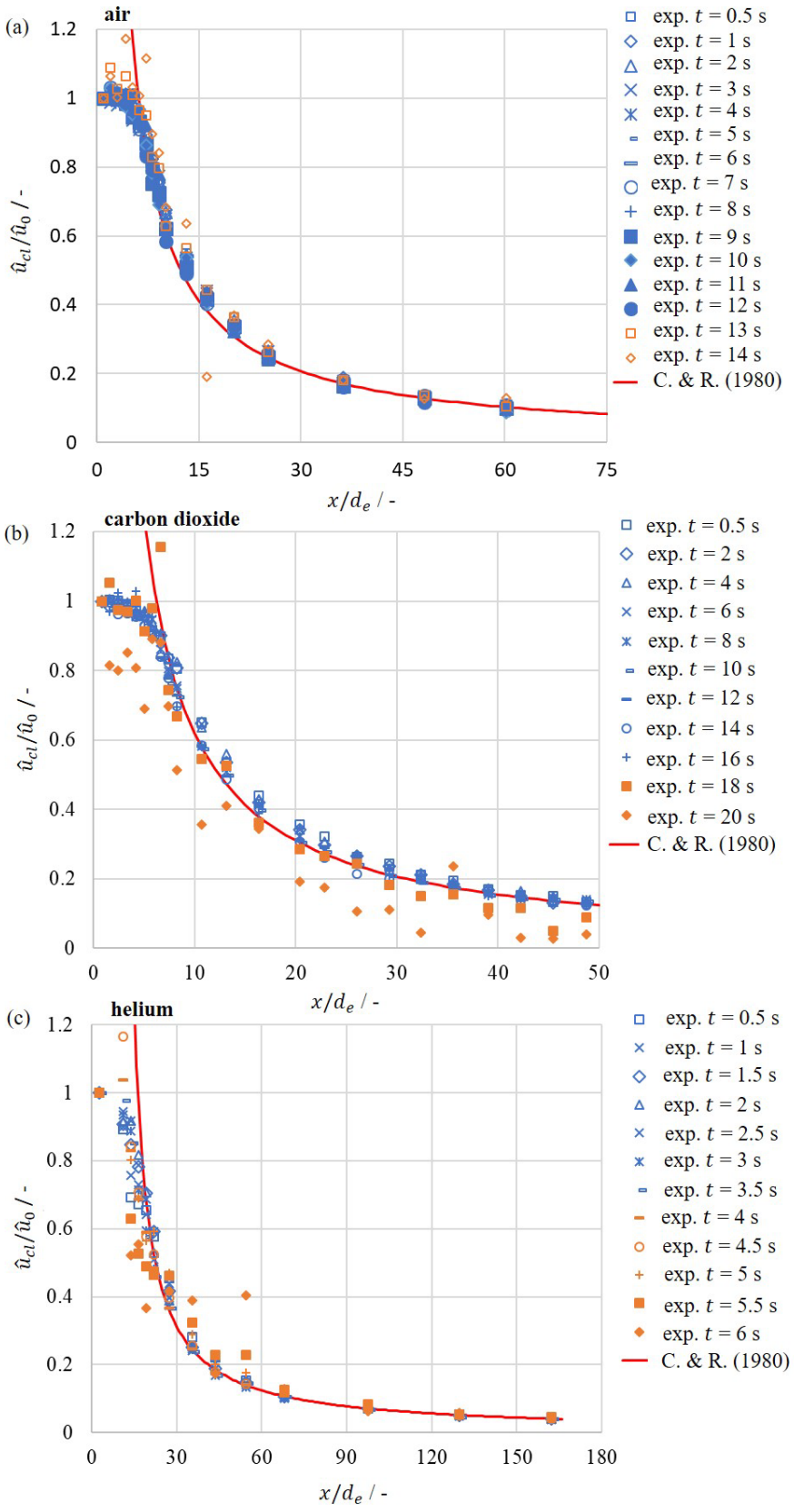

Figure 5.5.: Scaled current mean axial velocity $\hat{u}_{cl}/\hat{u}_0$ along the jet axis against scaled axial distance x/d_e for the particle class d_{pc} = 6.5 µm: (a) air jet, (b) carbon dioxide jet, and (c) helium jet. Subdivided into the inertia-dominated regime (blue) and buoyancy-affected regime (orange). Modified from PPA1.

The influence of buoyancy is shown in particular on the carbon dioxide jet because the velocity curves drop clearly for later discharge times. This can be referred to the apparent-centre-line effect, which will be explained in the context of Figure 5.9. Thus, the centre line shifts due to the sinking of the denser carbon dioxide. However, the measurement continues to be taken on the x-axis (apparent centre line); a smaller axial velocity is measured. In the case of helium, the buoyancy influence on the axial velocity profile cannot be recognised well in Figure 5.5 (c).

Overall, the axial velocity profiles $\hat{u}(x,t)$ for the different points in time do not show major deviations. Thus, it appears possible to scale a transient free jet with the time-dependent current mean exit velocity $\hat{u}_0(t)$ in a similar way as a stationary jet leading to a self-similar representation. This idea is to be investigated in more detail by averaging over the outflow duration for different particle sizes. As mentioned before, the additional measurement of the particle size with the PDA leads to a further validation. To assess this, the scaled velocity $\hat{u}_{cl}(x,t)/\hat{u}_0(t)$ averaged over several discrete points in time during the discharge is plotted against the scaled axial distance x/d_e for different particle classes in Figure 5.6. For simplification, the averaging over the scaled current mean velocity $\hat{u}_{cl}/\hat{u}_0$ during the discharge is referred to as discharge average velocity $\overline{\hat{u}_{cl}/\hat{u}_0}$, i.e.

$$\overline{\hat{u}_{cl}(x)/\hat{u}_0} = \frac{1}{N}\sum_{t=0.5\,s}^{t_{\mathrm{inertia}}} \hat{u}_{cl}(x,t)/\hat{u}_0(t). \tag{5.5}$$

The inertia-dominated discharge duration t_{inertia} was divided into N equally-distributed discrete points in time, with N = 15 for air, N = 17 for carbon dioxide and N = 13 for helium. However, the average is not taken over the entire outflow duration for carbon dioxide and helium but only for the duration that is inertia-dominated t_{inertia}, according to equation (2.10). For carbon dioxide this is the range $t \leq 16$ s and for helium $t \leq 3.5$ s. The discharge average velocities are plotted in Figure 5.6 for the four smallest particle classes d_{pc} = 0.5 µm (blue squares), d_{pc} = 2.5 µm (orange diamonds), d_{pc} = 6.5 µm (turquoise traingles) and d_{pc} = 11.5 µm (purple crosses).

For all gases, there is a good agreement between the four different particle classes. Quantitatively, this is confirmed by the small mean relative standard deviations of the discharge average velocity profiles σ_{rel} = 0.95 % for air, σ_{rel} = 0.74 % for carbon dioxide and σ_{rel} = 0.65 % for helium among the four different particle classes. The standard deviations for the individual particle classes tend to be greater for positions close to the pipe exit. This is because the velocity gradient is greatest after the core region and variations become more visible there. The experimental data of air are compared with data from transient numerical simulations of Abraham (1996) (grey pluses), the theoretical model according to Chen and Rodi (1980) (C. & R. 1980 red line) and the experimental data of Wygnanski and Fiedler (1969) (W. & F. 1969 green circles) for a stationary air jet. The model by Chen and Rodi (1980) is actually only valid in the similarity region $x/d > 25$ and the velocity has the asymptote $\overline{\hat{u}_{cl}(x)/\hat{u}_0} \to \infty$ for the axial distance $x/d \to 0$. In particular, in the self-similar region the differences between the axial

velocity profile $\overline{\hat{u}_{cl}(x)/\hat{u}_0}$ according to the model of Chen and Rodi (1980) and our experimental data are small with a mean relative deviation of 1.31 % for air, 3.05 % for carbon dioxide and 2.35 % for helium. Compared to a stationary free jet, the core region is not sharply defined. Thus, the axial velocity $\overline{\hat{u}_{cl}(x)/\hat{u}_0}$ gradually decreases with the axial distance x, which can also be observed in the data of Abraham (1996). So the core length x_c of Abraham (1996) is similarly long but the velocity decay appears faster, especially in the transition region of the free jet. This is not surprising because according to Pope (1978) the k-ε turbulence model which was used by Abraham (1996) is known to have problems in the calculation of round free jets. Pope (1978) explains that the k-ε turbulence model is not capable of accurately representing recirculation flows because they occur on the basis of eddies in free jets. This leads to a greater velocity decay, corresponding to a smaller decay constant $K_{1,u}$. There is a great agreement between the present experimental data for air and those of Wygnanski and Fiedler (1969) for a stationary air jet. This supports the idea that a transient free jet can be considered as a stationary free jet by scaling it with the current mean outlet velocity $\hat{u}_0(t)$. This leads to a self-similar behaviour of the transient free jet. The quantitative comparison is further made based on the determination of the decay constant $K_{1,u}$.

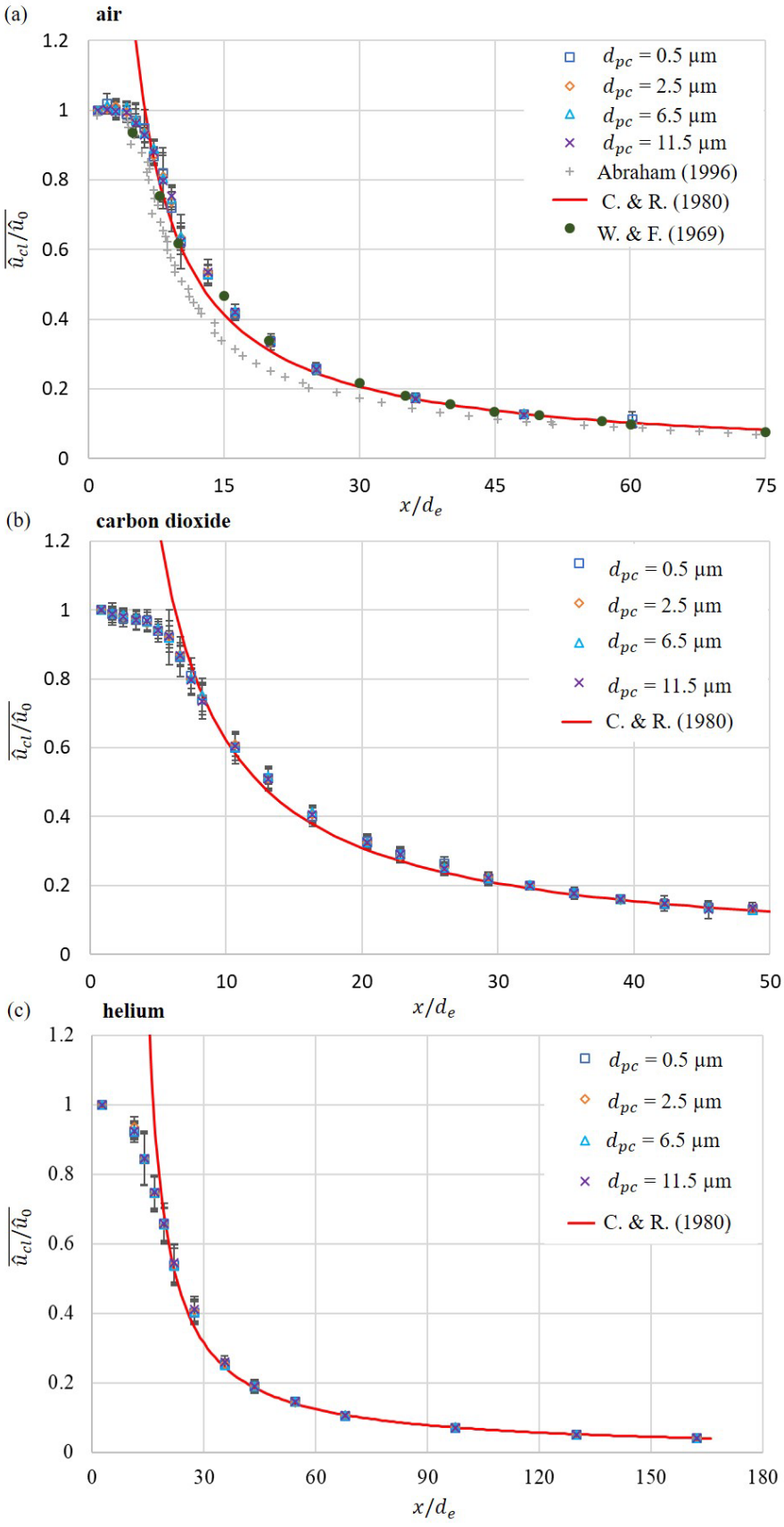

Figure 5.6.: Self-similar behaviour for the axial discharge average velocity $\overline{\hat{u}_{cl}/\hat{u}_0}$ against scaled axial distance for several particle classes: (a) air jet, (b) carbon dioxide jet, and (c) helium jet. Error bars indicate the standard deviation. Modified from PPA1.

To determine the decay constant $K_{1,u}$ and illustrate the hyperbolic character of the axial velocity profile $\overline{\hat{u}_{cl}(x)/\hat{u}_0}$, the axial velocity profile is plotted in the inverse form $\overline{\hat{u}_o/\hat{u}_{cl}(x)}$ against the scaled axial distance x/d_e according to equation (2.3) in Figure 5.7. As before, the four smallest particle classes d_{pc} = 0.5 µm (blue squares), d_{pc} = 2.5 µm (orange diamonds), d_{pc} = 6.5 µm (turquoise traingles) and d_{pc} = 11.5 µm (purple crosses) are considered. Furthermore, the experimental data are again compared with the data of Abraham (1996) (grey pluses), the theoretical model according to Chen and Rodi (1980) (C. & R. 1980 red line) and experimental data of Wygnanski and Fiedler (1969) (W. & F. 1969 green circles). The profiles of the particle classes d_{pc} = 0.5 µm and d_{pc} = 2.5 µm overlap almost perfectly and have a great agreement with the model of Chen and Rodi (1980). Apart from the measuring point for air at x/d_e = 60.2 and carbon dioxide at x/d_e = 48.58 for the particle class d_{pc} = 11.5 µm, there is a high degree of agreement between the particle classes.

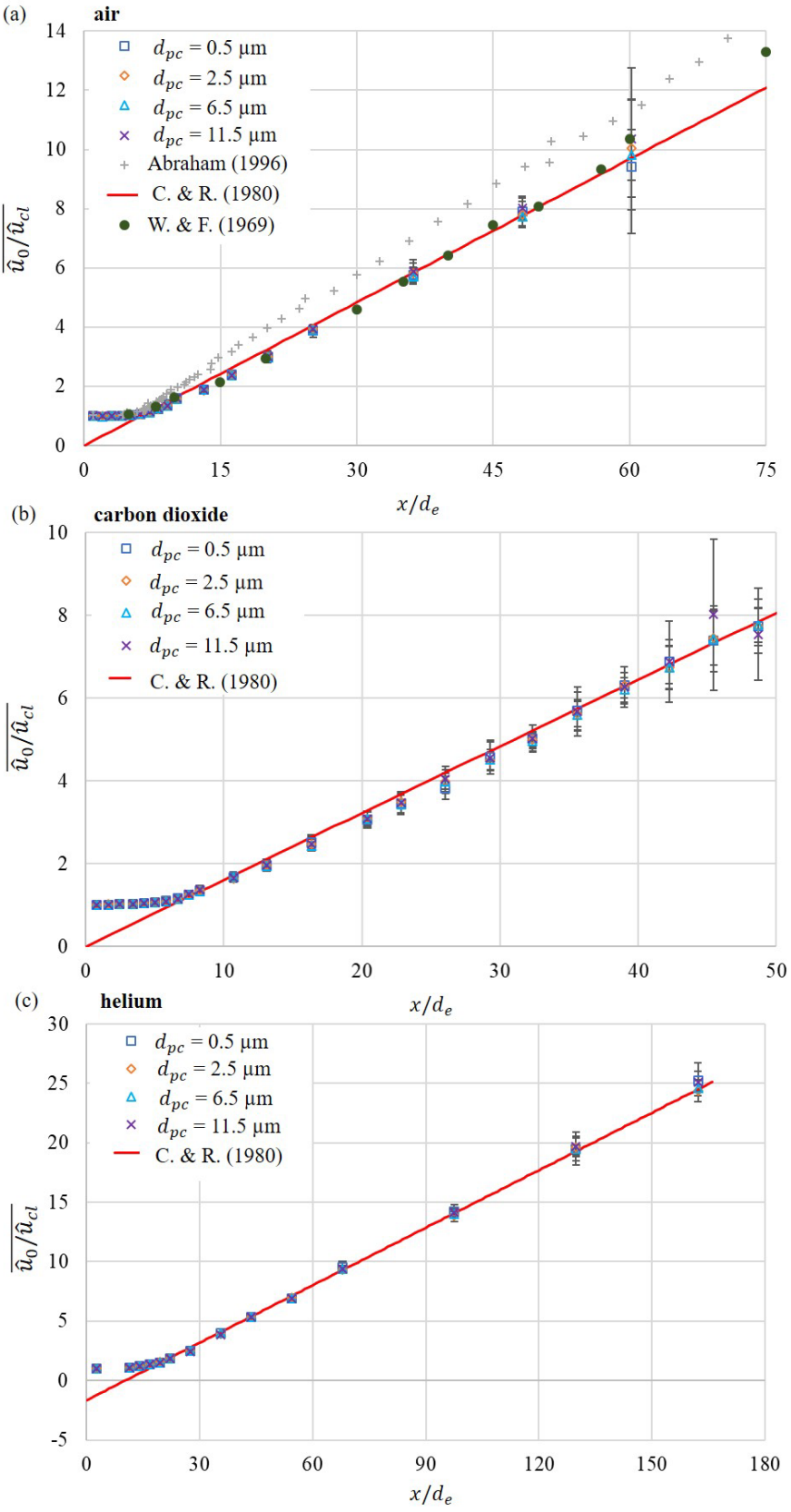

Figure 5.7.: Inverse discharge average velocity $\overline{\hat{u}_0/\hat{u}_{cl}}$ against scaled axial distance x/d_e for several particle classes d_{pc}: (a) air jet, (b) carbon dioxide jet and (c) helium jet. Error bars indicate the standard deviation. Modified from PPA1.

The decay constant $K_{1,u}$ is determined within the self-similar range x/d > 25 using equation (2.3). The furthest position at x/d = 60.2 is not included in the determination of the decay constant $K_{1,u}$ due to the great standard deviation, which is attributed to a small data rate. The mean measured particle number for the three gases at the position x/d = 60.2 is 2 500. This means that about four times less particles were measured there than (for example) at the location x/d = 48.2 and almost 20 times less particles than at x/d = 1. The mean decay constant for the transient air jet is $K_{1,u}$ = 5.87, for the carbon dioxide jet $K_{1,u}$ = 5.80 and for the helium jet $K_{1,u}$ = 5.98. The decay constant of the carbon dioxide jet is therefore -1.19 % smaller and that of the helium jet +1.87 % greater than the decay constant of the air jet. Furthermore, the "null hypothesis" is defined as the gas has no effect on the decay constant $K_{1,u}$. Since the p-value > 0.61 is greater than the significance level of α = 0.05, the "null hypothesis" cannot be rejected. This means that no significant correlation between the decay constant and the gas can be detected. This does not directly mean that the gas cannot have an influence on the decay constant, it may also be that the available data are not sufficient for a statement. This may be the case with a variation of three gases only. However, the number of non-toxic and non-flammable gases is limited, so further variation is difficult from a safety point of view. An overview on all decay constants is given in Table 5.6.

The approach of an effective diameter according to Thring and Newby (1953) to capture the density effect on axial velocity decay seems to also be validated for transient free jets. Furthermore, the definition of a universal decay constant $K_{1,u}$ = 5.90 seems suitable.

Table 5.6.: Overview of the decay constant $K_{1,u}$, virtual origin x_0 and coefficients of determination R^2 for transient air, carbon dioxide and helium jet based on the regression lines for different particle classes. Modified from PPA1.

	Air			Carbon dioxide			Helium		
d_{pc} in µm	$K_{1,u}$	x_0/d_e	R^2	$K_{1,u}$	x_0/d_e	R^2	$K_{1,u}$	x_0/d_e	R^2
0.5	6.109	1.446	0.9978	5.787	1.731	0.9720	5.887	11.574	0.9967
2.5	5.777	2.558	0.9996	5.801	1.655	0.9853	6.035	10.981	0.9982
6.5	5.921	2.247	0.9998	5.817	1.815	0.9871	6.007	11.112	0.9978
11.5	5.659	2.844	0.9997	6.003	1.508	0.9145	5.894	11.842	0.9950
mean	5.866	2.274	0.9992	5.802	1.734	0.9815	5.977	11.222	0.9976
standard deviation	0.194	0.603	0.0010	0.015	0.080	0.0083	0.079	0.312	0.0007

Another way to check the reproducibility is to consider the so-called random vessel effect. Therefore, the inverse velocity profile, as shown in Figure 5.7, was modelled with a mixed linear regression model according to Fahrmeir et al. (2016). The influence of the test identification number on the axial velocity profile is to be investigated, with the result that the variance contribution of the random vessel effect is only 0.0016 % for air, 1.35 % for carbon dioxide and 0.76 % for helium. The remaining part of the variance is due to fixed effects such as temperature and pressure variations, which also occur within a discharge experiment. Furthermore, the contribution of the random vessel effect on the residual variance

is 1.19 % for air, 1.90 % for carbon dioxide and 0.35 % for helium. Therefore, no statistically significant effect (p-value = 1) of random effects is found. This ensures an overall high level of reproducibility.

5.5.2. Reynolds number dependency of decay constant

One of the open questions in the literature is the influence of the Reynolds number on the decay constant $K_{1,u}$. To investigate this question further, Figure 5.8 plots the decay constant $K_{1,u}$ for different points in time, which results in a variation of the Reynolds number Re due to different current mean outlet velocities $\hat{u}_0(t)$. The decay constants $K_{1,u}$ of the four smallest particle classes d_{pc} = 0.5 µm (blue squares), d_{pc} = 2.5 µm (orange diamonds), d_{pc} = 6.5 µm (turquoise traingles) and d_{pc} = 11.5 µm (purple crosses) are shown. Since buoyancy effects lead to apparent correlations between the decay constant and Reynolds number, only the inertia-dominated regime $\mathrm{X}_F < 0.5$ is initially considered. According to equation (2.11), the inertia-dominated regime for air extends over the entire outflow duration. For the helium chart in Figure 5.8 (c), the region from which the outlet velocity was extrapolated is marked due to exceeding the maximum measurable velocity, and is thus scaled with this extrapolated velocity, as shown in Figure 5.1.

The decay constant $K_{1,u}$ depending on the Reynolds number Re is modelled with a linear regression (red line), i.e., by

$$K_{1,u} = c_{1,a} \cdot \mathrm{Re} + c_{1,b}. \tag{5.6}$$

Thus, a coefficient of the Reynolds number of $c_{1,a}$ = 0 is defined as the null hypothesis, which corresponds to the case where the Reynolds number has no influence on the decay constant. As the alternative hypothesis, tests whether coefficient $c_{1,a}$ is significantly different from 0. If the calculated significance p-value for the coefficient is smaller than the selected significance level of α = 0.05, then the null hypothesis is rejected in favour of the alternative hypothesis. (Fahrmeir et al., 2016)

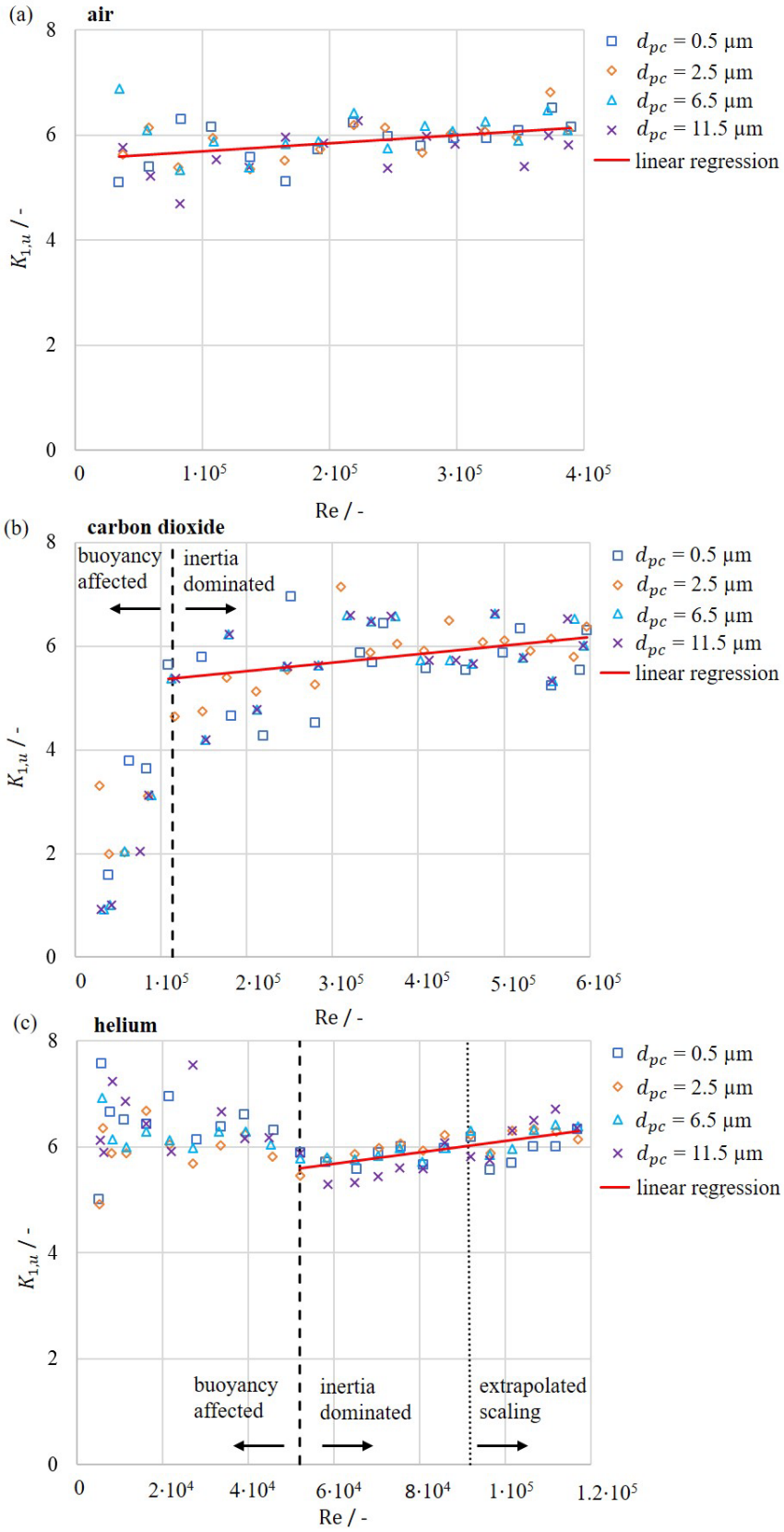

Figure 5.8.: Decay constant $K_{1,u}$ against Reynolds number Re: (a) air jet, (b) carbon dioxide jet and (c) helium jet. Modified from PPA1.

In Table 5.7, the coefficients $c_{1,a}$ and $c_{1,b}$ are summarised as well as the significance p-values. Due to the small significance p-values < $1.703 \cdot 10^{-4}$ for the coefficient $c_{1,a}$, a statistically significant dependence of the decay constant $K_{1,u}$ on the Reynolds number Re is confirmed in the range $4 \cdot 10^4 \leq \mathrm{Re} \leq 6 \cdot 10^6$. It could be mistakenly understood at this point that a slope of $c_{1,a} \approx 10^{-6}$ is quasi-zero, thus confirming the null hypothesis. However, a slope of $c_{1,a} = 10^{-6}$ at a Reynolds number of $\mathrm{Re} \approx 10^5$ means that the influence of the Reynolds number Re is again of a similar magnitude as the decay constant $K_{1,u}$.

Table 5.7.: Summary of the coefficients $c_{1,a}$ and $c_{1,b}$ and the corresponding significance p-values. Modified from PPA1.

	Air	Carbon dioxide	Helium
$c_{1,a}$	$1.51 \cdot 10^{-6}$	$2.03 \cdot 10^{-6}$	$1.07 \cdot 10^{-6}$
p-value$(c_{1,a})$	$1.703 \cdot 10^{-4}$	$2.358 \cdot 10^{-4}$	$1.937 \cdot 10^{-8}$
$c_{1,b}$	5.54	5.18	5.04
p-value$(c_{1,b})$	$< 10^{-16}$	$< 10^{-16}$	$< 10^{-16}$

For all three gases, the decay constant $K_{1,u}$ increases slightly in the inertia-dominated regime with increasing Reynolds number. Since the Reynolds number describes the ratio of inertial and frictional forces, it seems plausible that a free jet with a greater Reynolds number, and thus greater inertia, experiences a slower velocity decay. This correlation fits the observations from large-eddy simulation by Bogey and Bailly (2006), and Bonelli et al. (2021), as well as experimental results by Borée et al. (1996). Pope (2015) assumed that there was no significant influence of the Reynolds number on the decay constant and attributed the deviations to measurement inaccuracies. This statement can be rejected at this point. However, it must be admitted that the influence of the Reynolds number is small in the investigated range of Reynolds numbers. This makes it understandable that some authors attribute the deviations of the decay constant to measurement inaccuracies. However, based on the statistical evaluation, this assumption can be rejected because the deviations are not random but statistically significant. Since the influence of the Reynolds number Re on the decay constant $K_{1,u}$ is small, and probably of no relevance, for most technical applications the previously defined quasi-self-similarity with a mean decay constant of $K_{1,u} = 5.90$ seems to be acceptable.

The carbon dioxide and helium jet differ in the buoyancy-affected regime. Thus, the decay constant decreases with decreasing Reynolds number for the carbon dioxide jet and increases with decreasing Reynolds number for the helium jet. To understand the different behaviour of carbon dioxide and helium, the propagation of buoyancy-affected free jets will be considered in more detail in Figure 5.9 for free jets with a density ratio of $R_\varrho < 1$ like helium and for a density ratio $R_\varrho > 1$ like carbon dioxide. The jet's axis is bent in the case of non-density-neutral horizontal free jets in the buoyancy-affected regime, so that the maximum velocity is no longer on the x-axis with $y, z = 0$. If, as in this case, the velocity continues to be measured on the x-axis, then a faster velocity drop is detected, which results in a smaller

decay constant $K_{1,u}$. This effect will be called the apparent-centre-line effect. Thus, the behaviour of the buoyancy-affected helium jet does not correspond to expectations of the apparent centre line.

To understand different behaviour, there must be a second effect besides the apparent-centre-line effect that affects the velocity field. Certainly, the buoyancy of the less dense helium compared to the ambient air shifts the jet axis in the positive z-direction, which is why the maximum velocity is no longer present on the x-axis. However, according to the approach of Thring and Newby (1953), the density ratio is decisive for the velocity decay in a free jet. Thus, in the case of the helium jet, a relatively denser ambient gas (air) is sucked into the free jet, and in the case of carbon dioxide jet a relatively less dense ambient gas (air) is sucked into the free jet. Therefore, in the case of the helium jet, if jet regions with a higher density are shifted to the x-axis due to buoyancy, then these regions reduce velocity more slowly because they have a higher inertia due to the higher density. This effect will be further called the density-entrainment effect.

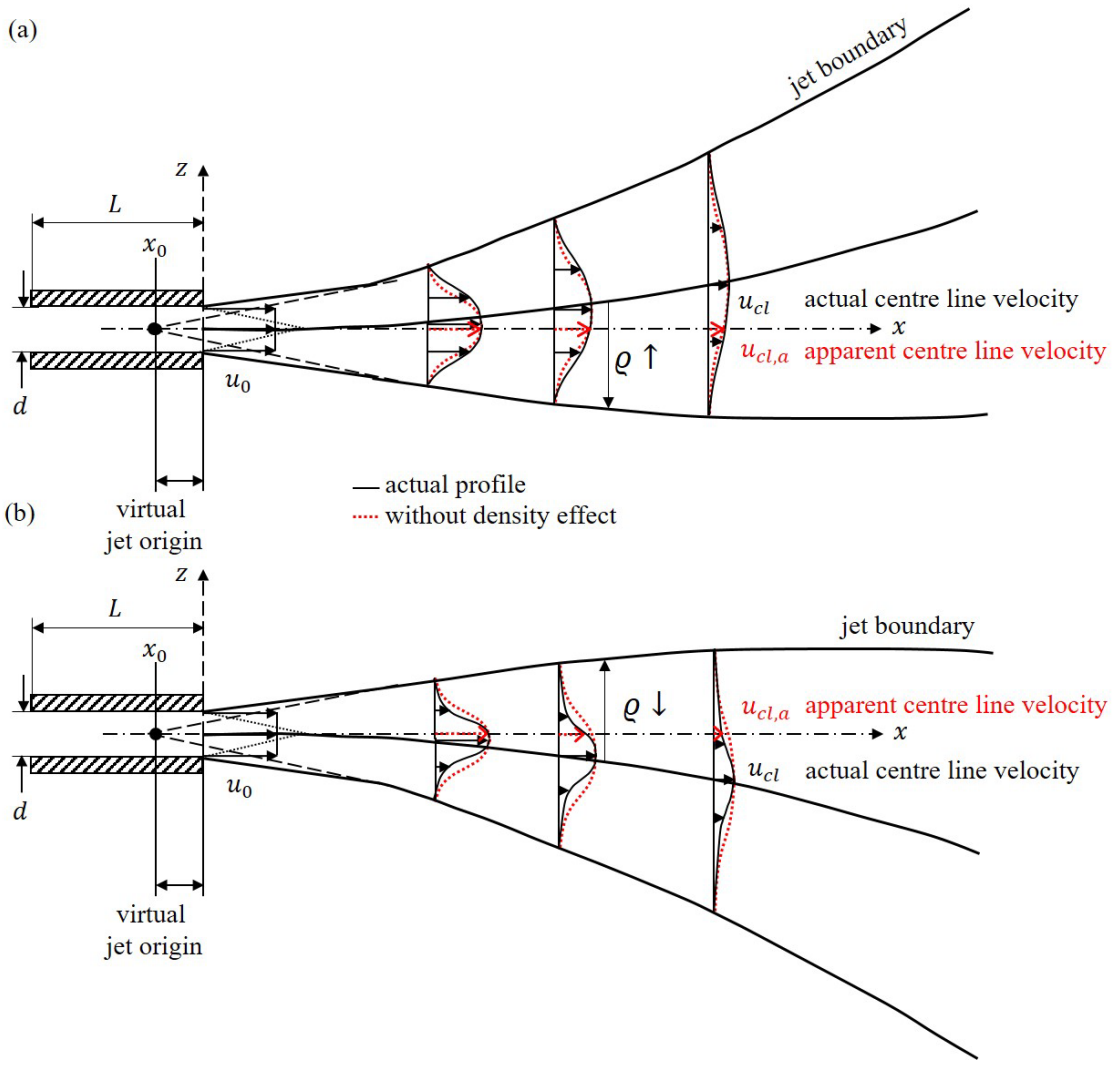

Figure 5.9.: Buoyancy effects on the propagation behaviour of horizontal free jets. (a) free jet with a density ratio $R_\varrho < 1$ and (b) free jet with a density ratio $R_\varrho > 1$.

A slower velocity decay results in a larger decay constant $K_{1,u}$, this behaviour can be observed in Figure 5.8. The influence of a different density in the free jet and the resulting different rate of velocity decay is also present in the carbon dioxide jet. The carbon dioxide jet mixes with the less dense ambient air. When these regions are shifted to the x-axis due to buoyancy, a faster velocity decay is detected. Since the apparent-centre-line effect with the shift of the velocity profile and the density-entrainment effect in the carbon dioxide jet have the same influence on the free jet, these effects cannot be observed separately from each other. The situation is different with the helium free jet, where the apparent-centre-line effect leads to a faster decrease of the velocity on the x-axis and the density-entrainment effect to a slower decrease of the velocity. However, according to Figure 5.8 the density-entrainment effect predominates for the helium jet, and thus causes an increase of the decay constant for smaller Reynolds numbers. In summary, the decay constant increases again in the buoyancy-affected regime for decreasing Reynolds number for horizontal free jets with a density ratio of $R_\varrho < 1$. Conversely, the decay constant for free

jets with a density ratio $R_\varrho > 1$ in the buoyancy-affected regime decreases as the Reynolds number decreases.

5.5.3. Radial spreading behaviour

The radial velocity profiles will now be investigated. The radial velocity profiles of the axial velocity component $\hat{u}(x, z, t)$ are shown in Figure 5.10, Figure 5.11 and Figure 5.12 for different axial distances x. The current mean velocity $\hat{u}(x, y = 0, z, t)$ is scaled with the current mean centre-line velocity $\hat{u}_{cl}(x, t)$ and averaged over the discharge duration that is inertia dominated. This leads to a period of time of $t \leq 16$ s for the carbon dioxide jet and for the helium jet to $t \leq 3.5$ s (cf. Table 5.5). The radial distances z are scaled with the corresponding axial distances x of the measuring plane. To determine the spreading rate $K_{2,u}$, five points are considered sufficient for each axial distance x to determine the profile because it has been confirmed in a large number of investigations that the radial velocity profile of a free jet can be approximated with a Gaussian profile (cf. equation (2.4)) (Ball et al., 2012). Therefore, the Gaussian profile no longer needs to be confirmed at this point. There is a transition from a turbulent pipe flow velocity profile at the pipe exit x = 0.025 m to a Gaussian profile for further axial distances. The velocity profiles at the pipe exit ((a) in Figure 5.10, Figure 5.11 and Figure 5.12) are modelled with a power-law approximation using an exponent of 1/7, i.e.

$$\overline{\hat{u}(z)/\hat{u}_{cl}} = \left(1 - \frac{2z}{d}\right)^{1/7}, \tag{5.7}$$

according to Zierep (2018) and Oertel (2012). This corresponds to the assumption that the same flow conditions exist in the core region of a free jet as at the pipe outlet. It must be mentioned here that the power law approach is not valid on the wall because it leads to infinite gradients. Furthermore, the power-law approach does not have a gradient of zero on the centre line and is not valid there. Nevertheless, this approach provides a great deal of agreement with the experimental data for most parts of the pipe cross section.

Especially for the positions x = 0.630 m and x = 0.905 m, a great correspondence to the model is present. Overall, there is a good agreement between the velocities in the positive and negative z-directions. This indicates that the free jet in the previously defined inertia-dominated regime behaves not only axisymmetrically but is also rotationally symmetric. This can be understood as a validation of the measurement results and shows that no noticeable buoyancy effects occur. Thus, buoyancy effects hardly bias the results on the dependence of the propagation.

Since the scaling of the velocity is always carried out with the centre-line velocity, the scaled velocity on the centre line must always be $\overline{\hat{u}(z = 0)/\hat{u}_{cl}}$ = 1, and therefore has a standard deviation of σ = 0.

Hence, the scaled velocities on the centre line do not have an error indicator. The standard deviations σ increase with increasing axial distance. Due to the jet's expansion, the tracer density is reduced, and thus the data rate is also reduced. As a result, it was not possible to measure further outwards in a radial direction. Due to the great standard deviations at the most distant axial measurement position x = 1.505 m, these data are not taken into account when determining the spreading rate $K_{2,u}$ for all three gases.

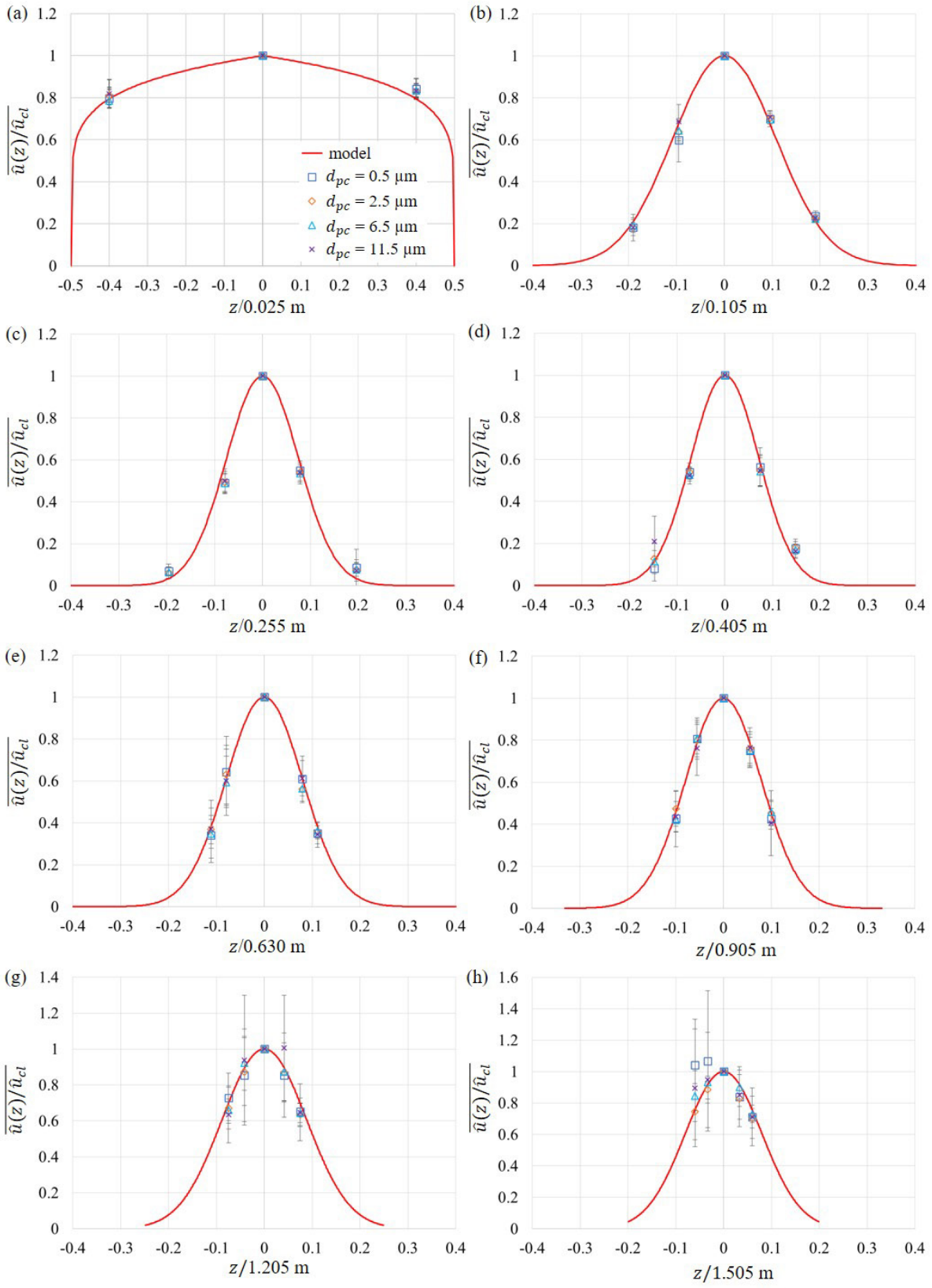

Figure 5.10.: Discharge average radial velocity profile $\overline{\hat{u}(z, y = 0)/\hat{u}_{cl}}$ against the radial distance z, scaled with the axial distance x for an air jet. Error bars indicate the standard deviation: (a) power-law model, (b) to (h) Gauss model. Modified from PPA1.

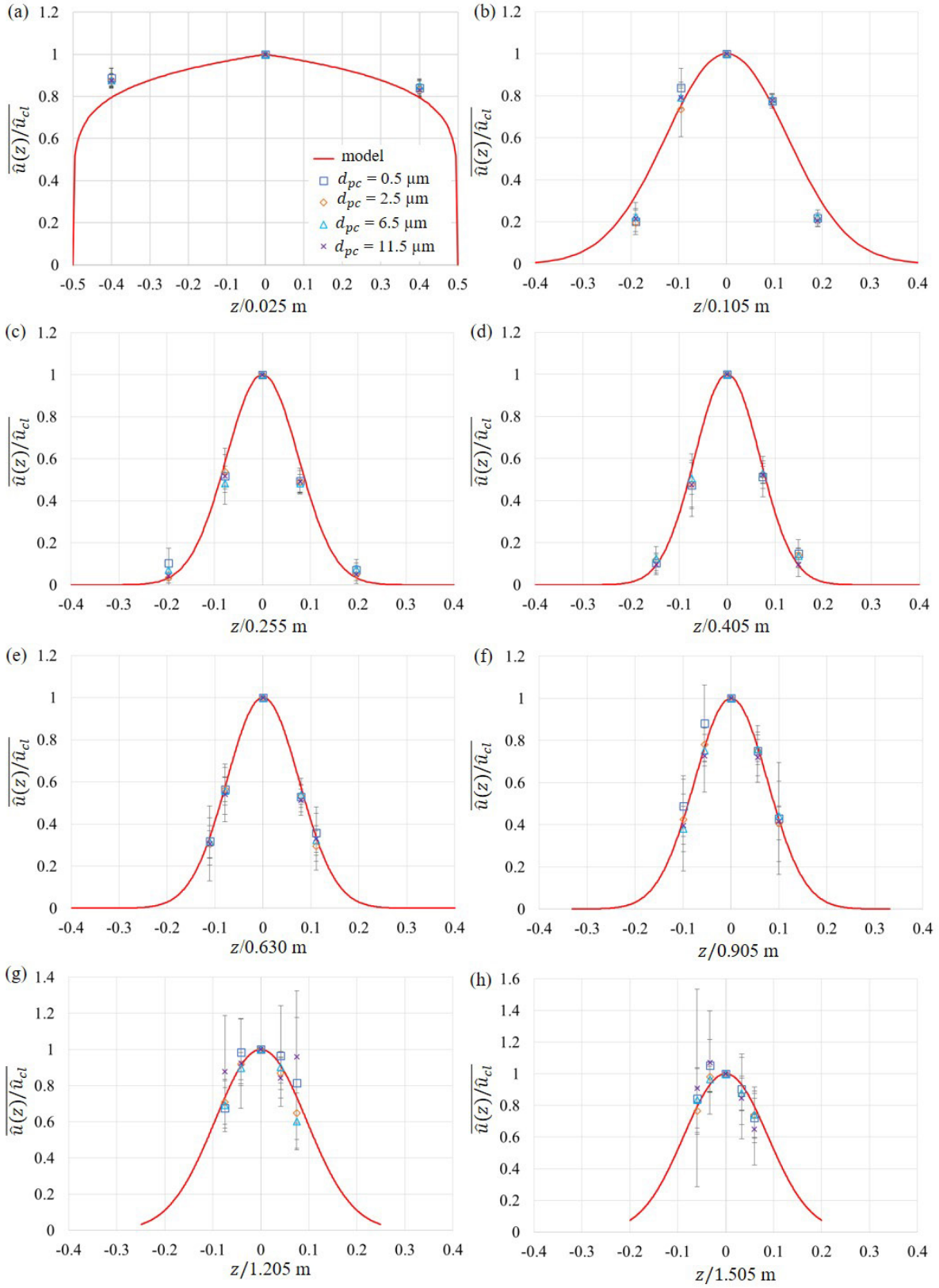

Figure 5.11.: Discharge average radial velocity profile $\overline{\hat{u}(z, y = 0)/\hat{u}_{cl}}$ against the radial distance z, scaled with the axial distance x for a carbon dioxide jet. Error bars indicate the standard deviation: (a) power-law model, (b) to (h) Gauss model.

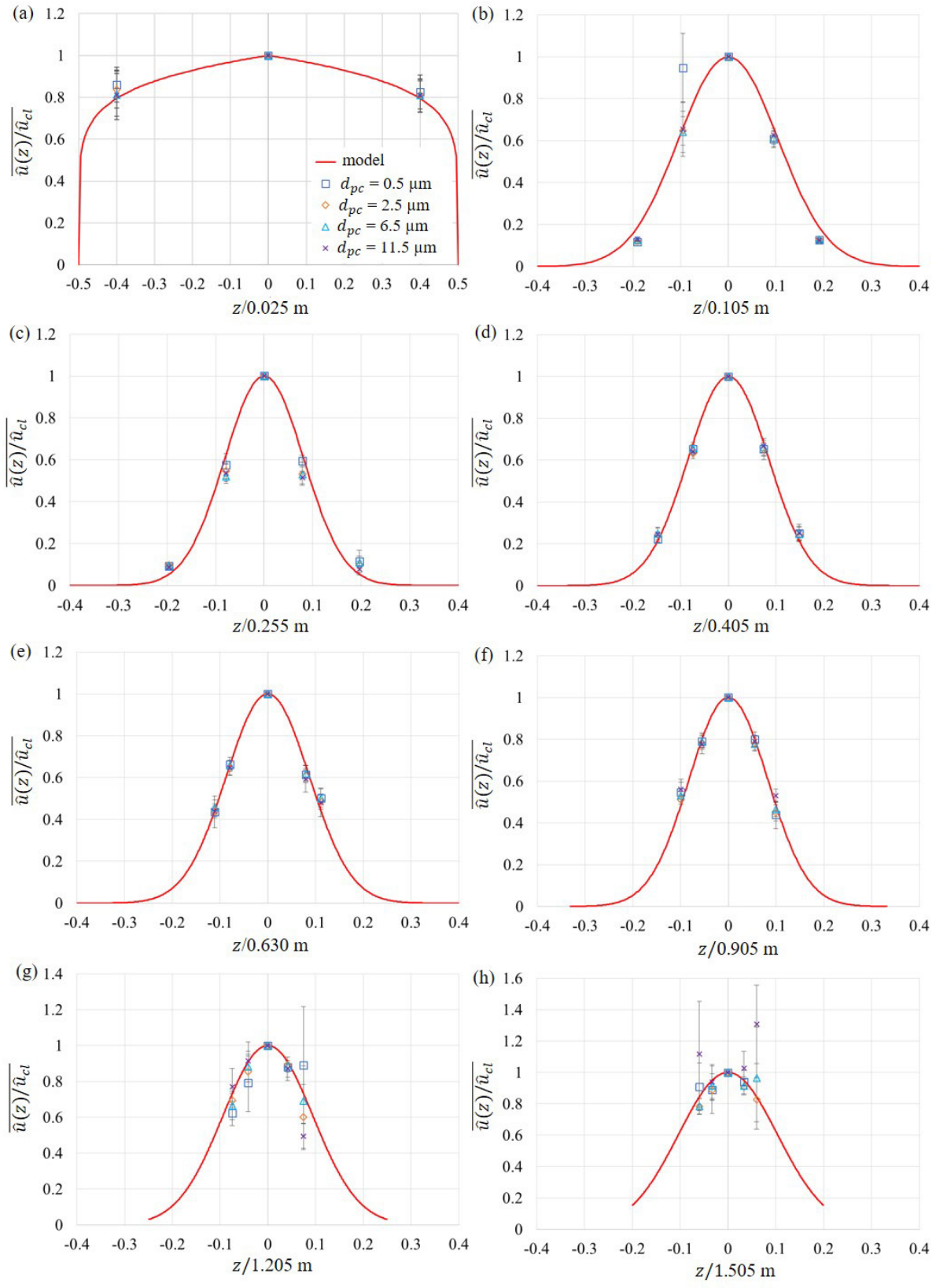

Figure 5.12.: Discharge average radial velocity profile $\overline{\hat{u}(z, y = 0)/\hat{u}_{cl}}$ against the radial distance z, scaled with the axial distance x for a helium jet. Error bars indicate the standard deviation: (a) power-law model, (b) to (h) Gauss model.

The experimental data are fitted with a Gaussian distribution according to equation (2.4) and the spreading rates $K_{2,u}$ are determined according to equation (2.6). The spreading rates $K_{2,u}$ obtained in this way are summarised in Table 5.8 for the three gases and for different axial distances 0.025 m $< x/d \leq$ 1.505 m. Initially, the spreading rate drops due to the change from a turbulent pipe flow velocity profile to a Gaussian profile and then remains approximately constant in the self-similar region 25 > x/d. The mean spreading rate for the transient air jet is $K_{2,u}$ = 0.099, for the carbon dioxide jet $K_{2,u}$ = 0.098 and for the helium jet $K_{2,u}$ = 0.104.

Based on the measurement data, no significant correlation (p > 0.31) between the spreading rate $K_{2,u}$ and the gas can be determined. This does not mean that there is no dependence of the spreading rate on density, but the available data may not be sufficient for a conclusion. This corresponds to the statement by Chen and Rodi (1980) that the spreading rate $K_{2,u}$ is independent of the density ratio R_ϱ. However, it contradicts the experimental results of Wang and Andreopoulos (2010). It is interesting to note that the values for the decay constant $K_{1,u}$ that were determined by Wang and Andreopoulos (2010) are in some cases considerably greater than those determined by other authors. A reason for this cannot be readily identified, because (for example) the data from helium were not entered into the charts in their work.

Table 5.8.: Discharge average spreading rates $K_{2,u}$ for different axial distances x for air, carbon dioxide $t \leq$ 16 s and helium $t \leq$ 3.5 s. Modified from PPA1.

		Air	Carbon dioxide	Helium
x in m	x/d	$K_{2,u}$	$K_{2,u}$	$K_{2,u}$
0.025	1	-	-	-
0.105	4.2	0.128	0.150	0.126
0.255	10.2	0.091	0.090	0.091
0.405	16.2	0.087	0.081	0.097
0.630	25.2	0.095	0.088	0.100
0.905	36.2	0.098	0.094	0.099
1.205	48.2	0.101	0.113	0.111
1.505	60.2	0.100	0.100	0.122
mean	(25.2 $d \leq x \leq$ 48.2 d)	0.099	0.098	0.104
standard deviation	(25.2 $d \leq x \leq$ 48.2 d)	0.002	0.015	0.014

5.5.4. Reynolds number dependency of spreading rate

In this section, the influence of the Reynolds number Re on the spreading rate $K_{2,u}$ is analysed statistically. For this purpose, the spreading rate $K_{2,u}$ determined for the individual points in time in the self-similar region 0.630 m $\leq x \leq$ 1.205 m are plotted against the corresponding Reynolds number Re in Figure 5.13 for the three gases. The spreading rates $K_{2,u}$ of the four smallest particle classes d_{pc} = 0.5 µm (blue squares), d_{pc} = 2.5 µm (orange diamonds), d_{pc} = 6.5 µm (turquoise traingles) and

d_{pc} = 11.5 µm (purple crosses) are shown. Furthermore, the charts in Figure 5.13 show the transition from the inertia-dominated to the buoyancy-affected free jet (dashed-black line).

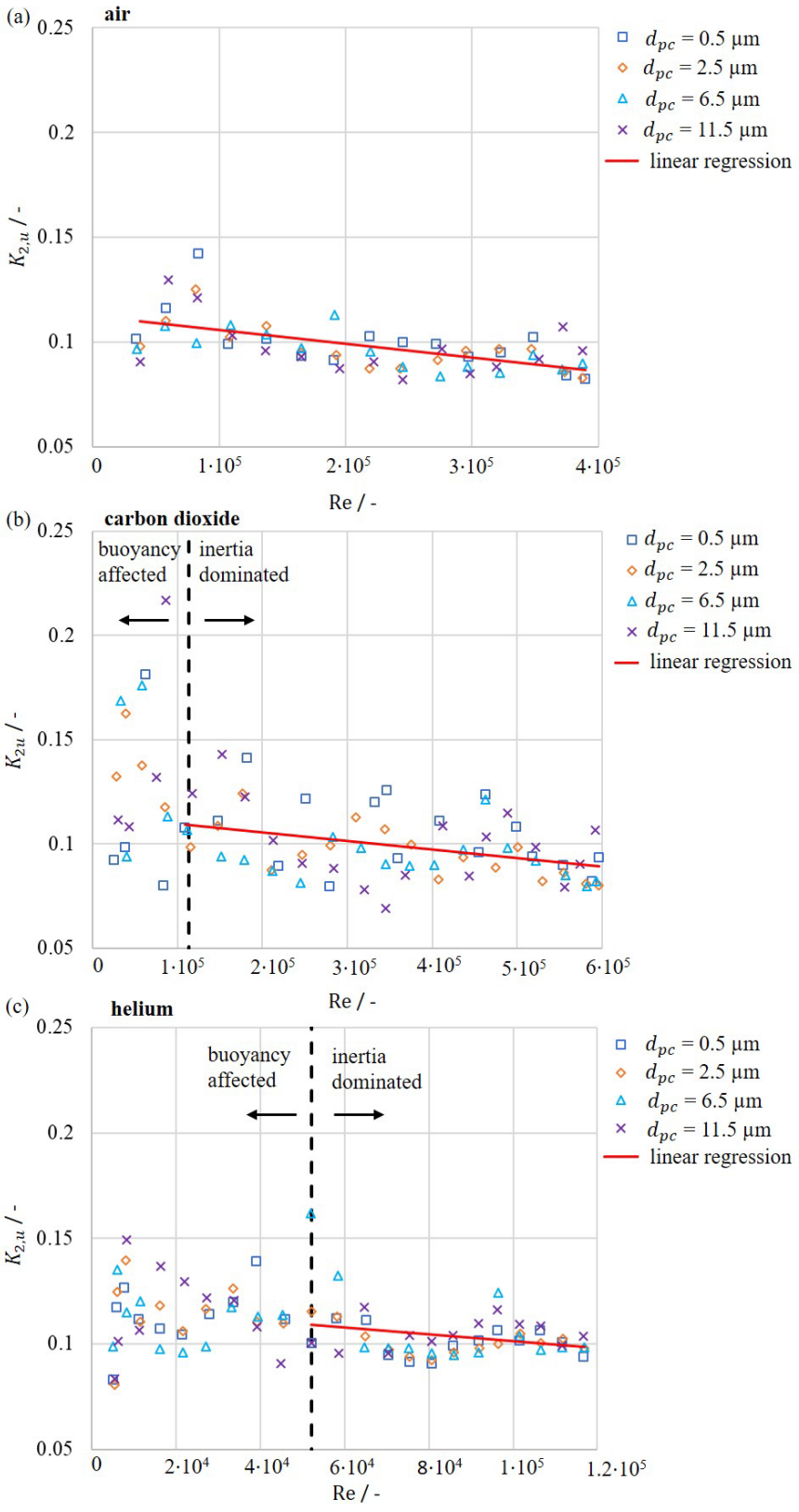

Figure 5.13.: Spreading rate $K_{2,u}$ against Reynolds number Re. $K_{2,u}$ is given for different particle classes d_{pc} and cumulative regressions are derived for (a) air jet, (b) carbon dioxide jet and (c) helium jet. Modified from PPA1.

For all three gases, the spreading rate $K_{2,u}$ decreases with increasing Reynolds number Re in the inertia-dominated regime. This corresponds to a smaller opening angle, and thus to a narrower free jet with increasing Reynolds number Re. This correlation fits with the dependence of the decay constant $K_{1,u}$ on the Reynolds number Re observed earlier in section 5.5.2. There, a slower velocity decrease on the centre line with increasing Reynolds number Re was observed. To avoid a break in the conservation of momentum, the spreading rate $K_{2,u}$ must decrease if the decay constant $K_{1,u}$ increases. Exactly this behaviour can be observed here, which is why the dependence of the decay constant $K_{1,u}$ and spreading rate $K_{2,u}$ on the Reynolds number Re appears to be physically reasonable. Furthermore, this agrees with the theory of Pope (2015) according to which the correlation $K_{1,u} \cdot K_{2,u} = 0.55$ between the decay constant $K_{1,u}$ and the spreading rate $K_{2,u}$ must hold. For the quantitative evaluation of the Reynolds number dependence of the spreading rate $K_{2,u}$, the spreading rate $K_{2,u}$ is modelled with a linear regression in the inertia-dominated regime (red line), i.e.

$$K_{2,u} = c_{2,a} \cdot \mathrm{Re} + c_{2,b}. \tag{5.8}$$

Thus, a coefficient of the Reynolds number of $c_{2,a} = 0$ is defined as the null hypothesis, which corresponds to the case where the Reynolds number has no influence on the spreading rate $K_{2,u}$. The alternative hypothesis, tests whether the coefficient $c_{2,a}$ is significantly different from zero. In Table 5.9 the coefficients $c_{2,a}$ and $c_{2,b}$ are summarised, as well as the significance p-values. Due to the small significance p-values for the coefficient $c_{2,a}$, a statistically significant dependence of the spreading rate $K_{2,u}$ on the Reynolds number Re is confirmed for all three gases. This fits with the observations from LES by Bogey and Bailly (2006), and Bonelli et al. (2021), as well as with experimental results by Borée et al. (1996). Since the influence of the Reynolds number Re on the spreading rate $K_{2,u}$ is very small, similar to the decay constant, the influence of the Reynolds number Re on the propagation behaviour is probably negligible for most technical problems (Thring and Newby, 1953). Consequently, the definition of a universal spreading rate $K_{2,u} = 0.10$ appears to be suitable.

Table 5.9.: Summary of the coefficients $c_{2,a}$ and $c_{2,b}$ and the corresponding significance values p. Modified from PPA1.

	Air	Carbon dioxide	Helium
$c_{2,a}$	$-5.80 \cdot 10^{-8}$	$-4.10 \cdot 10^{-8}$	$-1.62 \cdot 10^{-7}$
p-value$(c_{2,a})$	$1.453 \cdot 10^{-6}$	$7.521 \cdot 10^{-4}$	$1.62 \cdot 10^{-7}$
$c_{2,b}$	0.11	0.11	0.12
p-value$(c_{2,b})$	$< 10^{-16}$	$< 10^{-16}$	$< 10^{-16}$

In the buoyancy-affected regime, carbon dioxide and helium behave somewhat differently. For example, the spreading rate $K_{2,u}$ of carbon dioxide has a greater gradient with increasing Reynolds number Re in the buoyancy-affected regime than in the inertia-dominated regime. For the helium jet, the spreading

rate even decreases with decreasing Reynolds number in the buoyancy-affected regime. This behaviour does not necessarily mean a violation of the momentum conservation because only the velocity field was considered here. Since the momentum is also dependent on the density, and according to the density-entrainment effect, a shift of the density field occurs. Therefore, the assumption of a constant product of decay constant and spreading rate no longer holds for the buoyancy-affected regime.

5.6. Findings for transient free jets

Experimental investigations were carried out on the propagation of transient vessel discharge. For this purpose, a specially designed test facility was set up to measure the velocity field of the escaping gas free jet from the vessel. The measurement of the velocity field of a transient vessel discharge was carried out for the first time using an LDA and PDA. Compared to an LDA, PDA provides decisive information by measuring both the particle's size and velocity. This ensured that the evaluated ethylene glycol-water tracers had the same velocity as the gas. In the evaluation, the free jets were divided into an inertia-dominated and a buoyancy-affected regime to avoid apparent deviations due to buoyancy effects.

Based on a static analysis of the measurement data, the following conclusions could be drawn for transient free jets in the inertia-dominated regime:

- A statistically significant correlation between the decay constant and Reynolds number, as well as the spreading rate and Reynolds number, was clearly identified. However, the influence of the Reynolds number is so small that it should be negligible for most technical problems.
- The question of the dependence of a free jet on the Reynolds number, which has been discussed controversially in the literature, could thus be clarified.
- No statistically significant correlation could be observed between the density ratio R_ϱ and the decay constant $K_{1,u}$, as well as the spreading rate $K_{2,u}$.
- A transient free jet also exhibits a self-similar velocity field. However, given that the time-dependent mean outlet velocity and not the single velocity is used for scaling, this behaviour can only be described as quasi-self-similar.
- Therefore, the definition of a universal decay constant $K_{1,u} = 5.90$ and spreading rate $K_{2,u} = 0.10$ appears suitable. This leads to a product of $K_{1,u} \cdot K_{2,u} = 0.59$, which is almost exactly the mean value from the literature data $K_{1,u} \cdot K_{2,u} = 0.58$ in Table 2.1.

These conclusions fit with the observations from LES by Bogey and Bailly (2006), and Bonelli et al. (2021), as well as with experimental results by Borée et al. (1996) for stationary free jets. These findings refute the theory of Pope (2015), according to which the influence of the Reynolds number on the propagation can only be explained by measurement inaccuracies. At this point, however, a question opens

up: Is the influence of the Reynolds number on the transient free jets investigated here only an apparent effect due to the transient flow character or buoyancy effects? This will be examined in the next chapter using steady-state numerical simulations.

6. Numerical investigation of stationary free jets

In this chapter, the experimental results from chapter 5 are reproduced based on numerical simulations of the spreading region. The experimental results are to be validated by specifically eliminating sources of error. Thus, in numerical simulations, in contrast to experimental tests, buoyancy can be eliminated. Furthermore, the velocity field in numerical simulations does not have to be assembled by individual experiments at different points but can be determined within a single numerical simulation. This eliminates the influence of variations in ambient conditions and the same conditions are always present.

The simulations are intended to eliminate two uncertainties in the evaluation of the experimental data. First, it will be shown that the experimentally investigated transient free jet behaves like a stationary free jet for the individual points in time and that the observed influence of the Reynolds number on the propagation cannot be attributed to the transient flow character. Second, it will be shown that the influence of the Reynolds number on the propagation is not an apparent effect of buoyancy.

6.1. Numerical setup

The numerical simulations are performed with ANSYS CFX©. The standard k-ε turbulence model according to Launder and Spalding (1974) is used, as well as the generalised k-ω turbulence (GEKO) model according to Menter et al. (2019). Both models were already discussed in section 3.3.1. Since the simulations are deliberately made without buoyancy, the rotational symmetry around the x-axis can be exploited and the geometry can be reduced to a 4° wedge with only one cell in the azimuthal direction. This corresponds to a 2D simulation. Since only stationary free jets are investigated, the geometry can be reduced to the outlet pipe and the spreading region. The dimensions of the pipe in the computational domain corresponds to the dimensions of the experimental investigations in chapter 5. The pipe has a length of L = 0.4 m and an inner radius of r = 0.025 m. The spreading region has a length of L_S = 5 m and a radius of r_s = 2 m. The dimensions of the spreading region are selected based on equation (2.1) in such a way that the free jet has decayed at least 95 % of its velocity in this region. The pipe section is considered to determine the velocity profile that forms along the pipe. The geometry is depicted in Figure 6.1.

The following advisory/analysis services of the Statistical Consulting and Analysis Centre for Higher Education TU Dortmund University were used for this chapter: statistical methodology, selection of statistical software and statistical programming using R Core Team (2022), data analysis.

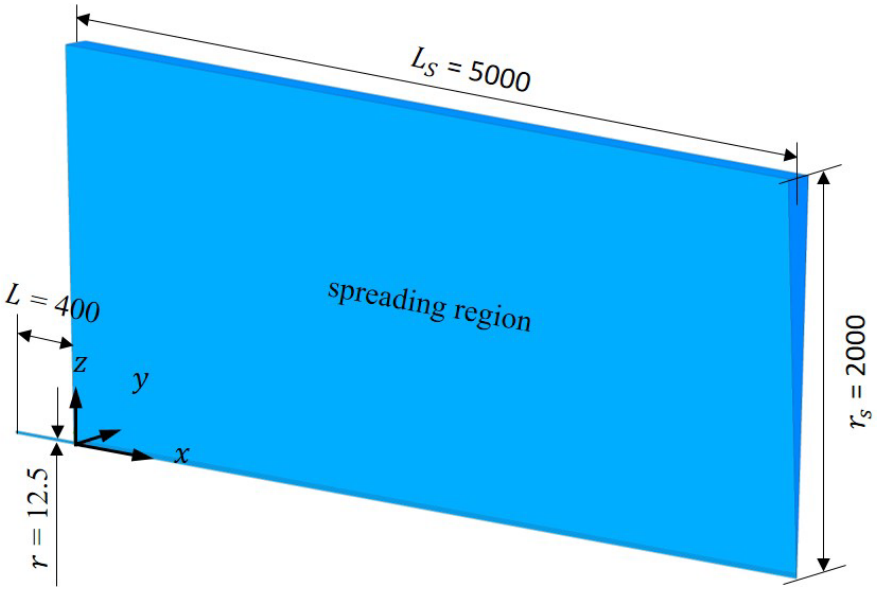

Figure 6.1.: Sketch of the geometry under investigation, which is rotationally-symmetric (2D) around the x-axis. All dimensions are in mm.

For the geometry, a mesh is generated that fulfils the mesh requirements already listed in section 4.3. An example of a coarse mesh with 19 600 cells is shown in Figure 6.2. The actual resolution used in the numerical simulations is considerably greater with 77 600 cells, but the mesh is then so fine that it is difficult to identify the structure in the illustration. The mesh essentially corresponds to that of the simulations in section 4.3 and the mesh requirements formulated there. Hereby, the spreading region is considerably greater because the focus here is on the free jet propagation.

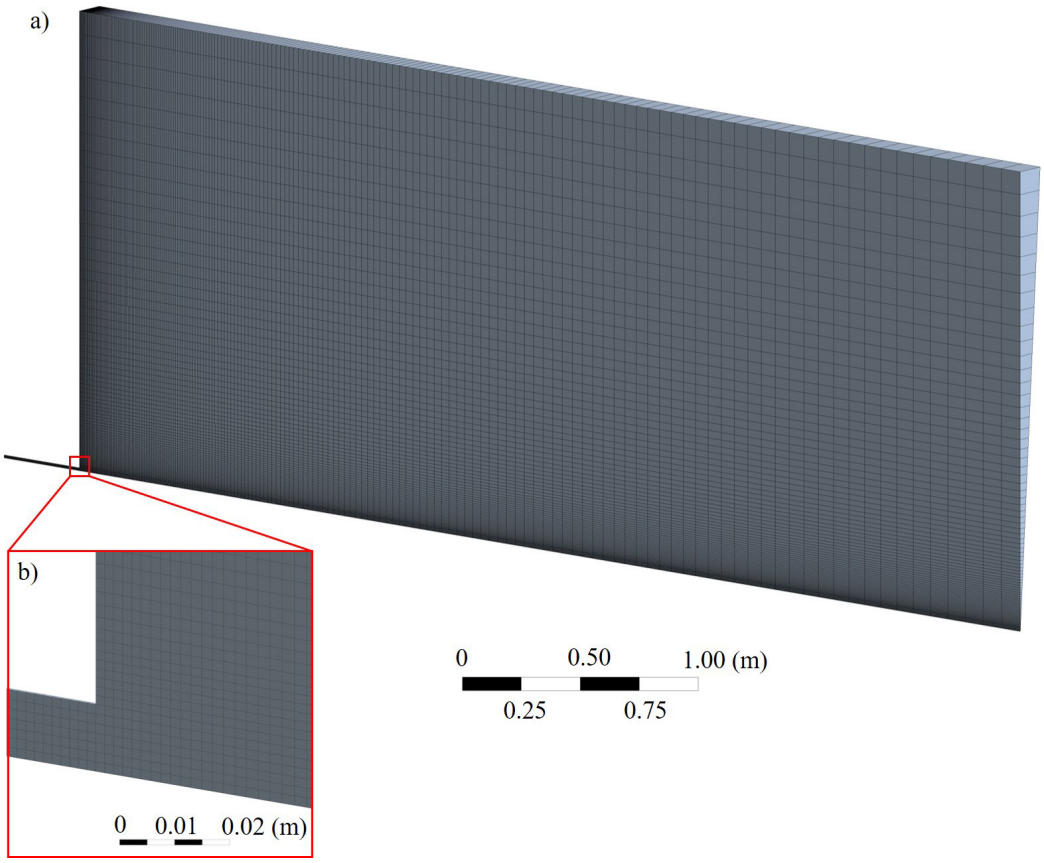

Figure 6.2.: Example of a structured computational mesh with 19 600 cells. (a) Angled view of the complete computational domain, (b) close up of the pipe to the spreading region.

In the following section, the boundary conditions and start values are explained. These basically correspond to the boundary conditions from section 4.3. Stationary simulations are to be compared with the transient experimental investigations. For this purpose, several different points in time from the experimental discharge are considered and the corresponding pressure within the vessel is used as a boundary condition at the inlet in the numerical simulations. However, the inlet temperature is deliberately left constant at T_0 = 298 K to exclude effects due to a change in density. The pipe wall is defined as a no slip adiabatic wall. Hence, on the one hand the velocity normal and tangential to the wall is zero u_{wall} = 0 m/s, and on the other hand no heat flow is allowed through the wall q_{wall} = 0. At the cutting planes, a symmetry condition is appeared. This leads to a Dirichlet boundary condition u_n = 0 m/s and to a Neumann boundary condition $\partial\phi/\partial\vec{n}$ = 0. The further boundaries of the spreading region are considered as openings allowing for entrainment. Here, both an inflow and an outflow may occur. This is particularly important for the entrainment into a free jet, in which (for example) surrounding gas is sucked in. Two Dirichlet boundary conditions are specified at the opening: first, a static relative pressure of p_{opening} = 0 Pa, and second an ambient temperature of T_{opening} = 298 K. This temperature is also used as the start value for the entire spreading region. The boundary conditions are visualised in Figure 6.3.

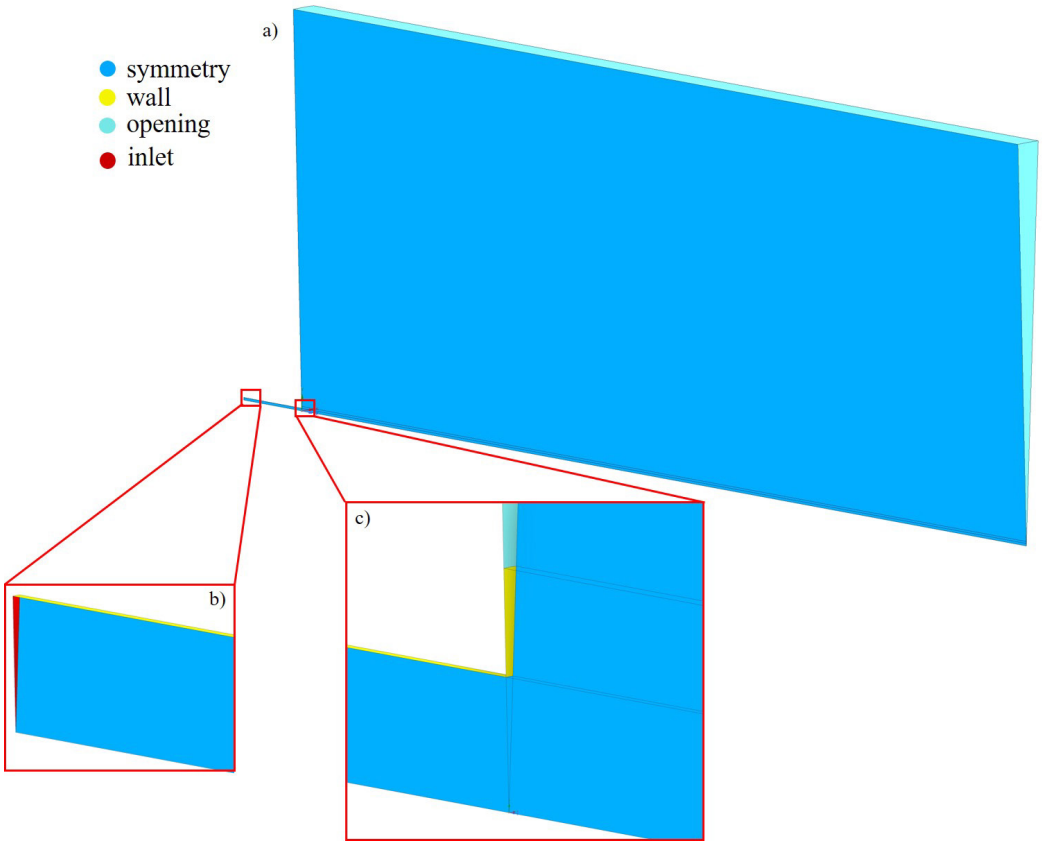

Figure 6.3.: Schematic representation of the boundary conditions used. (a) Angled view of the complete domain, (b) close up of pipe inlet and (c) close up of the transition from the pipe to the spreading region.

6.2. Results and discussion non-buoyant stationary free jets

In this section, the results from the numerical simulations of free jet propagation are presented. The results from the non-buoyant, stationary simulations for the various turbulence models are examined and compared with the experimental data. This should clearly exclude the possibility that the influences observed in chapter 5 are due to transient flow behaviour and buoyancy effects. An overview of the simulations carried out can be found in Table A.1, Table A.2 and Table A.3 in the appendix.

At the beginning of the evaluation, a qualitative plausibility check of the numerical simulations should be carried out. Therefore, the streamlines in the spreading region for an air jet at an inlet pressure of p_0 - p_∞ = 474 mbar are considered as an example in Figure 6.4. This corresponds to the transient discharge experimentally investigated in chapter 5 at a time of t = 0.5 s after opening. The streamlines are coloured according to the velocity field, whereby a logarithmic scaling was chosen. The velocity of the free jet after the pipe outlet initially remains constant and then drops rapidly. This corresponds to the freejet theory from chapter 3, according to which the velocity remains almost constant in the core region and then a hyperbolic velocity decay takes place. Furthermore, the entrainment of the free jet can be observed by the curved streamlines as the free jet draws in the surrounding gas.

A vortex can be identified at the end of the computational domains. For the k-ε turbulence model the vortex centre is inside the domain and for the GEKO model the vortex centre is outside the computational domain. Differently sized computational domains were investigated, whereby the vortex always appeared at the end of the computational domain. Therefore, the vortex seems to be an artefact. The reason for the formation of the artefact could be the relatively low flow velocity prevailing in this area in combination with the boundary condition opening to entrainment, which allows both inflow and outflow. The simulations with differently sized computational domains also showed that the problem is independent of the size of the computational domain because the velocity fields differed by less than 1%. This also shows that it makes sense to select a computational domain that is somewhat greater than the range to be evaluated to avoid skewing the solution due to boundary effects.

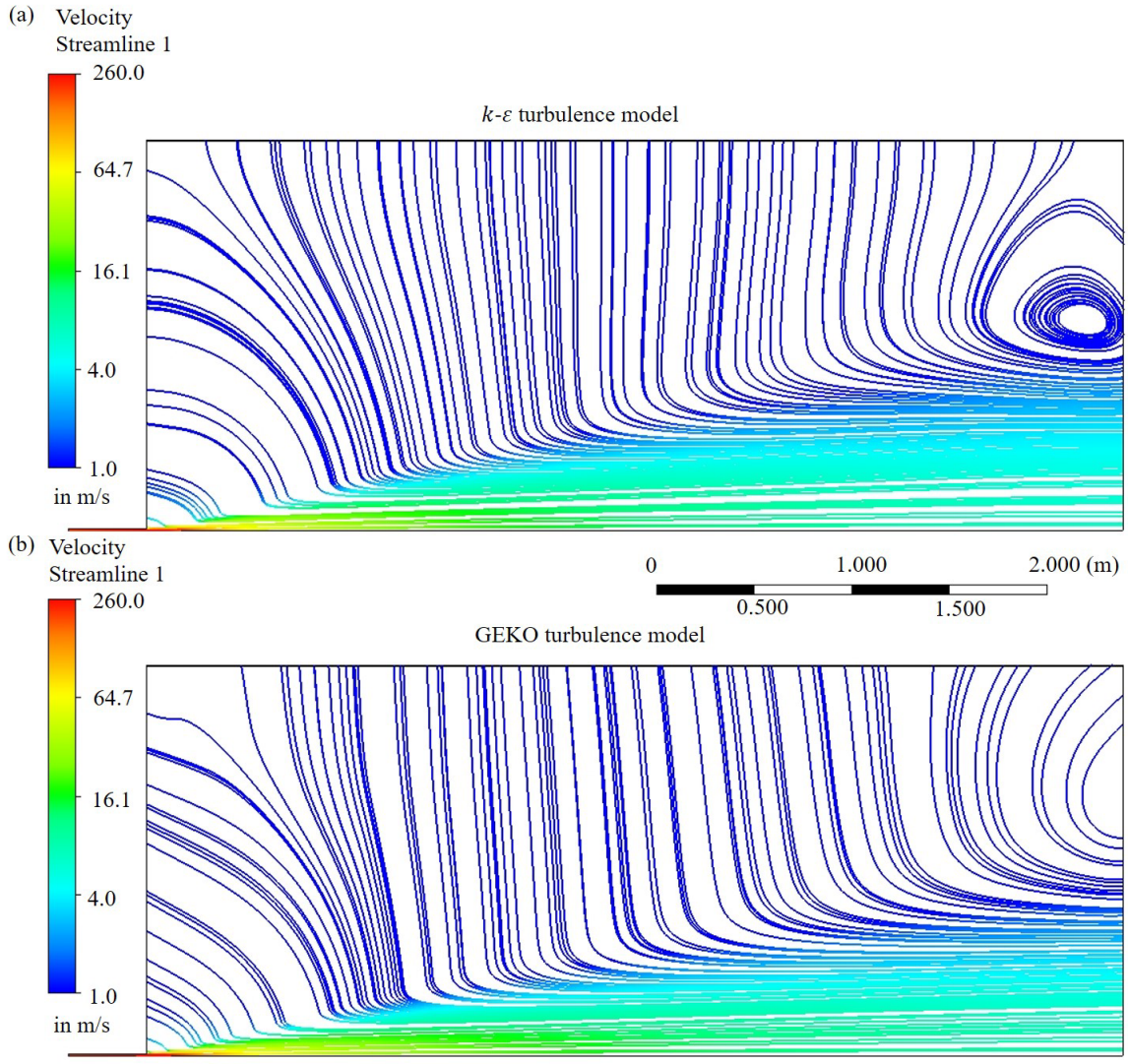

Figure 6.4.: Streamlines in the spreading region of a stationary air jet at an inlet pressure difference of $p_0 - p_\infty = 474$ mbar, computed with (a) the k-ε turbulence model and (b) the GEKO turbulence model.

The velocity profile on the centre line is then evaluated. For this purpose, the velocity on the centre line is scaled with the outlet velocity $\overline{\hat{u}_0/\hat{u}_{cl}}$ and plotted in inverse form against the axial distance, scaled with the effective diameter, x/d_e, in Figure 6.5. For each gas, all simulations (cf. Table A.1, Table A.2 and Table A.3.) are averaged, which means that the results correspond to the discharge-averaged data from the experiments (cf. Figure 5.6). The averaged axial velocity profiles in non-inverse form $\overline{\hat{u}_{cl}/\hat{u}_0}$ can be found in Figure A.1 in the appendix.

For all three gases, there is a good agreement between the experimental and numerical results with the k-ε and the GEKO turbulence model. The greatest differences are first in the near field, where the experimental velocities are somewhat greater than the numerical velocities and there is a smooth transition to the transient region. The error bars of the numerical simulations result from the averaging over the simulations for the respective gas with the different initial pressures. Therefore the error bars are an indicator of the deviation for different inlet pressures. Based on the error bars, which are so small that they are practically undetectable, there is a high level of agreement, which indicates a self-similar velocity field. The profiles of the k-ε model and GEKO model are similar, with the GEKO model having a slower velocity decay and being closer to the experimental data. Furthermore, the core lengths x_c of the stationary simulations and the transient experiments are summarised in Table 6.1. A good agreement is observed for the length of the core region for the different numerical simulations and experimental data. Here, the GEKO model tends to deliver an about 30 % greater core lengths x_c.

Table 6.1.: Core length x_c of the non-buoyant free jets of the stationary simulations and the transient experiments.

x_c/d	Air	Carbon dioxide	Helium
exp.	5	6.2	4.2
k-ε	6	6.4	4.8
GEKO	6.4	8	5.6

A quantitative analysis of whether the k-ε model or the GEKO model is closer to the experimental data is difficult at this point. For this purpose, the decay constant will be examined in more detail in Figure 6.7.

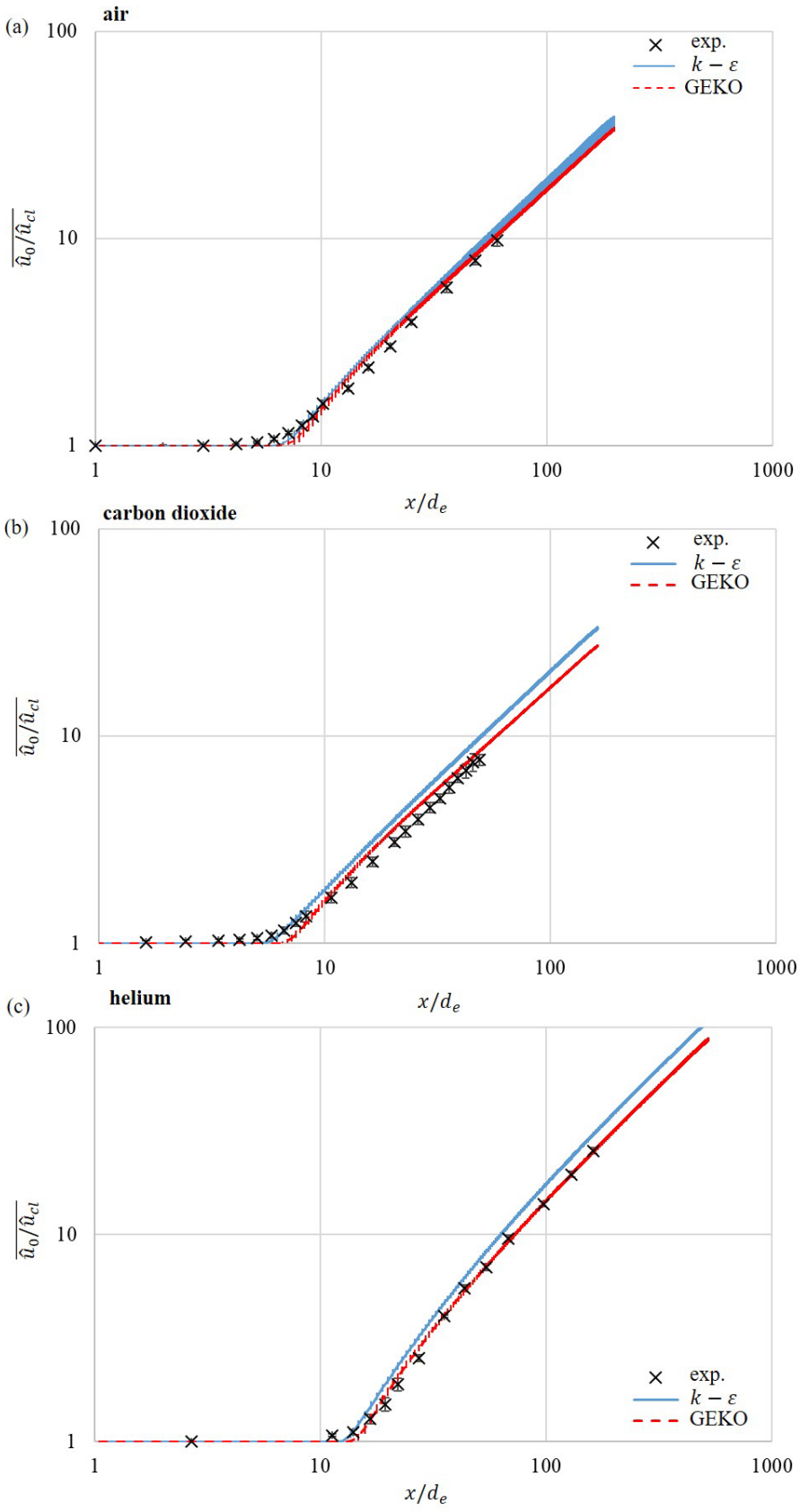

Figure 6.5.: Results of the inverse averaged axial velocity profile $\overline{\hat{u}_0/\hat{u}_{cl}}$ against the scaled axial distance x/d_e of the numerical simulations with the k-ε and GEKO model, compared to the experimental data (exp.). (a) Air jet, (b) carbon dioxide jet and (c) helium jet. Error bars indicate the standard deviation.

The radial profile of the axial velocities at different axial distances is now considered. For this purpose, the scaled discharge-averaged current mean velocity $\overline{\hat{u}/\hat{u}_{cl}}$ is plotted against the radial distance z, which is scaled by the axial distance x to exploit the self-similarity. The results from the numerical simulations with the k-ε model and the GEKO model are compared with the experimental results from section 5.5.3. Here, the profiles of the numerical simulations are created by averaging the simulations with the different inlet pressures. Thus, they correspond to the discharge-averaged profiles from the experimental investigations. Therefore, the error bars of the numerical simulations are an indicator of how great the deviations between the different injection pressures are. The error bars for the numerical simulations in Figure 6.6 are so small that they are practically undetectable. Accordingly, the radial velocity profiles of the numerical simulations are, almost independent of the injection pressure. Furthermore, the numerical profiles for all axial distances are almost ideally on top of each other for charts (a) to (f). This suggests that there is spatial self-similarity because the propagation through the scaling is independent of the axial distance. Due to the low average relative standard deviation of the simulations with the k-ε model of 0.86% and the GEKO simulations of 1.45%, a self-similarity independent of the pressure can be observed. For the air and carbon dioxide jets, the experimental data are slightly below the k-ε model but almost congruent on the profiles of the GEKO model. For helium, the experimental data are above the GEKO model, which corresponds to a broader velocity profile. In contrast, there is a good agreement between the experimental helium data and the k-ε model. Accordingly, the GEKO model tends to produce a smaller spreading rate $K_{2,u}$ for the helium jet.

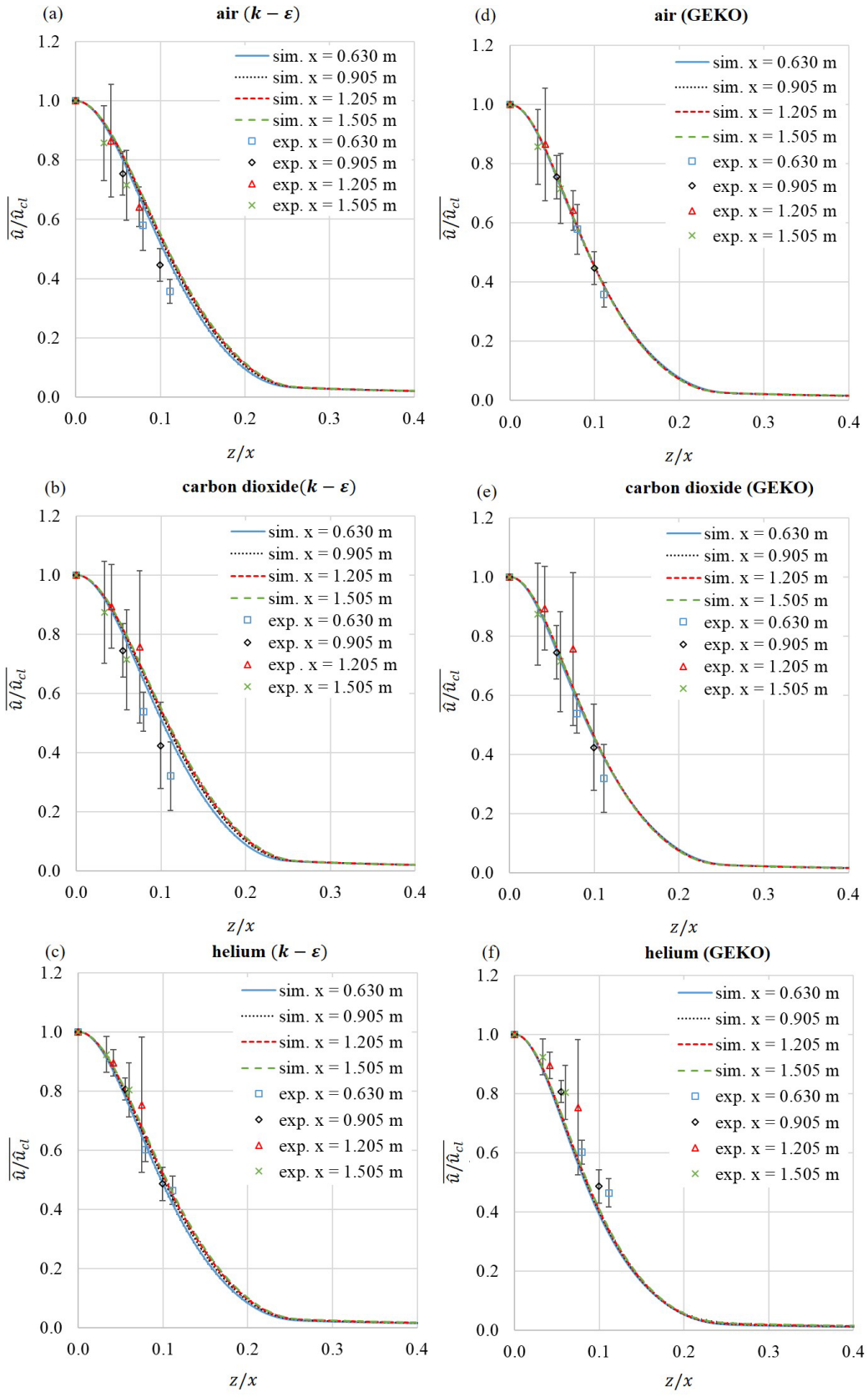

Figure 6.6.: Discharge average radial velocity profile $\overline{\hat{u}/\hat{u}_{cl}}$ against the radial distance z scaled with the axial distance x. Error bars indicate the standard deviation of the experimental data. (a) Air jet with k-ε model, (b) carbon dioxide jet with k-ε model, (c) helium jet with k-ε model, (d) air jet with GEKO model, (e) carbon dioxide with GEKO model and (f) helium jet with GEKO model.

In the following, the decay constant $K_{1,u}$ and spreading rate $K_{2,u}$ from the stationary numerical simulations will be compared with the transient experimental results from section 5.5.2 and 5.5.4. Figure 6.7 shows the decay constant $K_{1,u}$ and spreading rate $K_{2,u}$ plotted against the Reynolds number Re. There is a reasonable agreement between the experimental data and the GEKO simulations. The mean relative deviations of the decay constant and spreading rate for the two turbulence models from the experimental data are summarised in Table 6.2. Here, the decay constants of the GEKO model with a deviation of less than 1 % are considerably more accurate than the k-ε model, which deviates by almost 20 %. This fits with the observations of Pope (1978) that the k-ε turbulence model leads to a faster velocity decay when calculating round free jets, which corresponds to a smaller decay constant $K_{1,u}$. For the spreading rate $K_{2,u}$, the situation is somewhat different. For air and carbon dioxide, the GEKO model is also closer to the experimental data, but not for helium.

Table 6.2.: Mean relative deviations of the k-ε and GEKO turbulence models, compared to the experimental data for the decay constant $K_{1,u}$ and spreading rate $K_{2,u}$.

mean relative deviation / %	Air		Carbon dioxide		Helium	
	$K_{1,u}$	$K_{2,u}$	$K_{1,u}$	$K_{2,u}$	$K_{1,u}$	$K_{2,u}$
k-ε / exp.	-18.60	+9.45	-16.22	+9.98	-16.28	-1.6
GEKO / exp.	-0.60	-4.65	0.75	-3.98	+0.74	-17.65

A pattern can be seen here for both the numerical simulations and the experimental data, irrespective of the gas. The decay constant increases and the spreading rate decreases with increasing Reynolds number. For the quantitative analysis of the influence of the Reynolds number on the decay constant and spreading rate, these are approximated with linear regressions (cf. equation (5.6) and (5.8)) analogous to the experimental data. Thus, a coefficient of the Reynolds number of $c_{1,a}$ = 0 and $c_{2,a}$ = 0 is defined as the null hypothesis, which corresponds to the case where the Reynolds number has no influence on the decay constant $K_{1,u}$ and spreading rate $K_{2,u}$. The alternative hypothesis, tests whether coefficients $c_{1,a}$ and $c_{2,a}$ are significantly different from 0.

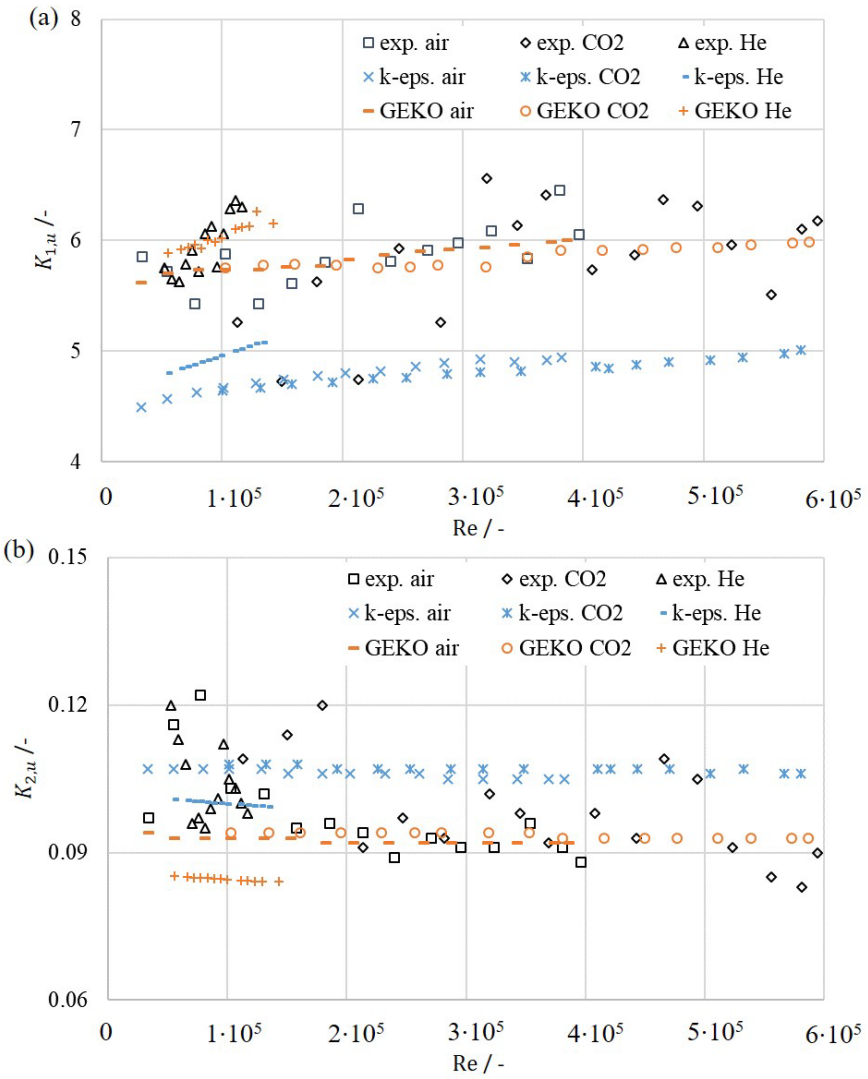

Figure 6.7.: (a) Decay constant $K_{1,u}$ against Reynolds number Re. (b) Spreading rate $K_{2,u}$ against Reynolds number Re. Comparison of the numerical simulations with the k-ε (k-eps.) and GEKO models with the experimental (exp.) results of section 5.5.2 and 5.5.4.

In Table 6.3, the coefficients $c_{1,a}$ and $c_{2,a}$ are summarised, as well as the significance p-values. Due to the small significance p-values for the coefficients $c_{1,a}$ and $c_{2,a}$, a statistically significant dependence of the decay constant $K_{1,u}$ and spreading rate $K_{2,u}$ on the Reynolds number Re is confirmed for all three gases and for both turbulence models. Since this behaviour is also observed in the stationary simulations, it can be assumed that the behaviour of the experimental investigations is not due to the transient flow character. It also shows that the influence of the Reynolds number on the decay constant and spreading rate is not only an apparent influence due to buoyancy effects because these were deliberately switched off in the present CFD simulations.

Table 6.3.: Summary of the coefficients $c_{1,a}$, $c_{2,a}$ and the corresponding significance p-values for the non-buoyant stationary CFD simulations.

	k-ε			GEKO		
	air	CO_2	helium	air	CO_2	helium
$c_{1,a}$	$1.172 \cdot 10^{-6}$	$7.041 \cdot 10^{-7}$	$3.858 \cdot 10^{-6}$	$9.987 \cdot 10^{-7}$	$4.990 \cdot 10^{-7}$	$4.158 \cdot 10^{-6}$
p-value$(c_{1,a})$	$< 10^{-16}$	$< 10^{-16}$	$< 10^{-16}$	$< 10^{-16}$	$< 10^{-16}$	$9.32 \cdot 10^{-8}$
$c_{2,a}$	$-6.866 \cdot 10^{-9}$	$-3.559 \cdot 10^{-9}$	$-1.962 \cdot 10^{-8}$	$-4.974 \cdot 10^{-9}$	$-2.607 \cdot 10^{-9}$	$-1.530 \cdot 10^{-8}$
p-value$(c_{2,a})$	$< 10^{-16}$	$6.649 \cdot 10^{-15}$	$< 10^{-16}$	$6.823 \cdot 10^{-14}$	$< 10^{-16}$	$< 10^{-16}$

The mean decay constant for the k-ε model is $K_{1,u}$ = 4.82 and for the GEKO model $K_{1,u}$ = 5.90. Thus, the decay constant of the GEKO model, corresponds exactly to the experimentally determined decay constant $K_{1,u}$ defined in section 5.5. The mean spreading rate $K_{2,u}$ for the k-ε model is $K_{2,u}$ = 0.104 and for the GEKO model $K_{2,u}$ = 0.090. Thus, the experimentally determined spreading rate $K_{2,u}$ = 0,100, is between the spreading rates $K_{2,u}$ determined with the two turbulence models.

To validate the results, a grid-independence study is performed according to section 3.3.3. The results are summarised in Table 6.4 and plotted in Figure 6.8. There is no extrapolated value for the decay constant $K_{1,u}$ of the GEKO model because there is no monotonous slope of the different mesh resolutions. For both the k-ε and GEKO models, the decay constant $K_{1,u}$ monotonously decreases for finer mesh resolution. Meanwhile, the spreading rate $K_{2,u}$ monotonously increases for the k-ε model and decreases for the GEKO model for a finer mesh resolution. The mean deviation from the extrapolation is 5.02 % for the coarse mesh, 2.07 % for the medium mesh and 0.94 % for the fine mesh. However, since the computation time increases sixfold with each refinement, the medium mesh is used as a trade-off between accuracy and computational effort.

Table 6.4.: Overview of the results from the grid-independence study with air and $p_0 - p_\infty = 47\,411$ Pa.

		k-ε		GEKO	
mesh	no elements	$K_{1,u}$	$K_{2,u}$	$K_{1,u}$	$K_{2,u}$
coarse	19 600	4.905	0.1055	6.100	0.0975
medium	77 600	4.774	0.1061	6.000	0.0915
fine	308 000	4.699	0.1063	6.016	0.0899
extrapolation	-	4.603	0.1063	-	0.0892

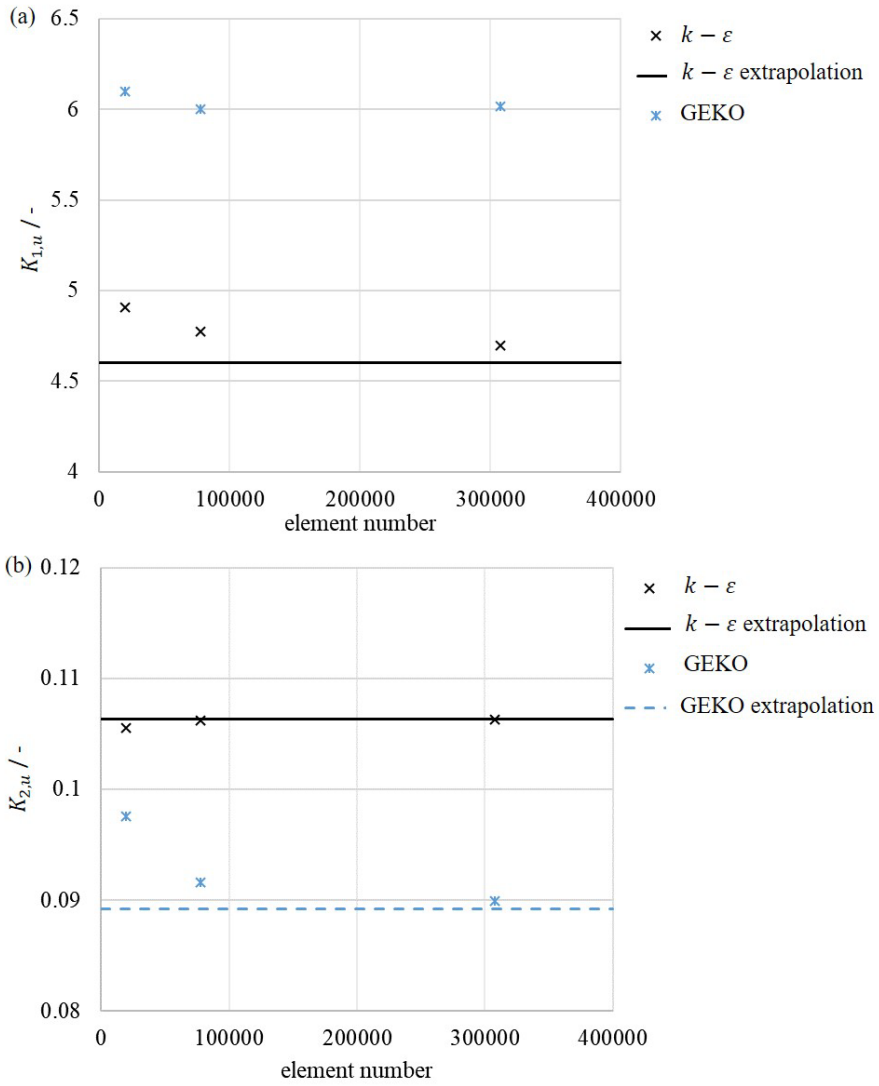

Figure 6.8.: Results of the grid independence study. (a) Decay constant $K_{1,u}$, (b) spreading rate $K_{2,u}$.

6.3. Findings on the simulation of stationary free jets

In this chapter, the experiments were reproduced in an idealized form by numerical simulations. For this purpose, different points in time of the experimental tests were used as boundary conditions for steady-state simulations. Here, two potential questions of the experimental evaluation could be clearly answered.

It was also shown that stationary non-buoyant free jets have a significant dependence on the Reynolds number, which is very similar to that of the experimentally-investigated transient free jets. Thus, the Reynolds number dependence of the decay constant $K_{1,u}$ (p-value < $9.32 \cdot 10^{-8}$) and of the spreading rate $K_{2,u}$ (p-value < $6.82 \cdot 10^{-14}$) of free jets is not just an apparent effect due to a transient flow character or due to buoyancy effects.

Even though a significant dependence of the Reynolds number on the decay constant and spreading rate was found in the numerical simulations, the relevance of this dependence is probably negligible for most technical applications. Thus, it seems justified to speak of a self-similar velocity field for free jets, which is independent of the injection pressure of the outlet velocity.

It was further shown that the GEKO model with a separation coefficient of C_{sep}= 2.2 and a mixing coefficient of C_{mix} = 0.3 is closer to the experimental data of air and carbon dioxide free jets than the standard k-ε model. For the helium free jet, the situation is different and the GEKO model gives greater deviations from the experimental data than the standard k-ε model. How far the GEKO model can be optimised in this respect by other turbulence parameters has to be shown in future investigations. Consequently, this optimisation has to be considered with caution because the goal of numerical simulations should not be to fit to experimental data by introducing more and more parameters.

7. Summary and outlook

In the context of this work, the compressible, transient and subcritical outflow of a gas from a vessel was considered. The focus was on both the condition inside the vessel during the discharge and the velocity field of the free jet when the gas flows out of the vessel. The research questions formulated at the beginning of chapter 1 are answered below:

1. What is a self-similar approach to describe a subcritical vessel outflow?
   A model was derived to characterise arbitrary subcritical outflows from round openings of ideal gases from arbitrary adiabatic vessels. The Bernoulli equation was used as the starting point for this model.
2. How can the outflow duration be determined by simple means?
   A distinction is made between two cases. For the first case of a thin-wall vessel, where frictional pressure losses $\Delta p_{\mathrm{friction}} \approx 0$ inside the outlet are negligible, an inertial loss model (ILM) and a dimensionless number Π_1 were derived. The ILM and the dimensionless number Π_1 showed constant values for a variation of the molar mass M, heat capacity ratio κ, temperature T_0, vessel volume V and opening diameter d_2. The ILM was validated based on numerical simulations. The mean deviation between the numerical simulations and the ILM is 1.94 %. The second case of a thick-wall vessel can be calculated with the model considering frictional and inertial pressure losses (FILM). The FILM was validated based on experimental investigations. The mean deviation between the FILM and the experiments is -1.75 %.
3. What influence does the Reynolds number have on the propagation of transient, subcritical free jets?
   A significant influence of the Reynolds number Re on the decay constant $K_{1,u}$ (p-value < $2.36 \cdot 10^{-4}$) and spreading rate $K_{2,u}$ (p-value < $7.52 \cdot 10^{-4}$) is determined based on a statistical analysis of the experimental data. The influence of the Reynolds number on the decay constant $K_{1,u}$ and spreading rate $K_{2,u}$ is so weak that it is not relevant for the most technical applications.
4. What influence does the density ratio have on the propagation of subcritical free jets?
   No significant influence (p-value > 0.31) of the density ratio R_ϱ on the decay constant $K_{1,u}$ and spreading rate $K_{2,u}$ could be observed. This supports the assumption of Chen and Rodi (1980) as well as Thring and Newby (1953) for stationary free jets. Therefore, the definition of a universal decay constant $K_{1,u} = 5.90$ and spreading rate $K_{2,u} = 0.10$ appears to be suitable.
5. Can a self-similar propagation also be observed for transient free jets?
   A transient free jet shows quasi-self-similar behaviour because the influence of the Reynolds number is small. If scaled with the time-dependent outlet velocity $u_0(t)$, then the entire velocity field can be described as a function of only one geometric variable.

6. Are the experimental results of the free jets replicable with numerical simulations?
   The stationary numerical simulations of the free jets have also shown a significant influence of the Reynolds number on the decay constant $K_{1,u}$ (p-value < $9.32 \cdot 10^{-9}$) and spreading rate $K_{2,u}$ (p-value < $6.82 \cdot 10^{-14}$). Therefore, the influence of the Reynolds number on the propagation that was previously observed in the experimental investigations is not due to buoyancy effects.
7. Is the new generalised k-ω turbulence (GEKO) model superior to the standard k-ε turbulence model for the simulation of round free jets?
   The GEKO model showed more accurate values for the decay constant $K_{1,u}$ and the spreading rate $K_{2,u}$ compared to the standard k-ε model during the simulations of air and carbon dioxide jets. For the simulations of helium free jets, the GEKO model had disadvantages compared to the k-ε model in determining the spreading rate $K_{2,u}$. A separation parameter of $C_{\mathrm{SEP}} = 2.2$ and a mixing parameter of $C_{\mathrm{MIX}} = 0.3$ were used for the GEKO model.

The results of this work are of relevance for a wide range of research fields. In particular, the findings can be used to derive a model for the propagation of hydrogen jets in the future. To date, there is a wide range of data on the dispersion behaviour of natural gas, but hardly any data on hydrogen. However, given that hydrogen is expected to be one of the main energy sources of the future, it appears necessary to conduct further research in this field. For this purpose, experimental investigations on the propagation of the hydrogen concentration could be carried out. The long-term target would be a universal model for determining the explosion protection zones of hydrogen in a wide variety of release scenarios and weather conditions.

Another interesting field in which the findings obtained here could be used is cryogenic energy storage. In this process, nitrogen is liquified and the energy is released through the expansion of the nitrogen during the phase change from liquid to gas. Currently, work is already being done on modelling these processes based on the ILM developed here. Moreover, it is desirable to extend the present investigations to outflows above the critical pressure ratio.

The GEKO model gave more accurate results than the k-ε model for the simulation of air and carbon-dioxide free jets, but this was not the case for the helium free jet. Future studies should try to find a correlation between the gas properties and the GEKO turbulence model parameters.
The hyperbolic approach of Chen and Rodi (1980) for the axial velocity profile of a free jet is only valid in the self-similar region. Currently, new functional approaches are being investigated to describe the axial velocity profile over all free jet regions.

In addition to the pure gas jets considered here, there is another field of free jets. Free jets can also be loaded with solid or liquid particles, leading to a multiphase problem. Due to the versatile technical

applications of particle-laden free jets, they offer an interesting field of research, which still has open questions due to complexity. These include (for example) the influence of particle size, particle density, particle loading and the interaction with the gas properties. Therefore, the transient propagation of particle-laden free jets should be investigated using the methods presented here. A first idealised model for predicting the discharge behavior of particles from a gas vessel has already been derived (Fischer et al., 2023).

Bibliography

Abraham, J. Entrapment characteristics of transient jets. *Numer. Heat Transf. A* **1996,** *30* (4), 347–364. DOI: 10.1080/10407789608913844.

Abramovich, G. N. *The theory of turbulent jets;* MIT-Press: Cambridge, MA, 1963.

Aihara, Y. Effects of an air stream on turbulent diffusion of a helium jet from a small nozzle. *Phys. Fluids* **1974,** *17* (4), 665–673. DOI: 10.1063/1.1694773.

Albrecht, H.-E.; Borys, M.; Damaschke, N.; Tropea, C. *Laser Doppler and Phase Doppler measurement techniques;* Springer: Berlin, Heidelberg, 2003.

Amielh, M.; Djeridane, T.; Anselmet, F.; Fulachier, L. Velocity near-field of variable density turbulent jets. *Int. J. Heat Mass Transfer* **1996,** *39* (10), 2149–2164. DOI: 10.1016/0017-9310(95)00294-4.

ANSYS. *ANSYS CFX 19.1-Solver Theory Guide*: Canonsburg, PA, 2019.

Ball, C. G.; Fellouah, H.; Pollard, A. The flow field in turbulent round free jets. *Prog. Aerosp. Sci.* **2012,** *50*, 1–26. DOI: 10.1016/j.paerosci.2011.10.002.

Batchelor, G. K. *An introduction to fluid dynamics*, 14th ed.; Cambridge University Press: Cambridge, U.K., 2010.

Birch, A. D.; Brown, D. R.; Dodson, M. G.; Thomas, J. R. The turbulent concentration field of a methane jet. *J. Fluid Mech.* **1978,** *88* (3), 431–449. DOI: 10.1017/S0022112078002190.

Bogey, C.; Bailly, C. Large eddy simulations of transitional round jets: Influence of the Reynolds number on flow development and energy dissipation. *Phys. Fluids* **2006,** *18* (6), 65101. DOI: 10.1063/1.2204060.

Bonelli, F.; Viggiano, A.; Magi, V. High-speed turbulent gas jets: an LES investigation of Mach and Reynolds number effects on the velocity decay and spreading rate. *Appl. Sci. Res.* **2021,** *107* (3), 519–550. DOI: 10.1007/s10494-021-00242-5.

Borée, J.; Atassi, N.; Charnay, G. Phase averaged velocity field in an axisymmetric jet subject to a sudden velocity decrease. *Exp. Fluids* **1996,** *21* (6), 447–456. DOI: 10.1007/BF00189047.

Boussinesq, J. *Essai sur la théorie des eaux courantes*; Mémoires présentés par divers savants à l'Académie des Sciences XXIII; Impr. nationale: Paris, 1877.

Buckingham, E. On physically similar systems; Illustrations of the use of dimensional equations. *Phys. Rev.* **1914,** *4* (4), 345–376. DOI: 10.1103/PhysRev.4.345.

Capp, S. P. Experimental investigation of the turbulent axisymmetric jet. Ph.D. Dissertation; University at Buffalo, SUNY, 1983.

Chang, J. I.; Lin, C.-C. A study of storage tank accidents. *J. Loss Prev. Process Ind.* **2006,** *19* (1), 51–59. DOI: 10.1016/j.jlp.2005.05.015.

Chen, C. J.; Rodi, W. *Vertical turbulent buoyant jets*. *A review of experimental data*, 4th ed.; HMT - Science and applications of heat and mass transfer; Pergamon Press: Oxford, U.K., 1980.

Chernyavsky, B.; Benard, P.; Oshkai, P.; Djilali, N. Numerical investigation of subsonic hydrogen jet release. *Int. J. Hydrogen Energy* **2014,** *39* (11), 6242–6251. DOI: 10.1016/j.ijhydene.2013.03.174.

Chernyavsky, B.; Wu, T. C.; Péneau, F.; Bénard, P.; Oshkai, P.; Djilali, N. Numerical and experimental investigation of buoyant gas release: Application to hydrogen jets. *Int. J. Hydrogen Energy* **2011,** *36* (3), 2645–2655. DOI: 10.1016/j.ijhydene.2010.04.130.

Colebrook, C. F.; White, C. M. Experiments with fluid friction in roughened pipes. *Proc. R. Soc. Lond. A* **1937,** *161* (906), 367–381. DOI: 10.1098/rspa.1937.0150.

Courant, R.; Friedrichs, K.; Lewy, H. Über die partiellen Differenzengleichungen der mathematischen Physik. *Math. Ann.* **1928,** *100* (1), 32–74. DOI: 10.1007/BF01448839.

Craske, J. Unsteady turbulent jets and plumes. Ph.D. Dissertation; Imperial College London, London, 2016.

Cumber, P. S. Predicting outflow from high pressure vessels. *Process Saf. Environ. Prot.* **2001,** *79* (1), 13–22. DOI: 10.1205/095758201531095.

Dantec Dynamics A/S. *LDA and PDA Reference Manuel*: Skovlunde, Denmark, 2011.

Ernst, R.; Groh, B.; Schmücker, A. *Potentially explosive atmosphere at exhaust opening of venting lines at gas plants or systems*. *Technischer Hinweis - Merkblatt Deutscher Verein des Gas- und Wasserfaches e.V. DVGW G 442 (M)*: Dorsten, Germany, 2015.

Fahrmeir, L.; Heumann, C.; Künstler, R.; Pigeot, I.; Tutz, G. *Statistik*. *Der Weg zur Datenanalyse*, 8th ed.; Springer Spektrum: Berlin, Heidelberg, Germany, 2016.

Ferdman, E.; Otugen, M. V.; Kim, S. Effect of initial velocity profile on the development of round jets. *J. Propul. Power* **2000,** *16* (4), 676–686. DOI: 10.2514/2.5627.

Ferziger, J. H.; Perić, M.; Street, R. L. *Computational methods for fluid dynamics*, 4th ed.; Springer: Cham, Switzerland, 2020.

Fick, A. Über Diffusion. *Ann. Phys.* **1855,** *170* (1), 59–86. DOI: 10.1002/andp.18551700105.

Fischer, H. B. *Mixing in inland and coastal waters;* Academic Press: New York, 1979.

Fischer, M.-D.; Baier, S.; Boettcher, K. E. Numerical modelling of the discharge behaviour of particles from a gas vessel. *Results Eng.* **2023,** *18*, 101207. DOI: 10.1016/j.rineng.2023.101207.

George, William K. *The self-preservation of turbulent flows and its relation to initial conditions and coherent structures;* Hemisphere: New York, 1989.

Gerold, J. Experimentelle und numerische Untersuchung von Gas-Freistrahlen. Ph.D. Dissertation; Universität der Bundeswehr München, Munich, Germany, 2015.

Grandchamp, X.; van Hirtum, A. Near field round jet flow downstream from an abrupt contraction nozzle with tube extension. *Appl. Sci. Res.* **2013,** *90* (1), 95–119. DOI: 10.1007/s10494-012-9429-5.

Hinze, J. O.; van der Hegge Zijnen, B. G. Transfer of heat and matter in the turbulent mixing zone of an axially symmetrical jet. *Appl. Sci. Res.* **1949,** *1* (1), 52. DOI: 10.1007/BF02120346.

Hrycak, P.; Jachna, S.; Lee, D. T. A study of characteristics of developing incompressible, axi-symmetric jets. *Lett. Heat Mass Transfer* **1974,** *1* (1), 63–71. DOI: 10.1016/0094-4548(74)90140-4.

Hussein, H. J.; Capp, S. P.; George, W. K. Velocity measurements in a high-Reynolds-number, momentum-conserving, axisymmetric, turbulent jet. *J. Fluid Mech.* **1994,** *258*, 31–75. DOI: 10.1017/S002211209400323X.

Idel'Chik, I. E. *Handbook of hydraulic resistance*, 4th ed.; Begell House: Redding, CT, 2008.

John, J. E.; Keith, T. G. *Gas dynamics*, 3rd ed.; Pearson Prentice Hall: Upper Saddle River, NJ, 2006.

Jones, W.; Launder, B. The prediction of laminarization with a two-equation model of turbulence. *Int. J. Heat Mass Transfer* **1972,** *15* (2), 301–314. DOI: 10.1016/0017-9310(72)90076-2.

Kast, W.; Nirschl, H. *VDI-Wärmeatlas*. Chapter L1.2 Druckverlust in durchströmten Rohren; VDI-Buch; Springer Vieweg: Berlin, Heidelberg, 2013.

Keagy, W. R.; Weller, A. E. A study of freely expanding inhomogeneous jets. *Proc. Heat Transfer, Fluid Mechanics Inst.* **1949,** *1*, 89–98.

Kümmel, W. *Technische Strömungsmechanik*, 3rd ed.; B.G. Teubner Verlag / GWV Fachverlage: Wiesbaden, Germany, 2007.

Kutta, W. Beitrag zur näherungsweisen Integration totaler Differentialgleichungen. *Zeitschrift für Mathematik und Physik* **1901,** No. 46, 435–453.

Kwon, S. J.; Seo, I. W. Reynolds number effects on the behavior of a non-buoyant round jet. *Exp. Fluids* **2005,** *38* (6), 801–812. DOI: 10.1007/s00348-005-0976-6.

Lau, J. C. Effects of exit Mach number and temperature on mean-flow and turbulence characteristics in round jets. *J. Fluid Mech.* **1981,** *105*, 193–218. DOI: 10.1017/S0022112081003170.

Launder, B. E.; Spalding, D. B. The numerical computation of turbulent flows. *Comput. Methods Appl. Mech. Eng.* **1974,** *3* (2), 269–289. DOI: 10.1016/0045-7825(74)90029-2.

Liepmann, H. W. Gaskinetics and gasdynamics of orifice flow. *J. Fluid Mech.* **1961,** *10* (1), 65–79. DOI: 10.1017/S002211206100007X.

Linstrom, Peter. *NIST Chemistry WebBook, NIST Standard Reference Database 69*, 1997. DOI: 10.18434/T4D303.

Loerbroks, C.; Mitropetros, K. *Auswirkungsbetrachtungen bei störungsbedingten Stoff- und Energiefreisetzungen in der Prozessindustrie: Methodenübersicht und industrielle Anwendung*, 3rd ed.; ProcessNet-Fachgemeinschaft „Anlagen- und Prozesssicherheit“: Frankfurt a. M., Germany, 2017.

Mani, M.; Babcock, D.; Winkler, C.; Spalart, P. Predictions of a supersonic turbulent flow in a square duct. In *51st AIAA Aerospace Sciences Meeting including the New Horizons Forum and Aerospace Exposition*; American Institute of Aeronautics and Astronautics: Reston, Virigina, 2013. DOI: 10.2514/6.2013-860.

Menter, F. R.; Lechner, R.; Matyushenko, A. *Best practice: Generalized k-omega two-equation turbulence model in ANSYS CFD (GEKO). Technical Report by ANSYS as an extension to the CFX theory guide*, 2019.

Mi, J.; Nathan, G. J.; Luxton, R. E. Centreline mixing characteristics of jets from nine differently shaped nozzles. *Exp. Fluids* **2000,** *28* (1), 93–94. DOI: 10.1007/s003480050012.

Mi, J.; Nobes, D.; Nathan, G. Influence of jet exit conditions on the passive scalar field of an axisymmetric free jet. *J. Fluid Mech.* **2001,** *432*, 91–125. DOI: 10.1017/S0022112000003384.

Milanovic, I. M.; Hammad, K. J. *PIV study of the near-field region of a turbulent round jet*. ASME 2010 3rd Joint US-European Fluids Engineering Summer Meeting collocated with 8th International Conference on Nanochannels, Microchannels, and Minichannels: Montreal, Quebec, Canada, 2010.

Najjar, Y. S. Hydrogen safety: The road toward green technology. *Int. J. Hydrogen Energy* **2013,** *38* (25), 10716–10728. DOI: 10.1016/j.ijhydene.2013.05.126.

Nitsche, W.; Brunn, A. *Strömungsmesstechnik*, 2nd ed.; VDI-Buch; Springer: Berlin, 2006.

Oertel, H. *Prandtl - Führer durch die Strömungslehre*, 13th ed.; Springer Vieweg: Wiesbaden, Germany, 2012.

Oertel, H.; Laurien, E. *Numerische Strömungsmechanik;* Springer: Berlin, 1995.

Olsson, M.; Fuchs, L. Large eddy simulation of the proximal region of a spatially developing circular jet. *Phys. Fluids* **1996,** *8* (8), 2125–2137. DOI: 10.1063/1.868987.

Panchapakesan, N. R.; Lumley, J. L. Turbulence measurements in axisymmetric jets of air and helium. Part 1. Air jet. *J. Fluid Mech.* **1993a,** *246*, 197–223. DOI: 10.1017/S0022112093000096.

Panchapakesan, N. R.; Lumley, J. L. Turbulence measurements in axisymmetric jets of air and helium. Part 2. Helium jet. *J. Fluid Mech.* **1993b,** *246*, 225–247. DOI: 10.1017/S0022112093000102.

Paschedag. *CFD in der Verfahrenstechnik;* Wiley VCH: Newark, NJ, 2006.

Pitts, W. M. Effects of global density ratio on the centerline mixing behavior of axisymmetric turbulent jets. *Exp. Fluids* **1991b,** *11-11* (2-3), 125–134. DOI: 10.1007/BF00190288.

Pitts, W. M. Reynolds number effects on the mixing behavior of axisymmetric turbulent jets. *Exp. Fluids* **1991a,** *11-11* (2-3), 135–141. DOI: 10.1007/BF00190289.

Pope, S. B. An explanation of the turbulent round-jet/plane-jet anomaly. *AIAA Journal* **1978,** *16* (3), 279–281. DOI: 10.2514/3.7521.

Pope, S. B. *Turbulent flows*, 12th ed.; Cambridge Univ. Press: Cambridge, U.K., 2015.

Rajaratnam, N. *Turbulent jets*; Developments in water science 5; Elsevier Scientific: Amsterdam, New York, 1976.

Renn, J.-C.; Hsiao, C.-H. Experimental and CFD study on the mass flow-rate characteristic of gas through orifice-type restrictor in aerostatic bearings. *Tribology International* **2004,** *37* (4), 309–315. DOI: 10.1016/j.triboint.2003.10.003.

Reynolds, A. J. Observations of a liquid-into-liquid jet. *J. Fluid Mech.* **1962,** *14* (04), 552. DOI: 10.1017/s0022112062001433.

Reynolds, O. On the dynamical theory of incompressible viscous fluids and the determination of the criterion. *Phil. Trans. R. Soc. Lond. A* **1895,** *186*, 123–164. DOI: 10.1098/rsta.1895.0004.

Richards, C. D.; Pitts, W. M. Global density effects on the self-preservation behaviour of turbulent free jets. *J. Fluid Mech.* **1993,** *254*, 417–435. DOI: 10.1017/S0022112093002204.

Richardson, L. F. The approximate arithmetical solution by finite differences of physical problems involving differential equations, with an application to the stresses in a masonry dam. *Phil. Trans. R. Soc. Lond. A* **1911,** *210* (459-470), 307–357. DOI: 10.1098/rsta.1911.0009.

Rist, D. *Dynamik realer Gase*. *Grundlagen, Berechnungen und Daten für Thermogasdynamik, Strömungsmechanik und Gastechnik;* Springer: Berlin, Heidelberg, 1996.

Romano, G. P. Large and small scales in a turbulent orifice round jet: Reynolds number effects and departures from isotropy. *Int. J. Heat Fluid Flow* **2020,** *83*, 108571. DOI: 10.1016/j.ijheatfluidflow.2020.108571.

Rosen, M. A.; Koohi-Fayegh, S. The prospects for hydrogen as an energy carrier: an overview of hydrogen energy and hydrogen energy systems. *Energ. Ecol. Environ.* **2016,** *1* (1), 10–29. DOI: 10.1007/s40974-016-0005-z.

Runge, C. Über die numerische Aufloesung von Differentialgleichungen. *Math. Ann.* **1895,** *46* (2), 167–178. DOI: 10.1007/BF01446807.

Rushton, J. H. The axial velocity of a submerged axially symmetrical fluid jet. *AIChE Journal* **1980,** *26* (6), 1038–1041.

Sautet, J. C.; Stepowski, D. Dynamic behavior of variable-density, turbulent jets in their near development fields. *Phys. Fluids* **1995,** *7* (11), 2796–2806. DOI: 10.1063/1.868658.

Schlichting, H.; Gersten, K. *Grenzschicht-Theorie*, 10th ed.; Springer: Berlin, Heidelberg, 2006.

Schmidt, E. Ausströmen von Gasen aus Behältern hohen Innendruckes. *Chem. Ing. Tech.* **1965,** *37* (11), 1091–1094. DOI: 10.1002/cite.330371103.

Shah, M. S.; Joshi, J. B.; Kalsi, A. S.; Prasad, C.; Shukla, D. S. Analysis of flow through an orifice meter: CFD simulation. *Chem. Eng. Sci.* **2012,** *71*, 300–309. DOI: 10.1016/j.ces.2011.11.022.

Smirnov, P. E.; Menter, F. R. Sensitization of the SST turbulence model to rotation and curvature by applying the Spalart–Shur correction term. *J. Turbomach.* **2009,** *131* (4). DOI: 10.1115/1.3070573.

So, R. M. C.; Zhu, J. Y.; Ötügen, M. V.; Hwang, B. C. Some measurements in a binary gas jet. *Exp. Fluids* **1990,** *9* (5), 273–284. DOI: 10.1007/BF00233128.

Spalart, P. R.; Venkatakrishnan, V. On the role and challenges of CFD in the aerospace industry. *Aeronaut. J.* **2016,** *120* (1223), 209–232. DOI: 10.1017/aer.2015.10.

Spalding, D. B. *Combustion and mass transfer*, 1st ed.; Pergamon Press: Oxford, U.K., 1979.

Squire, H. B.; Trouncer, J. Round jets in a general stream. *Reports and Memoranda, Aeronautical Research Committee* **1944**.

Sreenivasan, K. R. The passive scalar spectrum and the Obukhov–Corrsin constant. *Phys. Fluids* **1996,** *8* (1), 189–196. DOI: 10.1063/1.868826.

Stieß, M. *Mechanische Verfahrenstechnik 2;* Springer: Berlin, Heidelberg, 1997.

Stokes, G. G. On the theories of the internal friction of fluids in motion, and of the equilibrium and motion of elastic solids. In *Mathematical and Physical Papers vol.1*; Stokes, G. G., Ed.; Cambridge University Press: Cambridge, U.K., 2009; pp 75–129. DOI: 10.1017/CBO9780511702242.005.

Thring, M. W.; Newby, M. P. Combustion length of enclosed turbulent jet flames. *Symposium on Combustion New York* **1953,** *4* (1), 789–796. DOI: 10.1016/S0082-0784(53)80103-7.

Tollmien, W. Berechnung turbulenter Ausbreitungsvorgänge. *Z. Angew. Math. Mech.* **1926,** *6* (6), 468–478. DOI: 10.1002/zamm.19260060604.

Truckenbrodt, E. *Fluidmechanik 1: Grundlagen und elementare Strömungsvorgänge dichtebeständiger Fluide*, 4th ed.; Springer: Berlin, Heidelberg, 2008.

Walzel, P.; Tropea, C. *Proceedings / Conference Atomization and Spray Processes*. *March 18th and 19th 2004, University Dortmund ; final presentation of the DFG research program*; Schriftenreihe mechanische Verfahrenstechnik 7; Shaker: Aachen, Germany, 2004.

Wang, Z.; Andreopoulos, Y. Density and compressibility effects in turbulent subsonic jets part 1: mean velocity field. *Exp. Fluids* **2010,** *48* (2), 327–343. DOI: 10.1007/s00348-009-0738-y.

Weisgraber, T. H.; Liepmann, D. Turbulent structure during transition to self-similarity in a round jet. *Exp. Fluids* **1998,** *24* (3), 210–224. DOI: 10.1007/s003480050168.

Wendt, J. F. *Computational Fluid Dynamics;* Springer: Berlin, Heidelberg, 2009.

Wilcox, D. Reassessment of the scale-determining equation for advanced turbulence models. *AIAA Journal* **1988,** *26* (11), 1299–1310. DOI: 10.2514/3.10041.

Wilcox, D. C. *Turbulence modeling for CFD*, 2nd ed.; DCW Industries: La Cãnada, Calif., 1998.

Witze, P. O. Centerline velocity decay of compressible free jets. *AIAA Journal* **1974,** *12* (4), 417–418. DOI: 10.2514/3.49262.

Wygnanski, I.; Fiedler, H. Some measurements in the self-preserving jet. *J. Fluid Mech.* **1969,** *38* (3), 577–612. DOI: 10.1017/S0022112069000358.

Yan, Y.; Thorpe, R. Flow regime transitions due to cavitation in the flow through an orifice. *Int. J. Multiphase Flow* **1990,** *16* (6), 1023–1045. DOI: 10.1016/0301-9322(90)90105-R.

Zierep. *Grundzüge der Strömungslehre;* Springer: Wiesbaden, Germany, 2018.

Appendix

Table A.1.: Overview of stationary simulations for the propagation of an air jet without buoyancy.

Air		$k-\varepsilon$			GEKO			Exp.		
t / s	p_0-p_∞	Re	$K_{1,u}$	$K_{2,u}$	Re	$K_{1,u}$	$K_{2,u}$	Re	$K_{1,u}$	$K_{2,u}$
	/ Pa	/ -	/ -	/ -	/ -	/ -	/ -	/ -	/ -	/ -
0.5	47411	382244	4.94	0.105	386651	6.00	0.092	396620	6.05	0.088
1	44185	369664	4.92	0.105	373994	5.99	0.092	380677	6.45	0.091
2	36771	342881	4.90	0.105	342895	5.96	0.092	354068	5.84	0.096
3	31453	314509	4.93	0.105	318421	5.94	0.092	323771	6.09	0.091
4	25549	284697	4.89	0.105	288370	5.92	0.092	296041	5.98	0.091
5	21355	261118	4.86	0.106	264614	5.90	0.092	271042	5.91	0.093
6	16709	231807	4.82	0.106	234953	5.87	0.092	239867	5.81	0.089
7	12716	202768	4.80	0.106	205588	5.83	0.092	213451	6.29	0.094
8	9955	179637	4.78	0.106	182215	5.77	0.092	185475	5.80	0.096
9	7025	150967	4.74	0.106	153229	5.76	0.093	157866	5.61	0.095
10	5083	128313	4.71	0.107	130313	5.74	0.093	130515	5.43	0.102
11	3185	101298	4.67	0.107	102941	5.74	0.093	102743	5.88	0.103
12	1979	79517	4.63	0.107	80856	5.74	0.093	77495	5.43	0.122
13	952	54693	4.57	0.107	55647	5.70	0.093	54428	5.72	0.116
14	356	32990	4.49	0.107	33567	5.62	0.094	33731	5.85	0.097
mean			**4.78**	**0.106**		**5.83**	**0.092**		**5.88**	**0.096**
σ			0.136	0.001		0.11	0.001		0.27	0.010

Table A.2.: Overview of stationary simulations for the propagation of a carbon dioxide jet without buoyancy.

CO_2		$k-\varepsilon$			GEKO			Exp.		
t / s	p_0-p_∞	Re	$K_{1,u}$	$K_{2,u}$	Re	$K_{1,u}$	$K_{2,u}$	Re	$K_{1,u}$	$K_{2,u}$
	/ Pa	/ -	/ -	/ -	/ -	/ -	/ -	/ -	/ -	/ -
0.5	48025	580574	5.01	0.106	587244	5.99	0.093	594595	6.18	0.090
1	45620	566793	4.98	0.106	573389	5.98	0.093	581669	6.10	0.083
2	39925	532495	4.94	0.107	538902	5.96	0.093	555888	5.51	0.085
3	35689	505213	4.92	0.106	511429	5.94	0.093	523291	5.96	0.091
4	30777	471187	4.90	0.107	477150	5.94	0.093	494459	6.31	0.105
5	27147	444016	4.88	0.107	449743	5.92	0.093	466145	6.37	0.109
6	22972	410087	4.86	0.107	415486	5.91	0.093	442859	5.87	0.093
7	19169	421412	4.84	0.107	381027	5.91	0.093	407739	5.74	0.098
8	16402	348685	4.82	0.107	353438	5.85	0.094	369039	6.41	0.092
9	13266	314457	4.81	0.107	318857	5.76	0.094	345177	6.14	0.098
10	11022	287120	4.79	0.107	279257	5.78	0.094	319770	6.56	0.102
11	8531	252985	4.76	0.107	256687	5.76	0.094	281569	5.26	0.093
12	6786	225758	4.75	0.107	229146	5.75	0.094	247259	5.93	0.097
13	4893	191653	4.72	0.107	194625	5.78	0.094	213459	4.74	0.091
14	3349	158313	4.70	0.108	160860	5.79	0.094	179231	5.63	0.120
15	2348	132269	4.67	0.108	134463	5.78	0.094	149737	4.73	0.114
16	1383	101029	4.64	0.108	102775	5.75	0.094	113156	5.26	0.109
mean			**4.82**	**0.107**		**5.86**	**0.093**		**5.80**	**0.098**
σ			0.101	0.0006		0.09	0.0004		0.54	0.010

Table A.3.: Overview of stationary simulations for the propagation of a helium jet without buoyancy.

Helium		$k-\varepsilon$			GEKO			Exp.		
t / s	p_0-p_∞	Re	$K_{1,u}$	$K_{2,u}$	Re	$K_{1,u}$	$K_{2,u}$	Re	$K_{1,u}$	$K_{2,u}$
	/ Pa	/ -	/ -	/ -	/ -	/ -	/ -	/ -	/ -	/ -
0.5	42772	133572	5.08	0.099	142948.4	6.16	0.084	116770	6.30	0.098
0.75	38828	127406	5.07	0.099	128917.4	6.26	0.084	111650	6.36	0.100
1	35195	121437	5.05	0.100	122895.2	6.13	0.084	106535	6.29	0.103
1.25	31812	115588	5.02	0.100	117002.8	6.12	0.084	101513	6.06	0.105
1.5	28664	109847	5.00	0.100	111219.9	6.10	0.084	96348	5.76	0.112
1.75	23043	98704	4.96	0.100	99947.7	6.02	0.084	91845	6.13	0.101
2	20456	93091	4.94	0.100	94274.73	5.98	0.085	85786	6.06	0.099
2.25	18084	87601	4.92	0.100	88749.93	6.01	0.085	80692	5.72	0.095
2.5	15836	82031	4.90	0.100	83128.72	5.93	0.085	75391	5.91	0.097
2.75	13755	76489	4.88	0.100	77531.67	5.96	0.085	70311	5.79	0.096
3	11829	70951	4.86	0.100	71932.78	5.93	0.085	64895	5.63	0.108
3.25	10066	65445	4.84	0.101	66345.3	5.92	0.085	58313	5.65	0.113
3.5	7006	54536	4.80	0.101	55518.6	5.88	0.085	52073	5.75	0.120
mean			**4.95**	**0.100**		**6.03**	**0.085**		**5.96**	**0.104**
σ			0.09	$4.36 \cdot 10^{-4}$		0.11	$3.61 \cdot 10^{-4}$		0.25	0.007

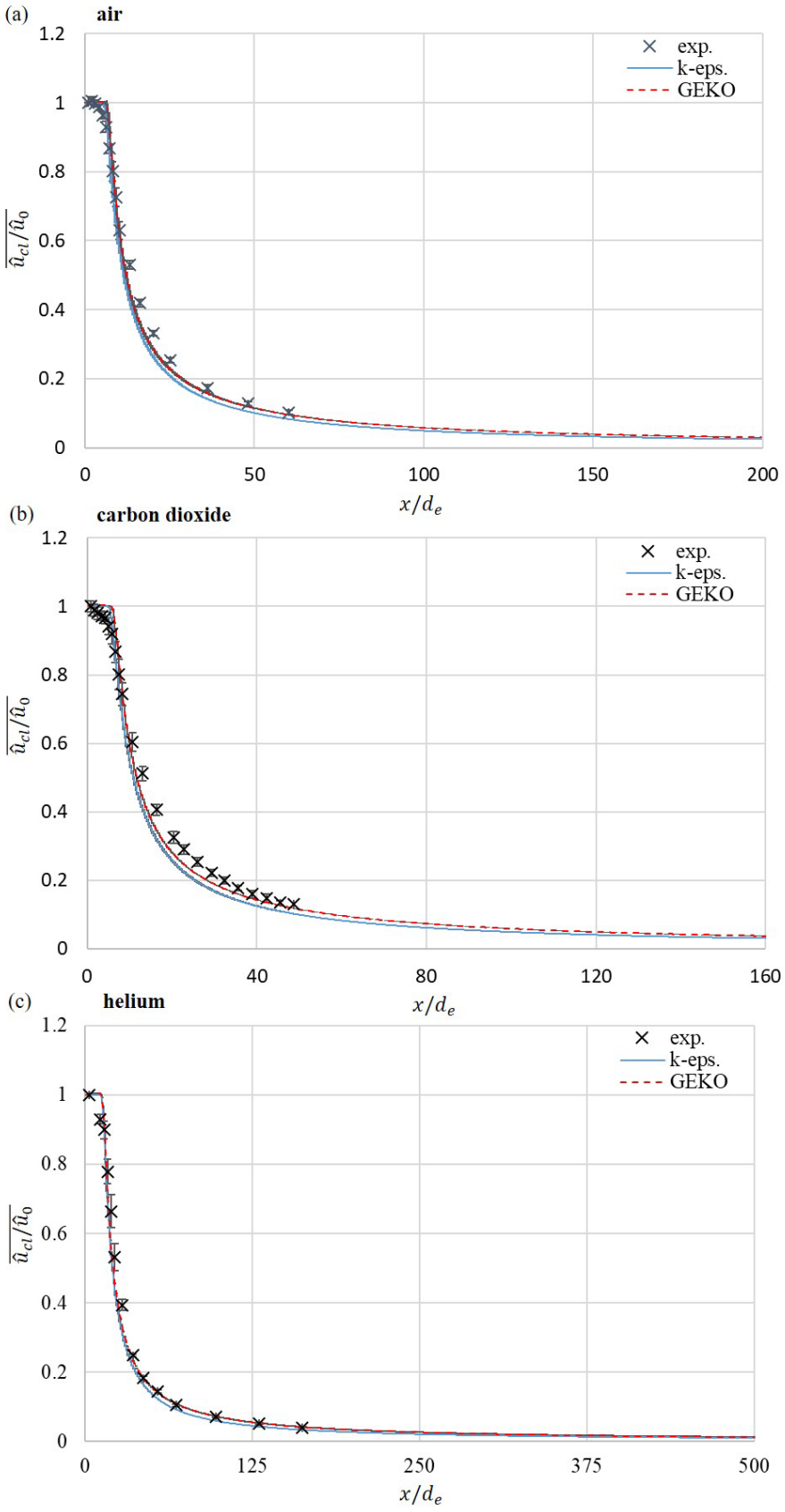

Figure A.1.: Results of the averaged axial velocity profile of the numerical simulations with the k-ε and GEKO model compared to the experimental (exp.) results. (a) air jet, (b) carbon dioxide jet and (c) helium jet. Error bars indicate the standard deviation.

Declarations

Declaration of pre-published content

Parts of this thesis were already published by the author in articles (PA1, PA2, PPA1). Some experimental data, simulations, and part of the methodology, are based on supervised master (M1-M2) and bachelor theses (B1-B3) at the Laboratory of Fluid Mechanics (Biochemical and Chemical Engineering, TU Dortmund University). This thesis contains the following reproductions:

chapter 1			
	1.1	content partly published in	PA1, PA2
chapter 2			
	2.1	content partly published in	PPA1
chapter 3			
	3.2	content published in	PPA1
	3.3	content partly published in	PA1, PA2
chapter 4			
	4.1	content published in	PA1, PA2
	4.2	content published in	PA1, PA2
	4.3	content published in	PA1, PA2
	4.4	content published in	PA1, PA2
	4.5	parts of the data are based on	M2
	4.6	content partly published in	PA1, PA2
chapter 5			
	5.1	content partly published in	PPA1
	5.2	content partly published in	PPA1
	5.3	content partly published in	PPA1
	5.4	content partly published in	PPA1
	5.5	content partly published in	PPA1
	5.6	content partly published in	PPA1
chapter 6			
	6.2	parts of the data are based on	B3

List of publications of Michael-David Fischer on this topic

Peer-reviewed articles

PA1 Fischer, M.-D.; Boettcher, K.
A fast method to predict the transient, subcritical gas discharge from a pressure vessel.
Chem. Eng. Sci. 2022, *249*.
DOI: 10.1016/j.ces.2021.117276

PA2 Fischer, M.-D.; Baier, S.; Boettcher, K.
Similarity solution of subcritical pressure discharges from vessels for arbitrary gases.
Chem. Eng. Sci. 2023, *267*.
DOI: 10.1016/j.ces.2022.118312

Preprint articles

PPA1 Fischer, M.-D.; Ryll, F.; Boettcher, K.
Measurement of the Reynolds number dependence of a transient air jet from a pressure vessel.
Preprint article published on *Research Square* 2022.
DOI: 10.21203/rs.3.rs-2311542/v1

Supervised Master's theses

M1 Kaufhold, N.
Modellierung explosionsgefährdeter Bereiche an Ausbläseröffnungen von Leitungen zur Atmosphäre an Wasserstoff-Gasanlagen
TU Dortmund University, Laboratory of Fluid Mechanics, November 2022

M2 Ryll, F.
Experimentelle Untersuchungen der Notentlastung eines Druckkessels
TU Dortmund University, Laboratory of Fluid Mechanics, April 2024

Supervised Bachelor's theses

B1 Knors, J.
Numerische Berechnungen zur Entwicklung eines Modells von unterkritischen, transienten Druckentlastungen
TU Dortmund University, Laboratory of Fluid Mechanics, September 2021

B2 Baier, S.
Numerische Modellierung des Austragverhaltens von Partikeln aus Gastanks
TU Dortmund University, Laboratory of Fluid Mechanics, May 2022

B3 Miyatake, L.
Numerische Untersuchungen zum Reynoldszahl und Turbulenzmodelleinfluss von Gas Freistrahlen
TU Dortmund University, Laboratory of Fluid Mechanics, August 2023